AN ABSTRACT OF THE THESIS OF

Krishnananda Shenoy for the degree of Master of Science in Mechanical Engineering presented on November 12, 1993.

Title: Residual Strength Properties of Gr/BMI Composite Laminates after Constant/Cyclic Compression

Redacted for Privacy

Abstract approved: _____

Ernest G. Wolff

An experimental method for compression loading of large numbers of composite specimens was developed. The electro-mechanical system, the loading procedure, and the associated mechanisms are described. Applicability of the system and residual strength property measurement procedures are discussed. Strength data obtained for $[0]_8$, $[90]_{16}$ and $[45/0/-45/90]_{16}$ IM7/5260-H Gr/BMI composite system layups are compared and discussed. Using experimental data from unidirectional layups as input to Genlam (a laminate program), tensile modulus and compressive strength for a $[45/0/-45/90]_{16}$ layup were predicted and compared. Strength curves based on a reduced Tsai-Wu strength criterion and experimental data were plotted and their significance with respect to safe states of stress were discussed. A 2D Finite Element Model simulating compression loading was created to show stress/strain gradients developed during specimen conditioning. This supports the loading procedure in terms of repeatability of tests and data for large number of specimens.

Additionally the microstructures of post exposure tested specimens were observed using established metallographic techniques. Possible failure modes relative to specimen orientation and conditioning history are discussed.

In summary, the research provided the basic groundwork for experimental conditioning, mechanical property measurement, theoretical predictions and probable failure modes for the Gr/BMI composite system.

Residual Strength Properties of Gr/BMI Composite Laminates after Constant/Cyclic Compression

by

Krishnananda Shenoy

A THESIS

Submitted to

Oregon State University

in partial fulfillment of

the requirements for the

degree of

Master of Science

Completed November 12, 1993

Commencement June 1994

APPROVED:

Redacted for Privacy

Associate Professor of Mechanical Engineering, in charge of major

Redacted for Privacy

Head of Department of Mechanical Engineering

Redacted for Privacy

Dean of Graduate School

Date thesis is presented November 12, 1993

Manuscript typed by the researcher Krishnananda Shenoy

DEDICATION

This work is dedicated to my parents whose love, understanding and trust has been the constant source of inspiration and strength to me.

Acknowledgments

First and foremost, I am grateful and indebted to my major professor, Dr. Ernest G. Wolff, for his constant encouragement, advice, confidence, patience, and support throughout my MS program. His research matched my career interests. I thank him very much for all this.

I would like to thank Dr. Timothy C. Kennedy, Dr. Jun Koike and Dr. Stephen W. Hoag for their time and consideration for serving on my graduate committee. My special thanks to Dr. Kennedy for his kind advice and support, both during my coursework and research. I thank Dr. Koike for his encouragement and advice.

I would like to specially extend my appreciation to the Boeing Commercial Airplane Group for financing the research project on High Speed Civil Transport at Oregon State. The project group was headed by Ramesh Khanna.

My special thanks to the Department of Mechanical Engineering for their kindness and administrative support during my entire graduate study.

Thanks especially to my fellow researcher and colleague Bill Hansen for his valuable advice and contribution during the developmental stage of the project. My special thanks to Sanji Widyaratne for his valuable time and help on the Instron and data-reduction of tested specimens.

Special thanks to my host family Tom and Patty McLintock for their friendship, hospitality and moral support during my stay here in Corvallis.

I would also like to thank all the professors under whom I studied, all the other staff members in the Department for their help, numerous friends and well wishers for their advice and support.

Table of Contents

List of figures

List of Tables

List of Appendices

List of appendices figures

Residual Strength Properties of Gr/BMI Composite Laminates after Constant/Cyclic Compression

1. Introduction

The trend towards composites usage in structural applications is continually on the rise. Composite materials allow significant weight savings, but cost effectiveness has been the key to the increased use of composites in commercial aircraft. All such future aircraft are likely to incorporate composites to a larger extent, especially to primary wing and fuselage structures. Currently composites comprise approximately 10% of a commercial aircraft's structural weight. For example, in a Boeing 767 this amounts to 3380 lbs, and the associated weight savings are about 1500 lbs. In keeping with these trends, many advanced composite systems that satisfy high temperature performance capabilities required for aerospace applications are currently being developed and researched. One such system developed by Boeing Commercial Aircraft with support from NASA under their Advanced Technology Composite Aircraft Structure (ATCAS) program was the Graphite/Bismaleimide (Gr/BMI) composite system. This system is one of the candidate composite materials being developed for use in their commercial supersonic aircraft, the High Speed Civil Transport (HSCT). The research here at Oregon State University (OSU) is part of the technology currently being developed for the HSCT airplane to support a possible roll out in the year 2005.

The Gr/BMI advanced composite system was specifically chosen by Boeing for use in HSCT application because of its promising tensile fatigue resistance, long term durability properties and thermal stability. In addition to having all the aforementioned advantages of composites, its relative ease of processing due to lower curing temperatures and better fracture toughness compared to epoxies has made the Gr/BMI system a viable choice. The need, therefore, to test the composite system, obtain strength data and establish its mechanical properties formed the basis for the research program at OSU. This, in turn, will provide the database for predictive modeling through testing of the material response to different controlling variables. Additionally it also would fulfill part of the overall objective of the program to determine the feasibility of Gr/BMI composite system for HSCT application.

The research involved the designing and developing of an experimental conditioning environment as per HSCT program specifications for compression loading of a large number of composite specimens subjected to different controlling variables. The variables were a) temperature, b) load, c) specimen layup, d) load/temperature spectrum and e) time period. The material response to control variables after the conditioning period was primarily obtained by determining all the relevant mechanical properties. This was done by testing the conditioned specimens on an Instron 4505 as per ASTM testing standards and reducing the test data for strength/stiffness properties [3]. A comparison of tensile strength and moduli for various exposures was done using experimental data. A comparison of tensile moduli and compressive strength data predicted using Genlam and from experiment for a $[45/0/-45/90]_{16}$ layup was done. Strength curves based on experimental data and reduced Tsai Wu failure theory

[5] were plotted. A simplified Finite Element model (FEA) to simulate experimental conditioning of individual layups was developed using COSMOS/M software. By means of the model, stress distribution plots for compression loading case were obtained. This would lend support to the experimental method discussed later. Results from the experiment and Genlam program are compared and discussed. Additionally, the microstructure of the tested specimens was studied using established metallographic techniques. This shed light on possible failure modes depending on orientation and specimen conditioning history for the Gr/BMI composite system.

Thus, the results provide the base for establishing the material response in prediction models for long term behavior of the material. Related work [2] on prediction of creep strains of non-linear viscoelastic composites with simultaneous aging and internal damage and Residual Strength [1] were recently reported.

This report focuses on a description of the experimental work and tensile test results for three different layups. Discussion of tensile moduli and compressive strength property data based on theory and experiment. It discusses the development of a finite element model and its implications on experimental loading of specimens. Finally, techniques used and inferences from microstructural observations of tested Gr/BMI specimens relative to failure modes are reported.

2. Theory

2.1 General Approach

Strength theories developed for isotropic materials have proved to be inadequate for composite materials. To describe the capabilities of anisotropic materials, it was necessary to modify many isotropic strength theories and to develop new onces [9]. The strength of unidirectional and multidirectional composites is usually described by quadratic interaction failure criteria in stress or strain space. The well-known Tsai-Wu strength theory [6] was chosen for this purpose. The Tsai-Wu theory is an extension of the von Mises or distortion energy theory as noted by Chou and McNamee [10]. Its characteristics are: (1) A criterion that is a scalar equation and is automatically invariant; (2) allows for transformation via known tensor transformation laws that lets failure plots to be rotated on the σ_x - σ_y plane and to be valid in all coordinate systems; and (3) the incorporation of symmetry properties like stiffness and compliances which makes the criterion mathematically rational and operationally simple [5]. It accounts for the strength difference in tension and compression and acknowledges possible interaction between normal and shear stresses. Other theories, namely the Maximum Stress theory and the Maximum Strain theory have three criteria each to be satisfied. In addition they do not account for interaction between normal stresses. The Tsai-Hill theory, on the other hand, does consider interaction, but failure cannot be related directly to the amount of distortional energy. This means an orthotropic material under a biaxial stress field cannot distort without extending. This limits the theory, in its description of experimental data, because of the reduced number of terms in the

prediction equation [7]. The Tsai-Wu, in constrast accounts for these inadequacies and other advantages stated above make it an attractive option.

2.1.1 Tsai-Wu Strength or the Quadratic Failure Criterion

In the Tsai-Wu strength criterion [5], it is assumed that there exists a closed failure surface in stress space. Its basic form is a scalar quantity,

$$F_{ij}\sigma_i\sigma_j + F_i\sigma_i = 1 \tag{1}$$

In strain components this is expressed as:

$$G_{ij}\varepsilon_i\varepsilon_j + G_i\varepsilon_i = 1 \tag{2}$$

where the F's and G's are combinations of strength parameters. Failure occurs when either equation is met. Equation 1 can be expanded for the case of a specially orthotropic ply under plane stress relative to the symmetry axes x-y or $i,j = 1,2,6$ as:

$$\begin{aligned} &F_{11}\sigma_1^2 + 2F_{12}\sigma_1\sigma_2 + F_{22}\sigma_2 2 + F_{66}\sigma_6 2 \\ &\quad + 2F_{16}\sigma_1\sigma_6 + 2F_{26}\sigma_2\sigma_6 \\ &\quad + F_1\sigma_1 + F_2\sigma_2 + F_6\sigma_6 = 1 \end{aligned} \tag{3}$$

where 1 coincides with the longitudinal direction of the composite,
2 coincides with the transverse direction of the composite,
6 is the shear component in the 1-2 plane.

For a unidirectional composite in its orthotropic axes, as shown in Figure 1, the strength should be unaffected by the direction or sign of the shear stress component. Reversing shear does not affect strength. However, sign reversal for the normal stress components, from tensile to compressive, is expected to have a significant effect on composite strength. Thus, all terms in equation 3 that contain linear or first degree shear stress are to be omitted. Further taking $i, j = x, y, s$ the terms F_{xs}, F_{ys} and F_s vanish.

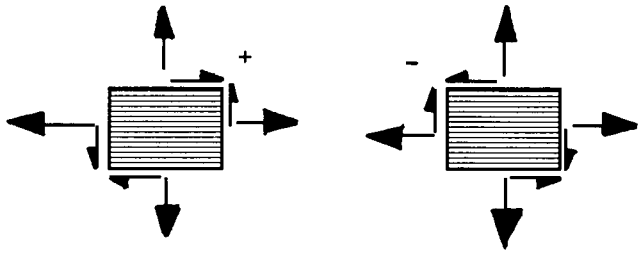

Figure 1. On-axis positive and negative shears.

The resulting equation after the removal of shear terms becomes,

$$F_{xx}\sigma_x^2 + 2F_{xy}\sigma_x\sigma_y + F_{yy}\sigma_y 2 + F_{ss}\sigma_s 2 + F_x\sigma_x + F_y\sigma_y = 1 \quad (4)$$

The failure criteria can also be expressed in terms of strain space by transforming the stress components into strain components [5].

$$F_{ij}\, Q_{ik}\, Q_{jf}\, \varepsilon_k\, \varepsilon_f + F_i\, Q_{ij}\, \varepsilon_j = 1 \quad (5)$$

defining G_{kf} and G_j as:

$$Gkf = F_{ij}\, Q_{ik}\, Q_{jf}$$
$$Gj = F_i\, Q_{ij} \quad (6)$$

upon substitution into equation 5, the failure criteria reduces to:

$$G_{kj}\varepsilon_k \varepsilon_f + G_k\varepsilon_k = 1 \tag{7}$$

expanding the equation, applied to a specially orthotropic case it becomes:

$$\begin{aligned} &G_{xx}\varepsilon_x^2 + 2G_{xy}\varepsilon_x\varepsilon_y + G_{yy}\varepsilon_y 2 \\ &\quad + G_{ss}\varepsilon_s 2 + G_x\varepsilon_x + G_y\varepsilon_y = 1 \end{aligned} \tag{8}$$

where,

$$\begin{aligned} G_{xx} &= F_{xx}Q_{xx}^2 + 2F_{xy}Q_{xx}Q_{xy} + F_{yy}Q_{xy}^2 \\ G_{yy} &= F_{xx}Q_{xy}^2 + 2F_{xy}Q_{xy}Q_{yy} + F_{yy}Q_{xy}^2 \\ G_{xy} &= F_{xx}Q_{xx}Q_{xy} + F_{xy}[\,Q_xQ_{yy} + Q_{xy}^2\,] + F_{yy}Q_{xy}Q_{yy} \\ G_{ss} &= F_{ss}Q_{ss}^2 + [\,Q_{ss}/S\,]^2 \\ G_x &= F_xQ_{xx} + F_yQ_{xy} \\ G_y &= F_xQ_{xy} + F_yQ_{yy} \end{aligned} \tag{9}$$

with the Q terms defined as follows:

$$\begin{aligned} Q_{xx} &= E_{xx}/(1-\nu_{xy}\nu_{yx}) \\ Q_{xy} &= \nu_{yx}E_{xx}/(1-\nu_{xy}\nu_{yx}) \\ Q_{yx} &= \nu_{xy}E_{yy}/(1-\nu_{xy}\nu_{yx}) \\ Q_{ss} &= E_s \end{aligned} \tag{10}$$

The only difficulty of the Tsai-Wu criterion, as noted by Raghava [10], is the determination of the interaction parameter F_{xy}. Determination of this parameter and its effects on failure surface is discussed in [9]. Suitable values for strength parameters are given in reference [5].

2.1.2 Strength Parameters

The Tsai-Wu theory, as noted from equation 4, consists of four quadratic strength parameters related to the four independent moduli components and two linear strength parameters. Of these six material constants, five can be measured by performing uniaxial tests. The longitudinal tensile strength X and compressive strength X' are then used to determine F_{XX} and F_X. Substituting these in equation 4 and setting $\sigma_y = \sigma_s = 0$;

when $\sigma_x = X$,

$$F_{XX}X^2 + F_X X = 1 \tag{11}$$

when $\sigma_x = -X'$,

$$F_{XX}X'^2 - F_X X' = 1 \tag{12}$$

solving the above equations for the two unknowns yields:

$$F_{XX} = 1 / XX' \tag{13}$$

$$F_X = 1/X - 1/X' \tag{14}$$

From transverse tensile strength Y and compressive strength Y', F_{yy} and F_y can be found through similar solutions.

$$F_{yy} = 1 / YY' \tag{15}$$

$$F_y = 1/Y - 1/Y' \tag{16}$$

Using the longitudinal shear strength S, F_{SS} and F_S are determined by substitution into equation 4.

$$F_{SS} = 1 / S^2 \tag{17}$$

Five of the six coefficients of the failure criterion as per equation 4 have been determined. The remaining term pertains to the interaction between two normal stress components and is called the interaction parameter. The exact value is difficult to measure as biaxial tests are to be performed [5]; however limits are imposed on this value from geometric considerations. The criterion dictating the type of curve is determined by the value of the discriminant in the equation.

$$\textbf{Discriminant} = F_{xx}F_{yy} - F_{xy}2 \quad \begin{cases} > 0 \text{ for ellipse} \\ = 0 \text{ for parallel lines} \\ < 0 \text{ for hyperbola} \end{cases} \tag{18}$$

To ensure a closed failure surface in the plane of the normal stress components, the value of the discriminant is constrained to the value of the ellipse and is closed to avoid infinite strength. This reduces the equation 18 to:

$$F_{xx}F_{yy} - F_{xy}2 > 0 \tag{19}$$

Defining the normalized interaction term as:

$$F^*_{xy}{}^2 = F_{xy}{}^2 / F_{xx}F_{yy} \tag{20}$$

The range of values expressed by the values of the normalized term:

$$-1 < F^*_{xy} < 1 \text{ for ellipse} \tag{21}$$

Rearranging equation 4 in terms of dimensionless parameters gives the quadratic form of the Tsai-Wu strength criterion as:

$$x^2 + 2F^*_{xy}\,xy + y^2 + z^2 + F^*xx + F^*yy = 1 \tag{22}$$

where,

$$\begin{aligned} x &= (F_{xx}\,\sigma_x)^{1/2} \\ y &= (F_{yy}\sigma_y)^{1/2} \\ z &= (F_{ss}\,\sigma_s)^{1/2} \end{aligned} \tag{23}$$

$$F^*_x = F_x / (F_{xx})^{1/2} = X' - X/(XX')^{1/2} \tag{24}$$

$$F^*_y = F_y / (F_{yy})^{1/2} = Y' - Y/(YY')^{1/2} \tag{25}$$

The stability limits for the normalized interaction parameter are:

$$-1 < F^*_{xy} < 1 \tag{26}$$

F^*_{xy} will govern both the slenderness ratio and the inclination of the major axis of the ellipse, i.e, +45 degrees for negative F^*_{xy}, and -45 degrees for positive F^*_{xy}.

Figure 2. Strength curve in stress space.

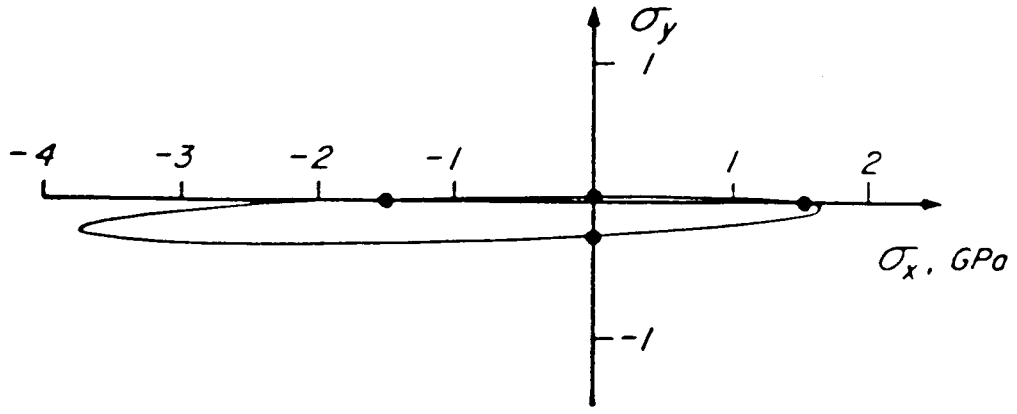

Generally strength curves are drawn with an assumed interaction term of the generalized von Mises criterion equal to -1/2. Figure 2 shows the assumed strength curve in stress space for material T300/5208 with F^*_{xy} = -1/2. In stress-space, as in Figure 2 above, the allowable strength curve for each material is anchored by four points representing the four measured strengths. These points are the intercepts of the stress axes shown as solid dots or focal points. All failure envelopes must pass through these intercepts. From the curve, note that there is a high degree of directionality in strength seen by the elongation along σ_x. It is seen that uniaxial stress induces biaxial strain because of the Poisson's effect. Similar intercepts in strain-space can be calculated using the on axis stress-strain relations. Figure 3 shows the plot for allowable strength curves in strain-space for various values of F^*xy. Comparatively less directionality is seen. Strength data for other unidirectional composites, their elastic constants and strength parameters for stress/strain are listed in reference 5.

Figure 3. Strength curve in strain space for different F^*xy.

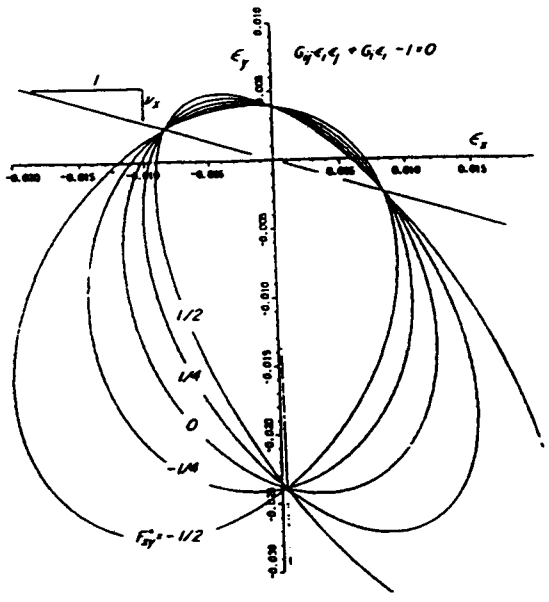

2.2 General Purpose Laminate Program - Genlam

The Genlam software [4] uses equation 4 and the laminate theory to predict laminate properties based on history dependence of ply parameters and hence the strength tensors F_{ij} and F_i. This through-the-thickness point stress laminate program gives stiffness constants, the compliance matrix and strength ratios. The model predicts the first ply failure stress and then assumes that the failed ply contributes only a fraction (the degradation factor DF) of its properties to the laminate until ultimate failure. It uses the quadratic failure criterion to compute strength ratios (R = ratio of strength to applied stress) of both intact and degraded matrix laminates [3]. Measured experimental properties from $[0]_8$ and $[90]_{16}$ layups were input into Genlam and the predicted values for a $[45/0/-45/90]_{16}$ laminate for different L - test exposures were obtained. These are tabulated and discussed in the results section of this report.

3. Component Material Properties and Fabrication Processes of the Gr/BMI System

3.1 Composite Materials-Definition and Background

Composites materials can be defined as materials composed of at least two distinctly dissimilar materials acting in concert. The properties of the composite system are not attainable by the individual components acting alone. A composite system is composed of a reinforcing fibrous material and a resin matrix binder. The combination yields a unique class of materials which provides a designer with tailorability that allows the properties, whether they be performance or processing, to be application specific. Depending on the specific components of a particular system, distinctions are made between the class of composites known as reinforced plastics and advanced composites. The Gr/BMI system belongs to the latter, which is the class of composites made of high modulus fibers such as Graphite and Boron, combined with a high performance matrix resin such as epoxy, vinyl ester etc. Why composites? Simply because such combinations of materials provide the composite system with unique properties that can be tailored to meet a broad spectrum of desired characteristics superior to traditional materials such as steel, aluminium etc. When compared to traditional materials, composites have higher moduli per unit weight and higher strengths per unit weight. These higher specific moduli and strengths can be translated directly into weight savings which, in turn, result in more efficient structures, reduced energy costs, and reduced material costs. Other advantages over traditional materials include resistance to fatigue and corrosion, low fabrication costs, tailored thermal expansion characteristics and

thermal conductivity, damping and design flexibility. These advantages is the reason for the widespread use of composites, especially in the aerospace and automotive industries [12].

3.1.1 Fibers and Resins

Today's designers and users of advanced composite materials have a wide variety of high performance reinforcing fibers and matrix resins available to them. There are literally limitless possibilities for users of this technology. Matrix resins are available that can satisfy a variety of requirement characteristics, such as sustained high temperature performance, improved fracture toughness, easy processing and improved environmental durability. Reinforcement fibers are available which also offer a variety of unique property characteristics. In the following sections, the key property characteristics of the components of the Gr/BMI advanced composite system will be discussed.

Graphite Fibers

Graphite fibers are high-strength, high-modulus, light-weight fibers which are the predominant reinforcement in advanced composites today. This high specific stiffness characteristic prompted an increased usage of advanced composites plus provided the expansion of a technology base that resulted in advances in areas of design and processing of new materials. Compared to boron, which has similar high specific properties, graphite offers significant cost and handling advantages. Consequently, it is attractive for use in high performance primary structure aircraft applications. Graphite fibers are prepared

from either organic fiber precursors or rayon precursors. However, in recent times polyacrylonitrile (PAN) is the predominant organic precursor fiber [13].

Many different processes have been used to convert PAN fibers into graphite fibers. The general process consists of the following four major steps:

1. Preparation: A process in which special grades of PAN fiber are produced. These fibers are subjected to a stretching operation which orients the fibrillar structure of the PAN and improves its mechanical properties.

2. Stabilization: A process in which the PAN is typically stabilized against polymer relaxation or softening during subsequent elevated temperature processing steps. The oriented PAN is typically stabilized under tension in an oxidizing atmosphere, resulting in reactions between the polymer and oxygen.

3. Carbonization: A process by which the stabilized PAN is pyrolyzed into carbon fibers. This process is carried out in an inert atmposphere at 1000-1500^{o} C. Tension is employed to achieve higher degrees of orientation.

4. Graphitization: A high temperature step, on the order of 2500-3000^{o} C, in which a higher carbon yield and more graphitic microstructure are obtained than in step 3. Higher degrees of orientation typically provide higher moduli.

Depending on the specific conditions employed in each step, graphite fibers having a wide range of properties may be obtained. The high mechanical properties achieved with graphite fibers are attributable to the structure and orientation of the graphite crystals formed during processing. The graphite crystal consists of planar layers of carbon atoms stacked on top of each other. Within the layers, the carbon atoms are joined by strong covalent bonds. These planar layers are oriented in the direction of the fiber axis as a result of the fiber processing steps. Varying degrees of orientation result in variations of

fiber properties, paticularly fiber modulus. In a final process, graphite fibers are subjected to a surface treatment using oxidation techniques with nitric acid solutions as the oxidizing agent. This results in increased resin-to-fiber adhesion and, in turn improved composite properties. Organic coatings are frequently used to protect the fiber during operations such as weaving and to improve wetting of the fibers by specific resin systems. Tables 1. and 2. show the range of available properties for selected graphite fibers [12].

Table 1. Typical Physical Properties of Carbon/Graphite Fibers

Property	PAN	Pitch
Diameter, μm	10.2	10.0
Longitudinal coefficient of thermal expansion, 10^{-6} in/in/^{o} F	-0.2 to -0.4	-0.5 to -0.9
Thermal Conductivity, Btu ft/hr ft^{2} ^{o} F	4-40	58-300
Electrical Resistivity, ohm-cm X 10^{-4}	9-18	2.5-7.5

Table 2. Fiber Properties With Different Precursors

Fiber	Precursor	Tensile Strength (10^{3} psi)	Tensile Modulus (10^{6} psi)	Strain-to-Failure (%)	Density (lb/in^{3})
T-300	PAN	500	33.5	1.50	0.0640
T-700	PAN	660	36.0	1.80	0.0650
T-55	PAN	350	57.0	0.70	0.0650
IM6	PAN	703	44.6	1.66	0.0632
HMS4	PAN	426	52.2	0.86	0.0645
T-55S	PITCH	250	55.0	0.50	0.0720
P-75S	PITCH	300	75.0	0.40	0.0720
P-100	PITCH	325	105.0	0.31	0.0780

Reinforcement Forms

Graphite fibers are available in a variety of product forms, such as continuous, chopped, woven fabrics and mats. The continuous graphite fibers also come in as yarns and rovings and tows - bundles of numerous filaments, typical counts ranging from 1000 - 10000. All of the fiber forms can be combined with a variety of resin systems to yield product forms, the most common being a prepreg tape. These tapes are prepared by collimating tows to the desired width and then impregnating them with a resin to yield a preimpregnated tape - the basic building block of advanced composite systems.

Polyimides

Polyimides are aromatic-heterocyclic polymeric resins which cure via cross-linking reactions or linear, chain-extension reactions to produce high temperature resistant, composite matrix resins. Polyimides are capable of performance at temperatures of upto 370^{o} C. The characteristic of polyimides that provides their elevated temperature stability is the aromatic-heterocyclic structure of the polymer backbone [12].

Figure 4. Polymer backbone structure.

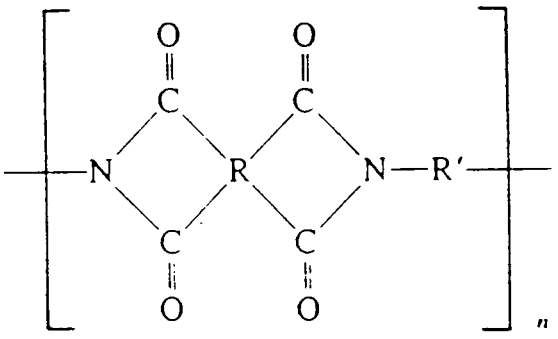

where R and R' can be varied.

This type of structure is thermally and thermo-oxidatively stable, and provides high glass transition temperatures. There are three classes of polyimide matrix resins for advanced composites: (1) Condensation Polyimides, (2) Polymerization of Monomeric Reactants (PMR) Polyimides, and (3) Bismaleimides (BMI's). Reaction are described in reference 12.

BMI Polyimides

The class called Bismaleimides was introduced by the French in the late 1960s and is a polyimide that cures via addition reactions without volatile evolution, which results in easier processing. In this class of polyimide resins, the baseline BMI is formed by the reaction of a diamine (either aromatic or aliphatic) with maleic anhydride:

Figure 5. Formation of BMI by reaction of a diamine with maleic anhydride.

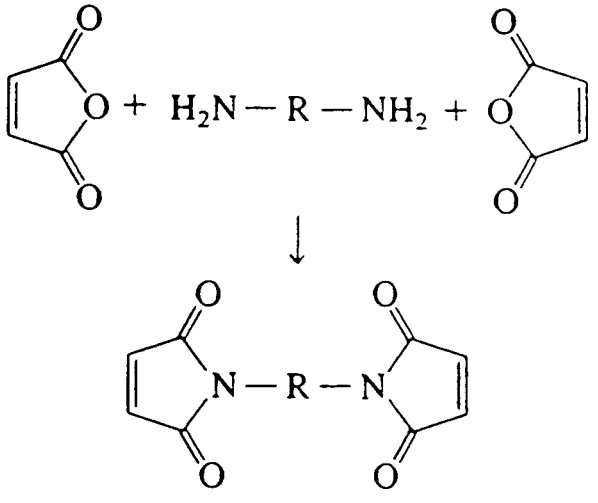

where R can be varied to achieve a variety of characteristics. This BMI can be used by itself, with other BMI's, and with diamines to form a final resin

system. Cure of the final resin can occur via two possible mechanisms depending on the resin composition. If diamines are used, there are two steps in the cure. The first step is a Michael addition reaction of the diamine across the double bond. The second step is the free radical polymerization of the double bonds [13].

Figure 6. Free radical polymerization.

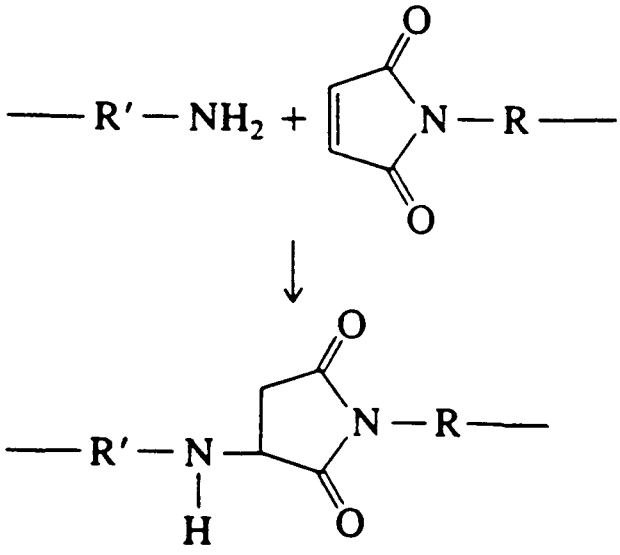

In the case of BMI's without diamines, cure proceeds via the free radical reaction only. The BMI monomers can be dissolved in solvents to form varnishes for fiber impregnation, or they can be formulated with reactive diluents similarly to the unsaturated polyesters to give solventless, hot-melt resin systems.

Processes

Starting materials for BMI composites can be prepreg product forms or they can be dry molding compounds. The nature of the prepreg products can vary greatly as a function of resin composition. All of the product forms are available with a variety of fiber reinforcements like graphite, glass, etc.

Cure is a function of the product form. Molding compounds and dry, boardy prepregs are typically cured with high pressure and temperatures of 450-550^{o} F in press cures or injection molding operations. Wet, solvent-based prepregs or hot-melt, solventless prepregs are procurable by vacumn-bag or autoclave cured at temperatures of 350^{o} F and 100 psi pressure. Postcures at temperatures of 425-475^{o} F are typically employed.

Performance Characteristics

Properties attainable with BMI resin/graphite fiber composites are shown in Table 3. BMI's are not as thermally stable as condensation or PMR polyimides, but they are much more thermally stable than epoxies. The system shown in the table is a formulated product that possesses epoxy-like mechanical properties while demonstrating outstanding temperature and moisture resistance. This characteristic has made BMI composites a popular choice for high performance aircraft structures such as wings and fuselage.

Table 3. Mechanical and Physical Properties of a BMI/Graphite Composite (V378A/T300)

Property	Value
Flexural Strength, ksi	
RT	265.0
177° C	197.5
232° C	179.0
288°C	122.0
316°C	107.0
Flexural Modulus, Msi	
RT	19.8
177° C	20.7
232° C	19.2
288° C	18.4
316° C	17.6
Short Beam Shear, ksi	
RT	18.3
177° C	10.9
232° C	9.2
288° C	6.4
316° C	5.8
RT Tensile	
Strength, ksi	228.9
Modulus, Msi	21.8
Strain, %	1.05
Density, g/cc	1.60
Fiber content, vol %	65

3.2 Experimental Methodology and Testing Procedure

3.2.1 Background for Test Methodology, Development and Testing

The aerospace engineering community has evolved practical procedures for demonstrating adequate service life for composite structures. Because of uncertainties in translating coupon data to components, service life is demonstrated at the component level. Current engineering certification approaches are governed by the lack of a definitive life prediction methodology. At the laminate-element level, however, tests are conducted using test coupons to establish life versus cyclic load levels to avoid fatigue degradation. Scatter in fatigue life data is addressed by increasing the spectrum load level so that, typically, testing for two life-times becomes statistically significant. Life is best defined by changes in such properties as strength or stiffness. Property changes can be interpreted by simulation models relating such changes to life, reliability and performance characteristics. Mechanistic models and data are needed that include proper representations of service effects such as multidimensional stress states, temperature, loading rate and sample size under service conditions. Experimental procedures to simulate such conditions is necessary for characterization of exposure effects on the materials. This characterization is carried out in real time in terms of engineering properties for design as well as in terms of basic material changes. The property data so obtained is to be validated against the long-term prediction models and real-time data base [14].

The foremost issue involving materials and structures, then, is the effects of exposing composite materials to load and temperature during operation and

the damage tolerance of the composite structure. The primary exposure effect appears to result from the combination of mechanical load, temperature and time history during supersonic flight. Currently the life of an airplane is defined as 72,000 total hours, 60,000 of which are supersonic and 30,000, flight cycles. These have been determined based on a 20-year life span [15].

3.2.2 Test Method

A static test method was developed, with the basic design specifications being provided by Boeing, to simulate the exposure effects through compression loading of a large number of test specimens. Compression loading of Gr/BMI coupons in terms of fixture development and assembly, test procedures and the strength/stiffness characterization based on property determination is discussed.

3.2.3 Strength/Stiffness Characterization of Gr/BMI system

All relevant strength and mechanical properties for the graphite/bismaleimide (IM7/5260-H) were experimentally determined. The evaluation material used was in four laminate configurations - unidirectionals, 90's or transverse unidirectionals, quasi-isotropic and [+/-45] layups - to provide specific mechanical properties. The Gr/BMI composite system is currently under investigation at Oregon State University as part of the High Speed Civil Transport Program funded by the Boeing Commercial Aircraft Group. A test matrix was devised in conjunction with Boeing personnel to obtain the required input parameters. The devised matrix will produces data which are both statistically valid and needed to develop prediction models. Table 5 shows the

test matrix, according to which tests will be performed on each of the layups and specimen types required to obtain the necessary properties. The test matrix was devised in order to subject a specimen of particular orientation to all relevant combinations of controlling variables to not only give the necessary properties but make them statistically valid. For example, referring to the Table 5 for test L3 the variables are a) time (3 months), b) temperature (75^{o} F), c) load (zero), both the temperature/load spectrum being constant and so on. Table 4. summarizes the tensile specimen configurations required for property characterization. For example, the $[0]_8$ and $[90]_{16}$ layups are used to obtain unidirectional strength and moduli. A quasi-isotropic laminate - $[+45/0/-45/90]_{16}$ was chosen to test predictions based on ply (0, 90 or +/-45) data [3]. Table 5 accordingly, shows the matrix, test variables and specimen layups for different tests. These test specimens, numbering 300, each of 8 or 16 plies, were fabricated by the Boeing Aircraft Company from the IM7/5260-H system and received at OSU in June of 1991. They were then stored at ambient temperature and humidity (50% RH). Mechanical property evaluation was based on the understanding of material behavior in a four-hour compression loading at variable temperature and stress levels, followed by one-hour relaxation at room temperature with zero stress level according as test matrix [2].

Table 4. Tensile Specimen Configurations and Test Methods

Property	Layup	Dimensions (l x w x t) inch	Test Method
E_1, X	$[0]_8$	10.0 x 1.0 x 0.046	ASTM D 3039
E_2, Y	$[90]_{16}$	10.0 x 1.0 x 0.093	"
E_1, X	$[45/0/-45/90]_{16}$	"	"

Table 5. Test Matrix Specifications

Test	Time	Temp.	Loaded	Spectrum	Layups	[0]	[0]	[90]	[90]	[±45]	[Quasi A]	[Quasi A]
Sample Type						Compressive	Tensile	Compressive	Tensile	Shear	Compressive	Tensile
Baseline						2	2	2	2	2	2	2
L1	0	75	no	const/const		2	2	2	2	2	1	2
L2	0	75	yes	const/const		2	2	2	2	2		2
L3	3	75	no	const/const		2	2	2	2	2		2
L4	3	75	yes	const/const		2	2	2	2	2	2	2
L5	3	75	yes	cyclic/cyclic		2	2	2	2	2	2	2
L6	0	300	no	const/const		2	2	2	2	2		2
L7	0	300	yes	const/const		2	2	2	2	2		2
											—	
L8	3	300	no	const/const		2	2	2	2	2	1	2
L9	3	300	no	cyclic/cyclic		2	2	2	2	2	1	2
L10	3	300	yes	const/const		2	2	2	2	2	2	2
L11	3	300	yes	cyclic/cyclic		2	2	2	2	2	2	2

3.2.4 Static and Cyclical Compression Testing for Exposure Effects

With the aforementioned requirements for strength characterization, a test matrix that uses two time periods (zero and three months), two temperatures (ambient and 300^{o} F), two compressive stress levels (zero and as per Table 5), with both static (S) and cyclic (C - 4h on, 1h off) stresses/temperatures, with appropriate specimen layups as per Table 5 was used for the purpose. For compressive load application on several specimens simultaneously, the test method chosen paid special attention to stress uniformity and specimen buckling. It also paid attention to friction between all moving surfaces and the amount of clamping necessary to hold the specimen. The method was based on the compression between links of a chain loaded in tension. A photograph of a typical setup for constant compressive loading along with the associated instrumentation, appears in Figure 7 below:

Figure 7. Photograph of typical setup for constant compression loading.

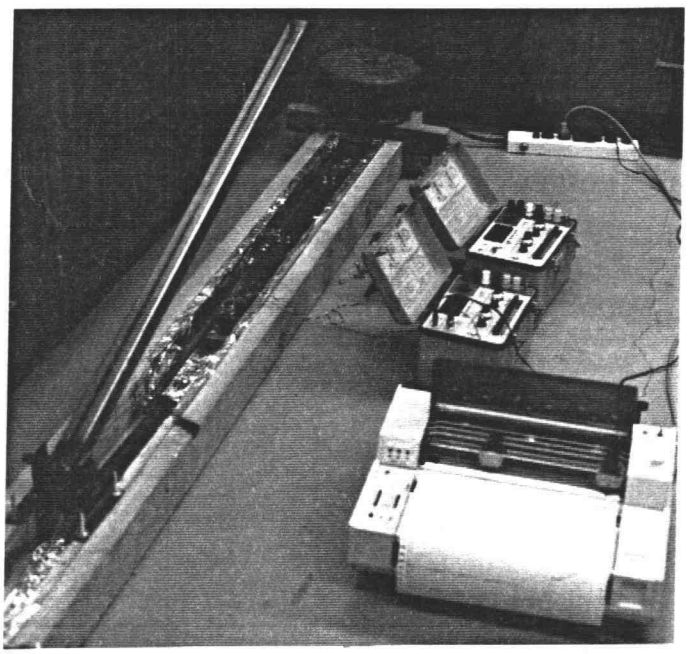

3.2.5 Description of fixtures and fixture assembly

The test specimens were both compressive and tensile, tabbed and untabbed in accordance with ASTM D3039, with dimensions as per Table 4. In order to apply constant and cyclic compressive loads with either constant or cyclic temperatures, a special fixture was developed. The test method required the fixture to be of multispecimen test capability in that it had to be able to compressively load several specimens simultaneously. This loading had to be constant over the length of the specimen (no stress gradients) as well as throughout the entire fixture assembly. Also, due to the method of loading, the fixture had to be capable of preventing any buckling of the specimen during load transfer. In addition the fixture had to have a minimal thermal mass to facilitate concurrent heating/cooling upon load application and removal [3]. A photograph of the resulting fixture, which evolved after several design modifications, is shown in Figure 8 below:

Figure 8. A typical fixture holding two specimens.

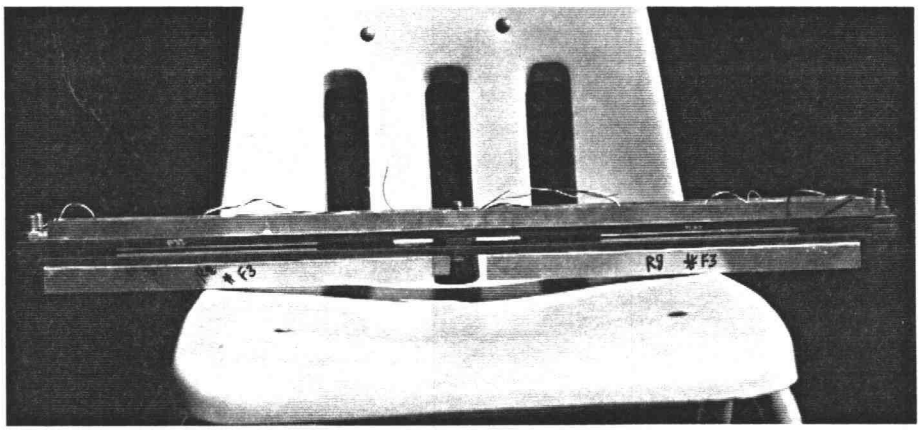

It consists of two steel strips, 24.6" x 1.5" x 0.00635 x 0.25" thick which are separated at each end and in the middle by three rectangular steel blocks which have a thickness just greater than the total thickness of the specimen and the tabs. These rectangular blocks are held in place by six 1/4" bolts which pass through the bottom steel strip. In the gap between the top and bottom strips, provided by the rectangular blocks, a specimen is placed against each end block. Parallel rows of 1/8" bolts, sixteen in number, are fastened between the top and bottom strip to prevent buckling along the length of each specimen. Two steel plates of thickness equal to that of the tabbed specimens act as sliders, and are placed in the gap between the center rectangular block and the other end of the specimen. These slider plates are wider than the steel strips and have two holes on each exposed end. Shims are used to fill the remaining gap between the top and bottom steel strips and the central untabbed section of the specimen. These shims provide necessary clamping to the specimens by preventing lateral movements. The shims are held in place by the bolts. Uniform tightening of the bolts, using a torque wrench and consistency in assembly, ensures this. Friction on all sliding surfaces is minimized by covering with a adhesive teflon tape. The fixture size varies according to specimen size. The photograph in Figure 9 shows three individual fixtures, each essentially similar except for the dimensions which are specimen dependent. Each fixture can hold two specimens. Several such fixtures are placed end to end with the forward slider of the trailing fixture attached by four steel strips to the rear slider of the leading fixture. This is shown in the schematic [3] of Figure 10.

Figure 9. Three dimensionally different fixtures as per specimen size.

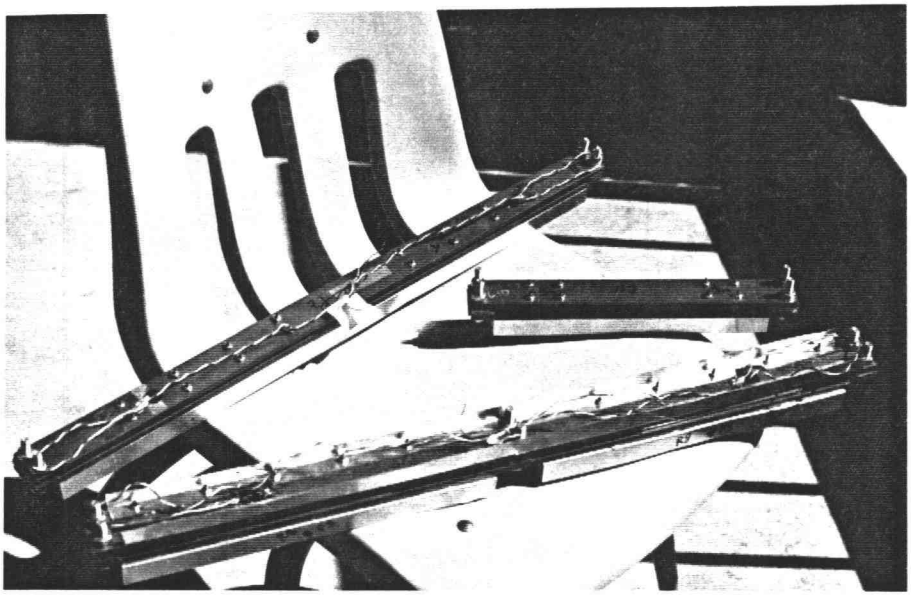

Figure 10. Schematic of a typical fixture setup.

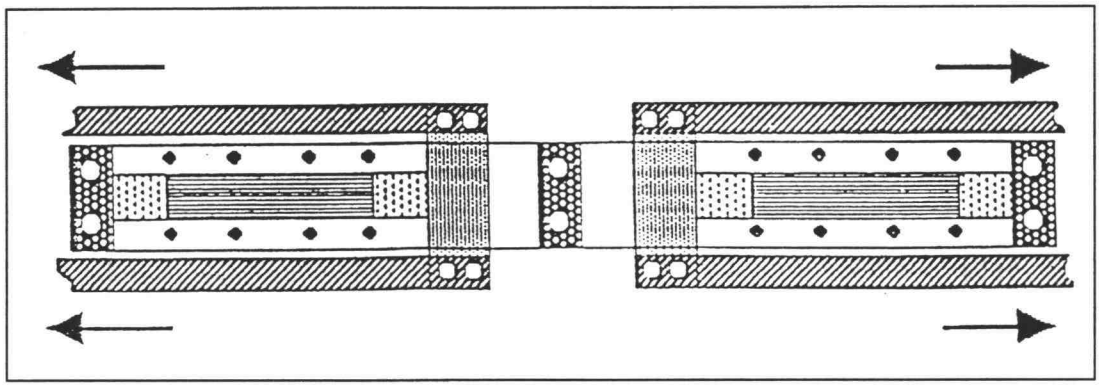

These fixtures are linked together, constituting a chain, with the specimens between the links. Additionally, two L-shaped aluminium fins are attached to the bottom steel strip of the fixture. This enables the placement of

the fixture on steel rollers and allows for the free rolling movement of the chain upon loading. The chain of fixtures is placed in a U-shaped wooden channel lined with aluminium foil (Figure 11 below):

Figure 11. Chain of fixtures assembled in the wooden channel.

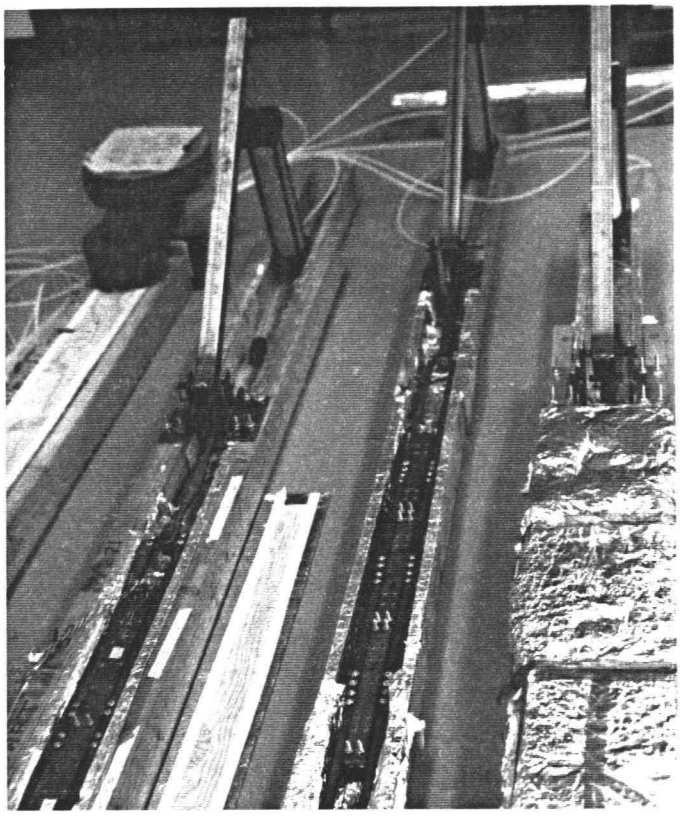

3.2.6 Load Application Procedure

To apply the load, the chain of fixtures is fixed at one end of the channel with wooden blocks. The other end is attached to a lever arm. Each steel plate at the free ends of the chain is centrally drilled. A long bolt passes through the steel plate, the wooden blocks holding the whole chain in tension.

This is shown in the photograph in Figure 12. At the other end, the chain is linked to the lever arm through a turn-buckle. The turn-buckle allows for the adjustment of the slack, after the whole chain is in the wooden channel. Two different lever arm types, each of 8:1 load ratio, are used, depending on the desired loading spectrum. The loading action is achieved when the whole chain of fixtures is placed under tension while the individual fixtures with the specimens are in compression. In the constant load configuration of Figure 7 an inverted L-shaped lever arm with the longer arm stretched over the fixture chain is used. A steel pin welded into the long arm end allows for the dead weight loads to be applied. Weights were calibrated to give appropriate load, using a load cell and a Vishay P3500 strain indicator box.

A schematic of the constant load configuration, along with the dead weights and load direction, is as shown in Figure 12. The action of the cyclic load configuration, is basically the same, but here air cylinders are used and is shown in the photograph in Figure 13. Here the lever arm extends ahead of the chain and has a 3/4" bolt hole drilled instead of the pin at the longer end. A special bolt threaded through its diameter passes through this hole. The bolt enables the threaded plunger rod to be screwed onto itself providing the attachment from the air cylinder to lever arm. The loading action is accomplished when timer controlled air cylinders, also fixed to the wooden channel push up against the lever arm pulling the chain in tension as seen in Figure 13.

Figure 12. Constant load application using dead weights and lever arm.

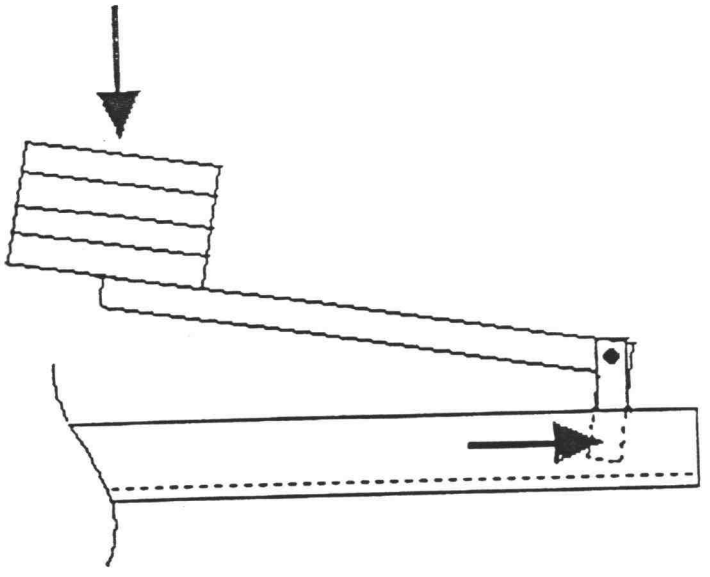

Figure 13. Cyclic load application using air cylinders.

3.2.7 Associated Mechanical and Electrical accessories

Air Cylinders

Speedaire Air Cylinders Model 6 x 393 inch, 2.5 bore and 10 inch stroke capable of applying upto 250 psi pressure were used. Maximum pull force applicable was 921 lbs. Air supply was provided through an air filter and regulator for efficient operation. These were bolted to the wooden channel and linked to the chain via the lever arm.

Air Regulators and Pressure gages.

This is shown in the photograph in Figure 14. Standard air regulators with associated phenolic piping and brass fittings were used for air supply to and from the cylinders. Standard commercial pressure gages were used to measure the supply pressure.

Figure 14. Air regulators and associated accessories.

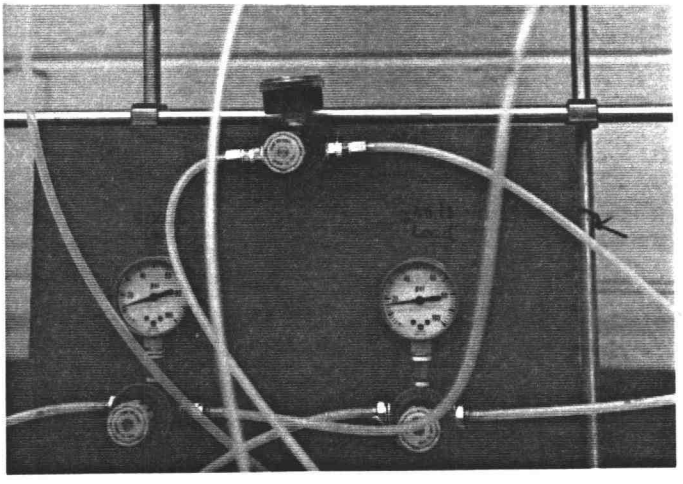

Solenoid Valves

These are shown in the photograph in Figure 15. These were standard DC-powered valves. They were used to control the direction of the flow of air to and out of the system, depending on the timer signal. Figure 16 shows the overall setup of air supply, air control and regulation.

Figure 15. Solenoid valves.

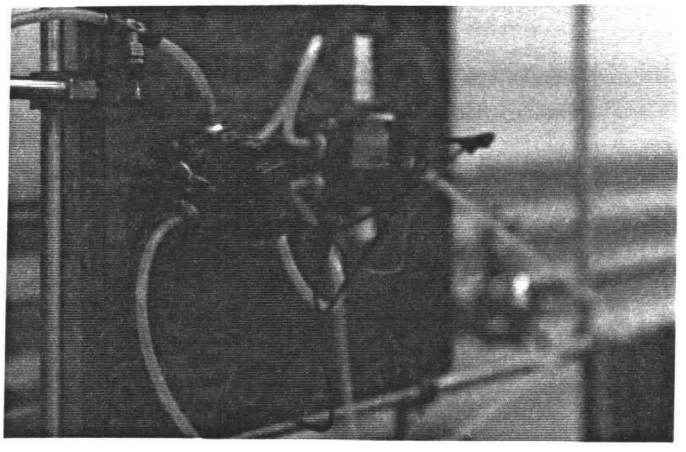

Figure 16. Air supply, regulation and control setup.

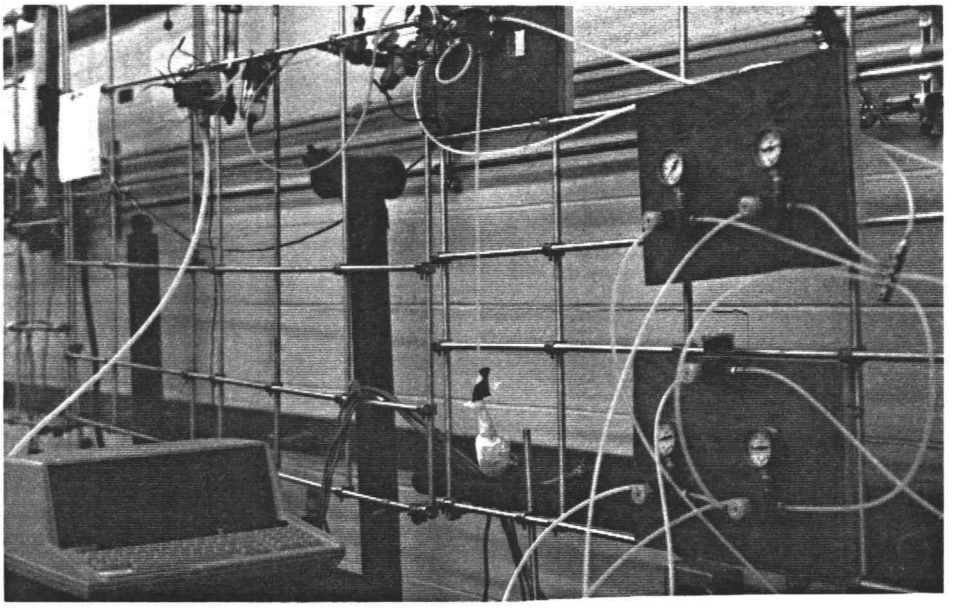

Time Controller

A standard electrical signal activated MC series recycling multicam timer model A-30 was used. It appears in the photograph in Figure 18 along with temperature controller panels. Cam adjustment provided for control of total time as a percentage of on/off time. This is done by initially setting the cam, and then powering the timer unit. In our case, each cycle ran for 4 hours on, 1 hour off.

Cycle Counters

These are spring controlled contrivances and are hooked to the lever arm through a string link attachment as shown in Figure 16. When the lever arm is stretched upon loading the spring is activated via the link to increment the counter reading.

Figure 17. Schematic of heater setup shown along with a cross-section of the channel.

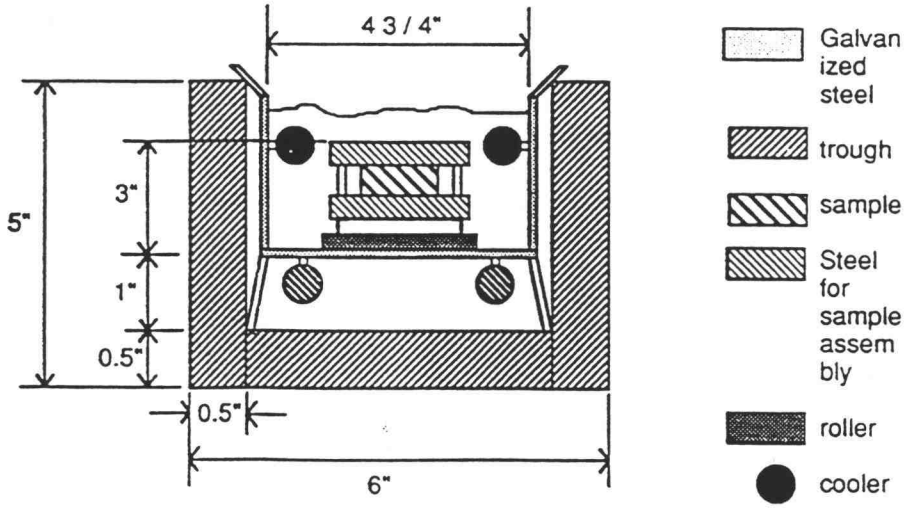

Diameter of roller 3 / 8"
Diameter of heater and cooler 3 / 4"
Galvanized steel 1 / 8"

Heaters and Control Circuit

These were Nichrome wire 28 gage resistive heaters contained in Pyrex glass tubes. Resistance equaling 60 ohms was placed in series below the specimens through a channel arrangement as seen in the sketch in Figure 17. The Pyrex tubes were sealed at either ends using Teflon fabric and silicone adhesive. The heaters were rated at either 120 V or 240 V, depending on constant/cyclic temperature requirements. Typical heating time from room temperature to 300^{o} F was 35 minutes.

Temperature Controllers

These were standard OMEGA CN350 miniature controllers for thermocouple input from resistive loads (heaters). They are time proportional with a manual reset having an accuracy of +/- 1.5 % + 1 digit for thermocouple input. The photograph in Figure 18 shows the temperature control panel and the associated circuitry. This includes fuses to prevent overloading of the circuit and power switches to allow the heaters to be turned off individually without interfering with other tests.

Figure 18. Temperature control panel with temperature controllers and electrical wiring.

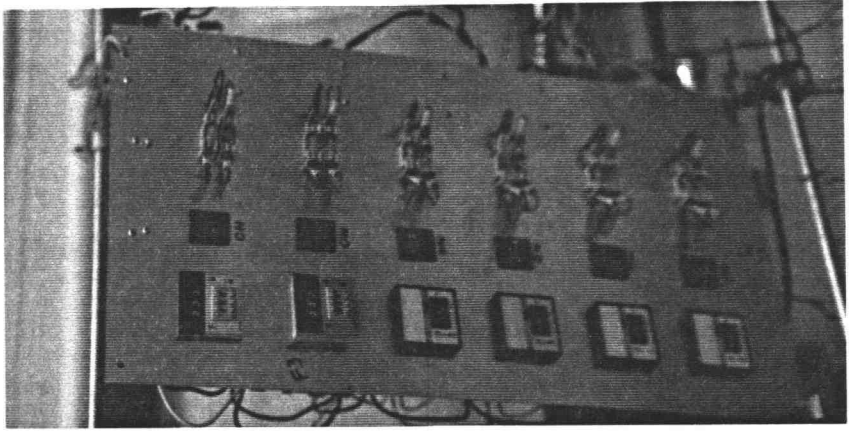

Relays

Standard OMRON Solid State 10A 300 V rated AC Relays were used together with the temperature controllers to control power to individual heater units.

Thermocouples and Digital Temperature Indicator

Standard Iron-Constantan "J" curve thermocouples with positive iron wire and a negative constantan were used as temperature sensors. A minimum of three were used in each test to average out local temperature differentials. Two were connected to the temperature controller and one to the digital indicator for temperature readout.

DC Power Supply

A Transistorized Power Supply Model 2015R rated for 24 V DC was used to power the solenoid valves.

Thermostats

These were connected in series with the heaters for safety against temperature surges. In case of local temperature gradients being greater than the rated temperature, power to the heating units would be automatically shut off.

Other accessories included general wiring, piping, insulation tape, teflon tape, high temperature resistant tape, wire connectors, 5A fuses, additional 2 x 4 inch wooden panels for channel reinforcement glass wool for heat insulation and a standard tool set.

3.3 Equipment and Associated Instrumentation for Property Measurement

All mechanical properties were obtained by tensile and compressive testing as per ASTM standards after the specimens were subjected to exposure effects according to the test matrix. This report sticks to tensile testing only. Tensile testing was done in accordance with ASTM D 3039. Standard Instron grips were used. The rigged up test setup is seen in the photograph in Figure 19. The testing was completed using an Instron 4500/4505 controlled by a Labview II program on a Macintosh SE, which recorded the applied load and crosshead displacement. A listing of the labview program appears in Appendix 1. The strains were sensed by Micro measurements type AE strain gauges and read by Vishay Model P3500 strain indicators which supplied a voltage signal. This signal was converted to analog readout and recorded on a chart by a Soltec 1243 chart recorder.

Figure 19. A typical testing setup on the Instron with associated instrumentation.

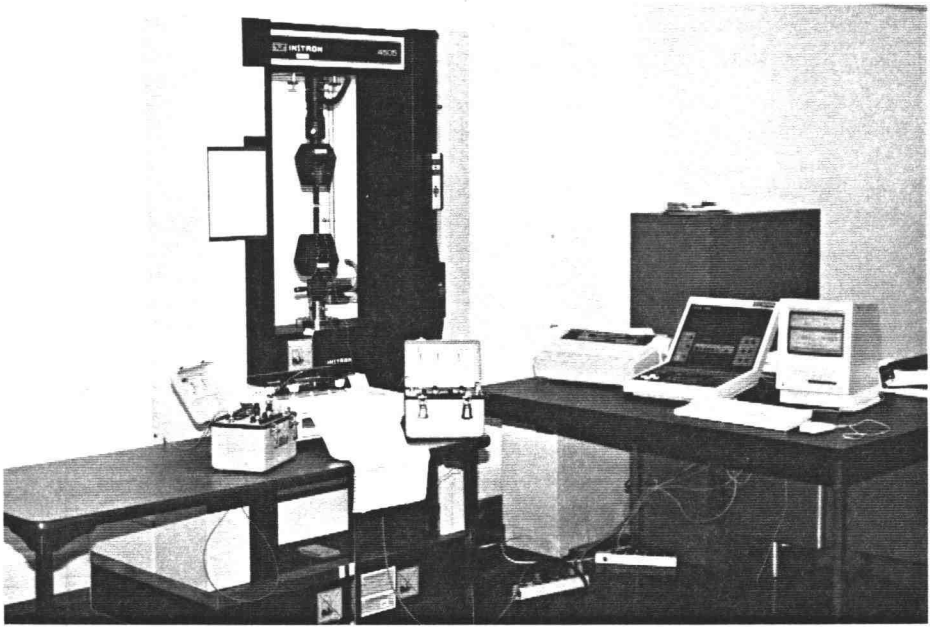

3.3.1 Uniaxial Characteristics - Measurement and Data Reduction Procedure

The uniaxial characteristics were determined using standard test methods and specimens listed in Table 4. Residual Stiffness (modulus) is recorded as a measure of strength degradation. The stiffness tests were conducted on tensile specimens and modulus was determined by recording strains to failure and calculated in accordance with ASTM D 3039. Appendix 2 gives curves of stress versus strain for the results listed in Tables 6 - 8 (pp. 41-43). A linear curve fit of the type shown below was applied for better accuracy.

$$\sigma \text{ (psi)} = a + b * \varepsilon \text{ (in/in)}$$

where 'ε' is the engineering strain, has been fitted to each curve.

For Residual Strength the procedure went as follows: first strain was recorded off the chart recorder as a percentage of the distance to failure. Next this was repeated for the load recorded from the Instron data acquisition system. Then both strain and load data were correlated to get the actual tensile stress/strain data [3]. Finally strength was calculated in accordance with ASTM D 695. Tables 6 - 8, appearing in the results section (pp. 41-43), list relevant tensile modulus and residual tensile strength data for the $[0]_8$, $[90]_{16}$, and $[45/0/-45/90]_{16}$ layups respectively.

4. Results and Discussion

4.1 Residual Tensile Strength and Modulus

Results from uniaxial testing of tensile specimens gave the following material properties, listed in Tables 6-8 after L1 - L11 (conditioning history as per Table 5) exposures. Residual Strength after each of the exposures showed a general trend of decreasing strength value compared to the unexposed specimens. This showed that there is some form of damage occurring during the conditioning of the specimens. Damage could be due to weak or misaligned fibers or flaws leading to microcracks, both of which induce increasing stress on other fibers and matrix, eventually leading to failure of the laminate. Strength depends on the amount of damage. This is expected and accounts for the lower strength data. This holds true for the $[0]_8$ and $[90]_{16}$ layups; however for some exposures, L4 and L8, the numbers were higher. This could be because of or a combination of experimental errors, such as specimen alignment, scaling and gage length effects. The other possibility is that during the conditioning, a break may have occurred due to mechanical problems, power outage or stoppage due to premature specimen failure. This would allow the specimen to recover, depending on the elastic limit and recovery time. On the other hand, if the loading level is sufficiently low where the strength property is insensitive to the conditioning, then obviously little or no damage will occur. This accounts for variability of the strength and moduli numbers.

A plot of variation of experimental tensile strength versus exposure appears in Figure 20 (p. 44) for a $[45/0/-45/90]_{16}$ layup. From the plot it is

seen that the general trend of decreasing strength as a measure of damage holds true. A plot of the modulus variation appears in Figure 21 for the same layup. The moduli numbers, though, are somewhat higher for similar reasons.

Table 6. Measured Uniaxial Tensile Properties For a $[0]_8$ Layup IM7/5260-H

Exposure #	Modulus msi (E_1)	Strength ksi (X)
L1	22.0	337.4
	22.34	336.6
average	22.17	337.0
L2	23.1	343.1
	23.2	335.8
average	23.15	339.5
L3	22.71	362.78
	23.65	356.32
average	23.18	359.55
L4	35.1	400.6
	24.3	352.1
average	29.7	376.4
L5	34.8	347.1
	31.4	369.2
average	33.1	358.15
L6	28.8	347.7
	35.3	340.9
average	32.1	344.3
L7	21.6	311.4
	(27.34)	(331.6)
average	24.47	321.5
L8	23.11	362.4
	(22.14)	(350.2)
average	22.63	356.3
L9	23.76	352.35
	21.43	317.09
average	22.59	334.72
L10	29.22	350.41
	(26.43)	(342.6)
average	27.83	346.51
L11	23.06	330.02
	(27.84)	(329.6)
average	25.45	329.81

Table 7. Measured Uniaxial Tensile Properties For a $[90]_{16}$ Layup IM7/5260-H

Exposure #	Modulus msi (E_2)	Strength ksi (Y)
L1	1.26	10.6
	1.18	9.9
average	1.22	10.3
L2	1.27	9.4
	1.23	8.7
average	1.25	9.1
L3	1.40	11.16
	1.27	6.51
average	1.34	8.84
L4	1.49	10.0
	1.43	10.6
average	1.46	10.3
L5	1.38	9.1
	1.42	7.5
average	1.40	8.3
L6	1.26	11.1
	1.26	8.4
average	1.26	9.8
L7	1.33	11.5
	1.21	10.2
average	1.27	10.9
L8	1.49	9.3
	(1.45)	(10.1)
average	1.47	9.4
L9	1.33	7.83
	1.26	7.67
average	1.3	7.75
L10	1.3	8.34
	1.38	7.39
average	1.34	7.87
L11	1.31	7.54
	(1.54)	(8.56)
average	1.43	8.05

Table 8. Measured Uniaxial Properties For a $[45/0/-45/90]_{16}$ Layup IM7/5260-H

Exposure #	Modulus, msi (E_1)	Strength, ksi (X)
L1	9.7	117.6
	11.18	149.6
average	10.44	133.6
L2	(8.27)	129.6
	11.2	(136.3)
average	9.75	132.95
L3	9.27	115.29
	8.8	116.97
average	9.04	116.13
L4	10.87	123.03
	9.01	140.67
average	9.94	131.85
L5	7.82	127.83
	8.1	117.93
average	7.96	122.88
L6	6.0	107.8
	8.4	126.6
average	7.2	117.2
L7	8.4	118.2
	(9.2)	(122.4)
average	8.8	120.3
L8	9.04	119.02
	8.7	127.83
average	8.87	123.43
L9	7.87	117.61
	8.83	117.83
average	8.35	117.72
L10	9.99	122.39
	13.82	125.0
average	11.91	123.69
L11	8.38	114.56
	8.98	108.24
average	8.68	111.4

( ) is the estimated value

Figure 20. Variation of tensile strength versus exposure for a $[45/0/45/90]_{16}$ layup.

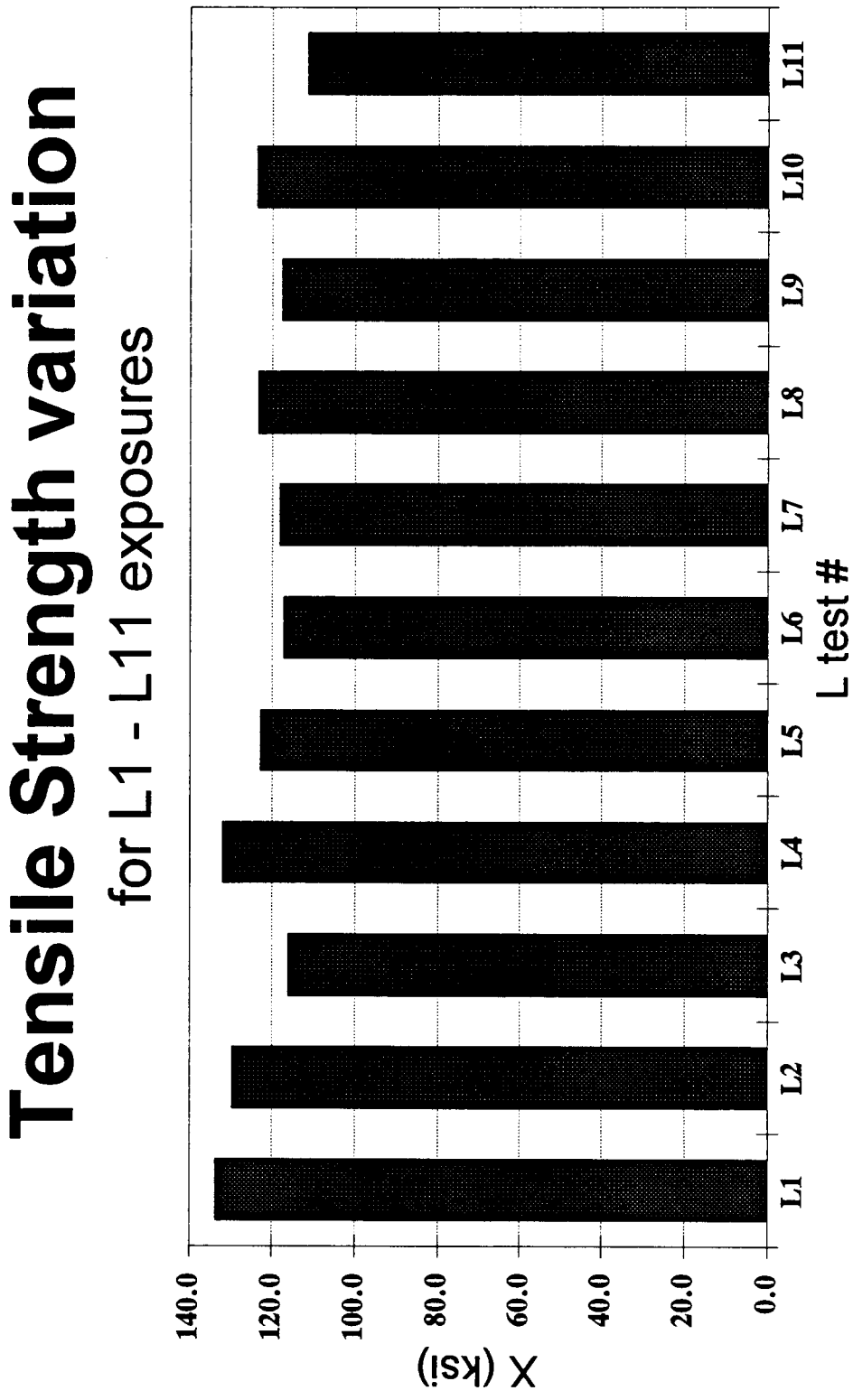

Figure 21. Variation of tensile modulus versus exposure for a $[45/0/-45/90]_{16}$ layup.

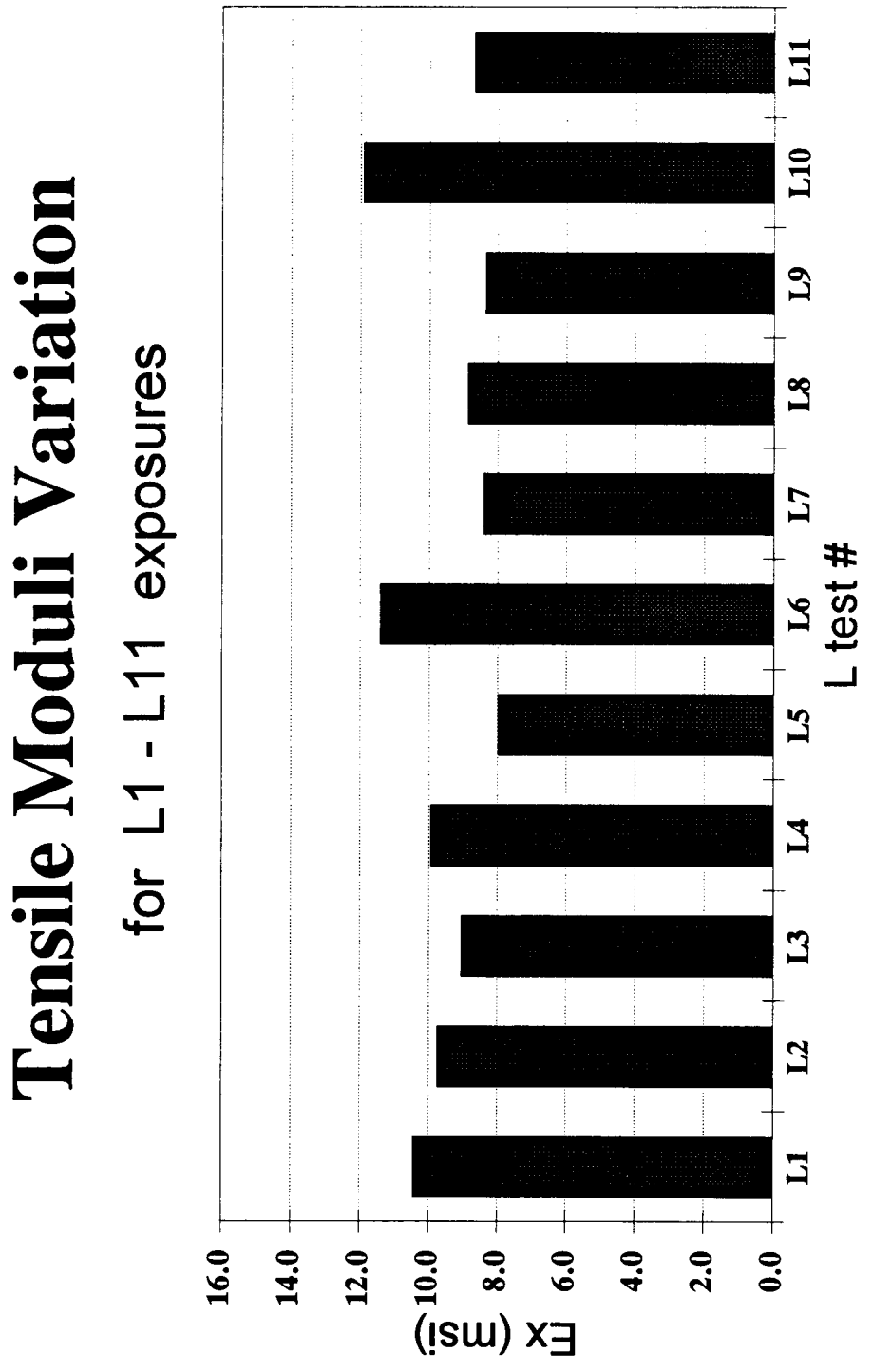

The Genlam program predicted strength numbers as per [3].

Table 9. Tensile Moduli From Experiment and Theory For a $[45/0/-45/90]_{16}$ Layup

Exposure #	Experimental E_1 (msi)	Theoretical E_1 (msi)
L1	10.44	8.55
L2	9.75	9.49
L3	9.04	8.92
L4	9.94	10.65
L5	7.96	12.51
L6	11.4	12.15
L7	8.4	8.04
L8	8.87	8.81
L9	8.35	8.3
L10	11.91	10.43
L11	8.68	10.39

From the plot of Figure 22 it is seen that there is good correlation for L3, L4, L6, L7, L8, and L9. For the others the experimental values are slightly higher. This is probably due to one or more factors discussed earlier. Moreover in the theoretical input values for the expansion coefficients were considered equal to those of graphite/epoxy. Further average of two values from experimental data for the $[0]_8$ and $[90]_{16}$ layup were used. For some cases an average value was unavailable, so an estimated value was used. Also the theoretical program does not take into account the local load and temperature variations, that may have existed over the specimen length during the exposure period. These could be the reasons for the variation in the predicted and experimental values. The remedy would be to have at least an average of four values with closer tolerances on the conditioning and testing wherever possible.

Figure 22. Plot of theoretical and experimental tensile moduli for a $[45/0/-45/90]_{16}$ layup.

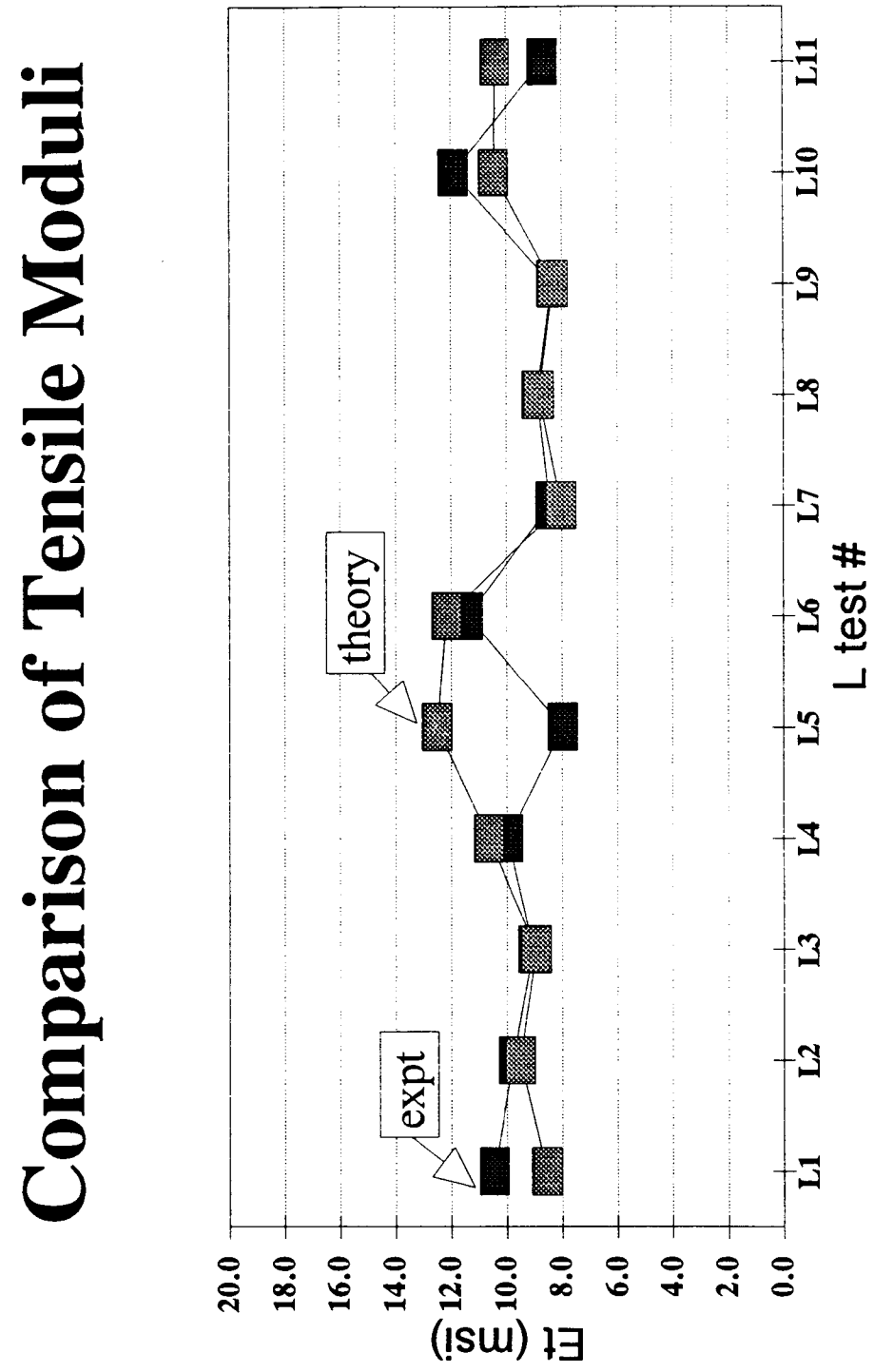

4.1.1 Compressive Strength

Experimental uniaxial strength properties were input into Genlam and the predicted output for a Quasi layup were obtained as outlined in section 2.2. A comparison plot of experimental compressive strength values [3] and theoretical values as applied to the individual exposures are listed in table 10. below:

Table 10. Experimental and Theoretical Compressive Strength Values For a $[45/0/-45/90]_{16}$ Layup

Exposure #	Experimenal X' (ksi)	Theoretical X' (ksi) DF = 0.1	DF = 0.2	DF = 0.3
L1	95.0	114.2	114.3	115.3
L2	121.8	117.73	120.44	121.25
L3	122.2	116.1	116.1	116.1
L4	113.8	127.21	128.57	130.45
L5	118.92	118.27	119.89	121.25
L6	115.81	117.2	117.14	117.2
L7	102.65	107.17	109.61	111.51
L8	118.59	123.43	123.4	123.43
L9	107.25	117.9	117.7	117.69
L10	124.61	120.44	123.14	125.14
L11	111.76	120.71	123.15	125.04

From the plot of Figure 23 it was observed that the experimental values came closest to the theoretical values for a degradation factor D.F of 0.3 (is a measure of % contribution of first ply failure to overall laminate failure). This could be because the factor 0.3 comes closest to the actual damage occurrng during conditioning. Except for L1 and L4 good correlation was found for all exposures. Comparable plots with DF = 0.1 and DF = 0.2 appear in Figures 24 and 25 respectively.

Figure 23. Plot of compressive strength comparison from theory and experiment with DF = 0.3 for a $[45/0/-45/90]_{16}$ layup.

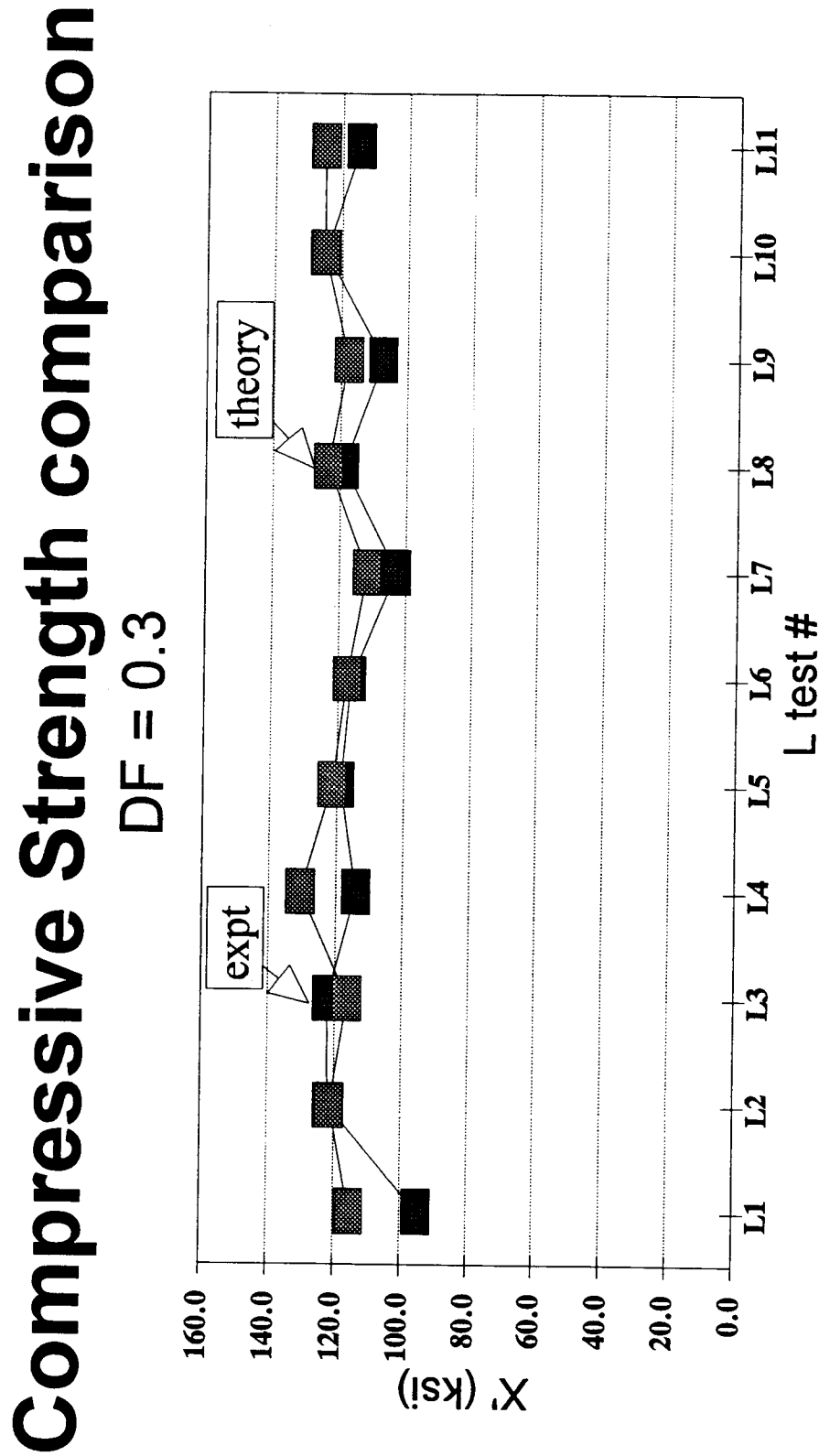

Figure 24. Plot of compressive strength comparison from theory and experiment with DF = 0.1 for a $[45/0/-45/90]_{16}$ layup.

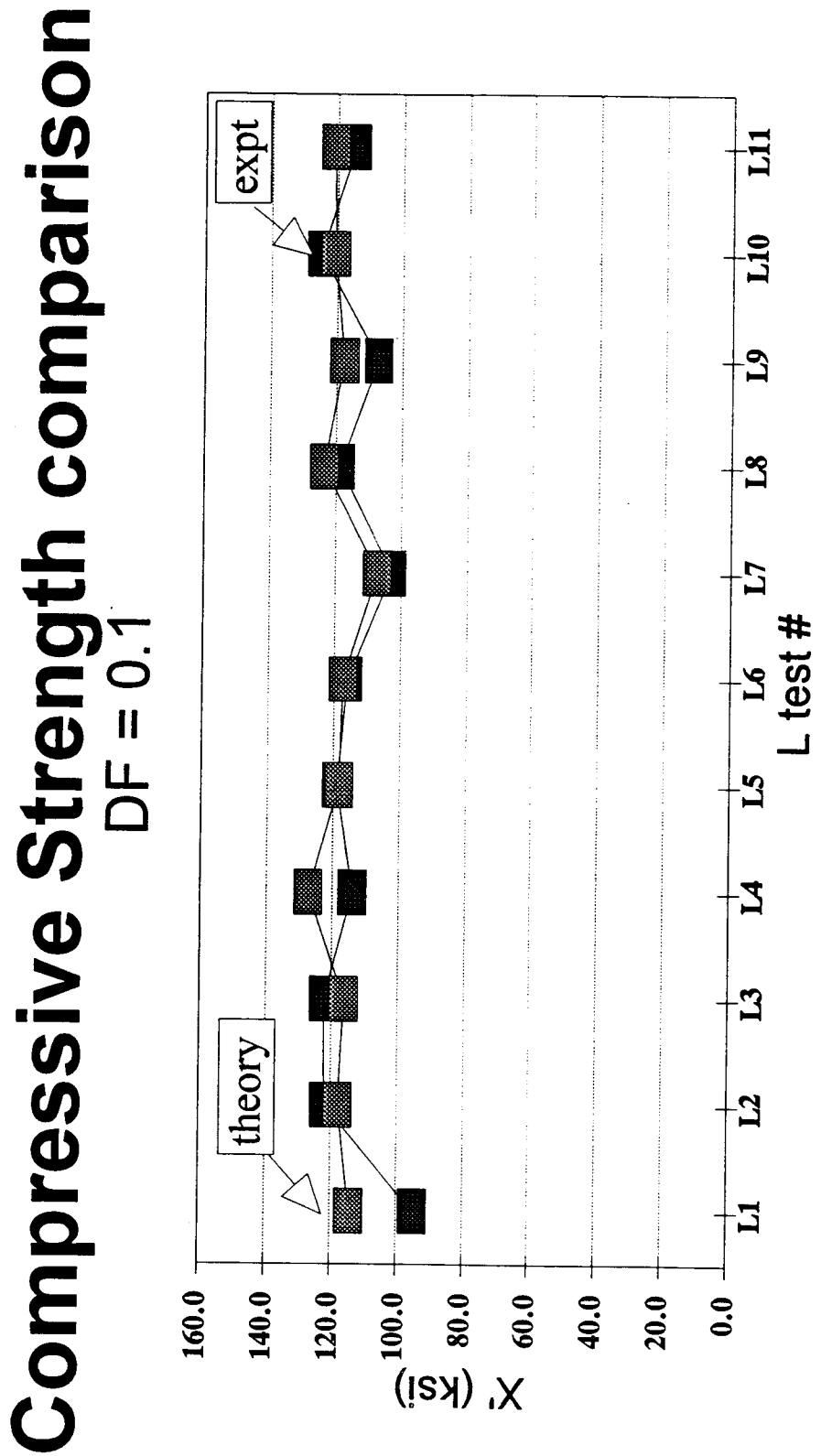

Figure 25. Plot of compressive strength comparison from theory and experiment with DF = 0.2 for a $[45/0/-45/90]_{16}$ layup.

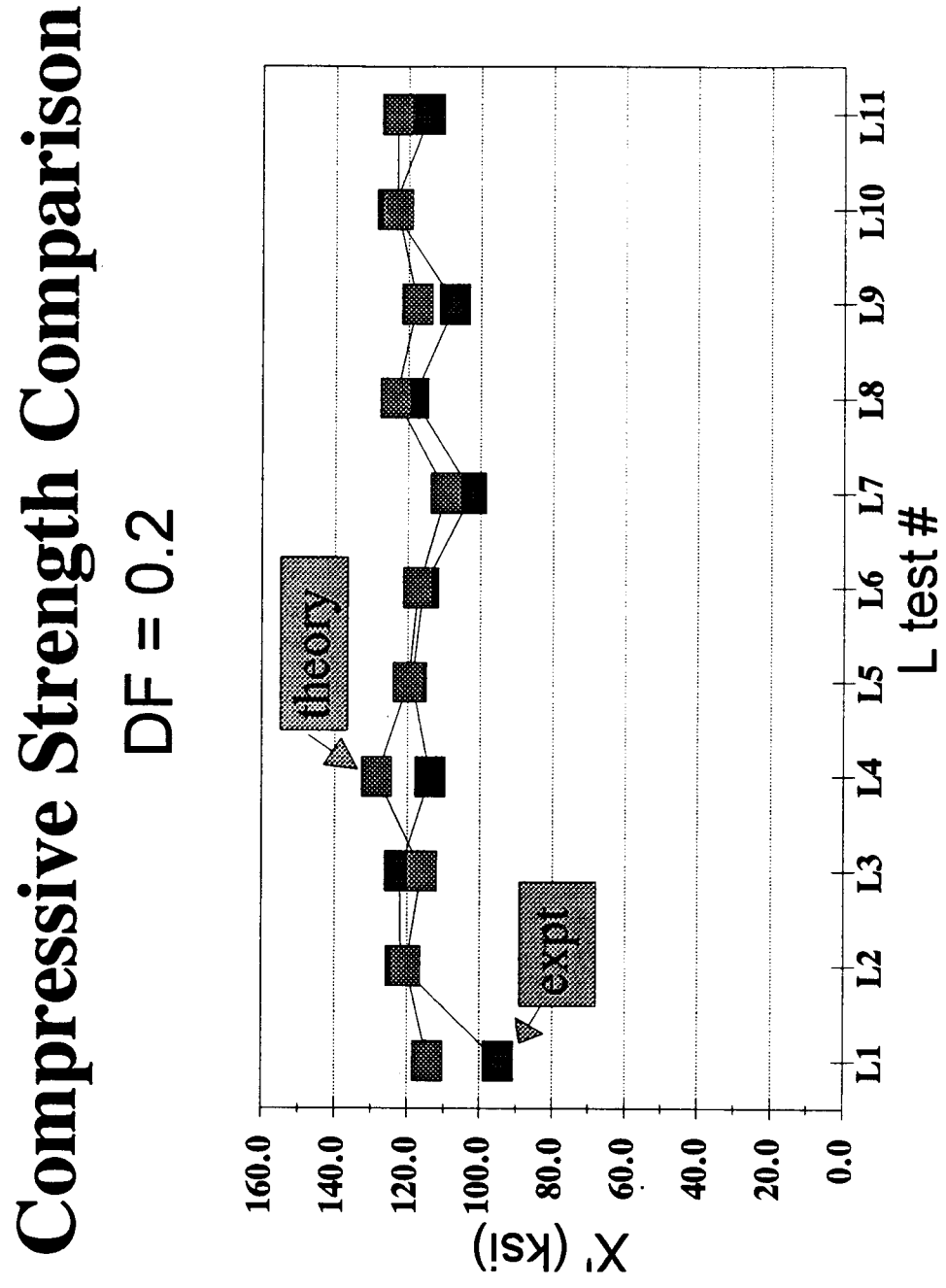

4.2 Strength Curves

The strength of unidirectional composites for a given state of stress can be obtained from solving equation 4. A reduced form of the equation considering orthotropic failure criterion in equation 4, becomes a generalization of the von Mises criterion with F*xy = -1/2. With these considerations the equation in stress takes the form:

$$\sigma_x^2 / F_y - \sigma_x\sigma_y / \text{sqrt}(F_{xx} F_{yy}) + \sigma_y 2 / F_{xx} = 1 / F_x F_y \qquad (27)$$

this is in the form of an elliptical equation, reducing using constants, becomes:

$$A*\sigma_x^2 - B*\sigma_x\sigma_y + C*\sigma_y 2 = D \qquad (28)$$

where $A = 1 / F_{yy}$ $B = 1 / \text{sqrt.}(F_{xx} F_{yy})$

$C = 1 / F_{xx}$ $D = 1 / F_x F_y$

with F_{xx}, F_{yy} expressed in strength terms as derived in equations 10 - 16. Calculating constants A, B, C and D using measured experimental data and then converting into polar coordinates the final form of the equation 28 becomes:

$$r = \text{sqrt.}\{ D / A * \text{Cos}^2\theta - B * \text{Sin}\theta * \text{Cos}\theta + C * \text{Sin}^2\theta \} \qquad (29)$$

where $\sigma_x = r * \text{Cos}\theta$ $\sigma_y = r * \text{Sin}\theta$

Now for θ varying from 0 to 360 degrees, the radius r was found in steps of one degree. Subsequently σx and σy were calculated.

Figure 26. Strength curve for a Gr/BMI laminate in resultant stress space for a $[0/90]_S$ layup after L5 exposure.

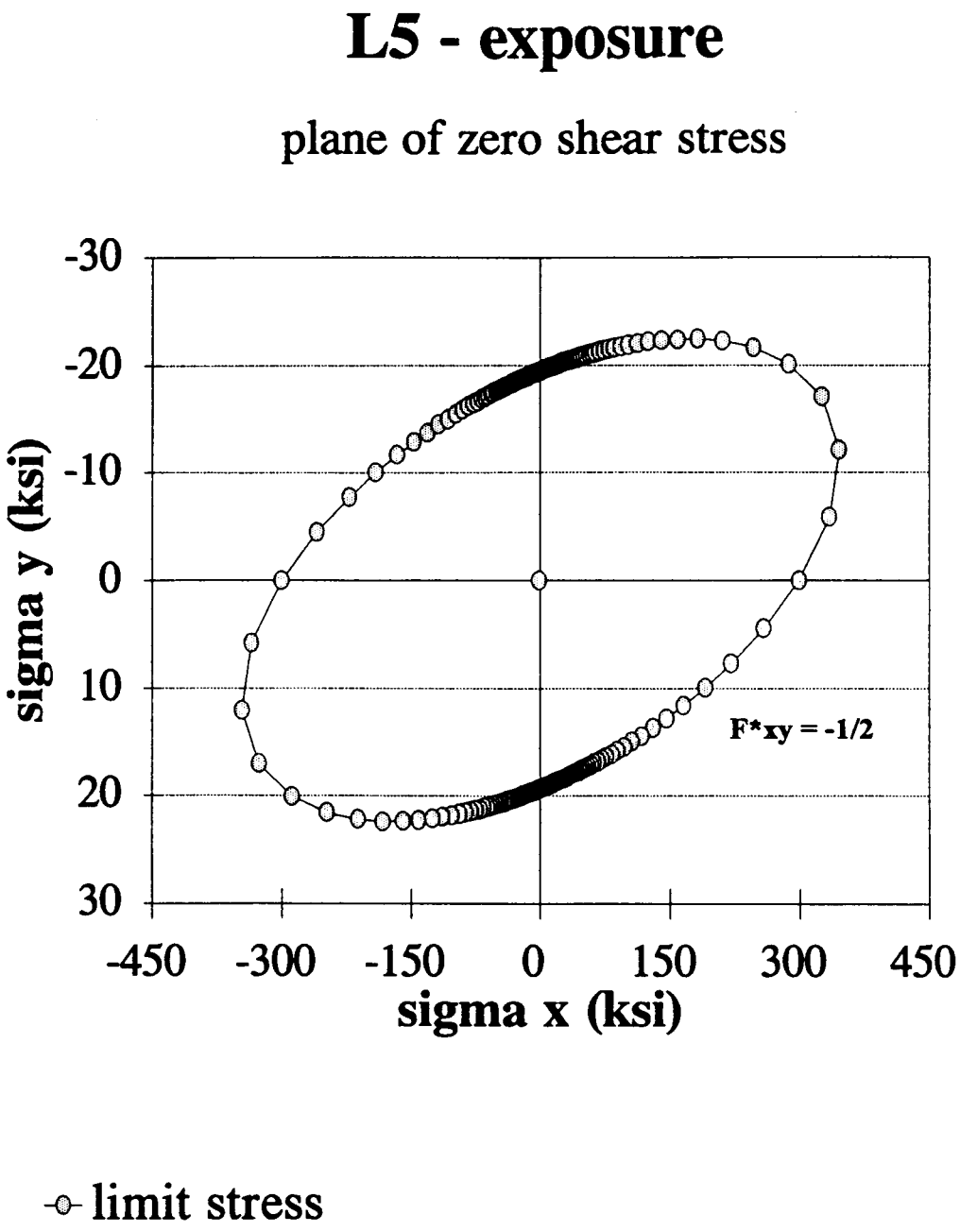

A program listing in C language for radii calculation with varying theta appears in Appendix 3. A plot of the normal stresses in x and y, with unit stress vector (1,1,0) gave the allowable strength curve. A typical curve drawn in zero shear stress plane is shown in Figure 26. It is seen that in stress-space, the material is anchored by four focal points, which are the intercepts of stress axes. These points represent the allowable stress limits in tension and compression respectively. The tensile failure would occurs at 422 ksi and the compressive failure at 22 ksi. Any point within the locus is considered a safe state of stress in x and y. This holds for any sequence of unidirectional layup of the laminate with appropriate exposure. This means the case assumes equal applied stresses both in x and y to the laminate. From experiment only the measured limit strength values for a paticular layup may be obtained. The theoretical stress plot gives a closer representation of strength because it considers the interaction parameter. Similar plots for exposures L1 - L11 appear in Appendix 3.

Table 11. Calculated Coefficients of Equation 28 For Each Exposure

Exposure #	A	B	C	D x e6
L1	458.35	6014.6	78925.0	36175.45
L2	376.74	5269.65	73705.45	27769.16
L3	374.73	5586.22	83276.15	31205.87
L4	375.76	6115.2	99520.16	37395.67
L5	376.16	5808.41	89691.1	33737.67
L6	389.66	5416.25	75401.7	29335.79
L7	463.25	6096.13	80222.01	37162.85
L8	317.97	5210.81	85394.13	27152.54
L9	281.17	4579.64	74592.35	20973.13
L10	301.19	5120.13	87041.84	26215.69
L11	104.4	3173.55	96471.77	10071.39

4.3 Finite Element Modeling

A finite element model was developed using COSMOS/M finite element software. The purpose of the model was to simulate compression loading as applied during experimental conditioning of the specimens. The variation of stress and strain over the length of the specimen was observed. This is an important requirement from an experimental viewpoint, because if stress distribution were not uniform, the calculated properties will not be accurate and consistent. Also repeating the loading procedure for large number of different specimens will be questionable. Since this would be rather combersome experimently a FEA model was necessary.

With the above considerations and assuming close to ideal conditions a 2D model was developed using geostar. The model assigns orthotropic properties based on elastic moduli in two directions and Poisson's ratio. Model assumes no edge effects. Further the model holds only for plane stress situations. Its features are as follows:

Element type : Shell4l was used for the purpose. It is a 4-node multi-layer quadilateral shell element with membrane and bending capabilities. Six degrees of freedom (three translations and three rotations) per node are considered. A 205-node 160 element sketch appears in Figure 25 for a $[90]_{16}$ layup.

Boundary Conditions considered for problem setup: One end was fixed (zero degree of freedom), no translation in Z-direction and no rotations in X and Y-directions. Another case with rotation only in Y was also modeled.

Loading: Pressure equal to 45% of the applied stress during an L5 run (5510 psi) was applied at one end of the specimen as shown in Figure 25.

Figure. 27 The 205-node, 160 element finite element model.

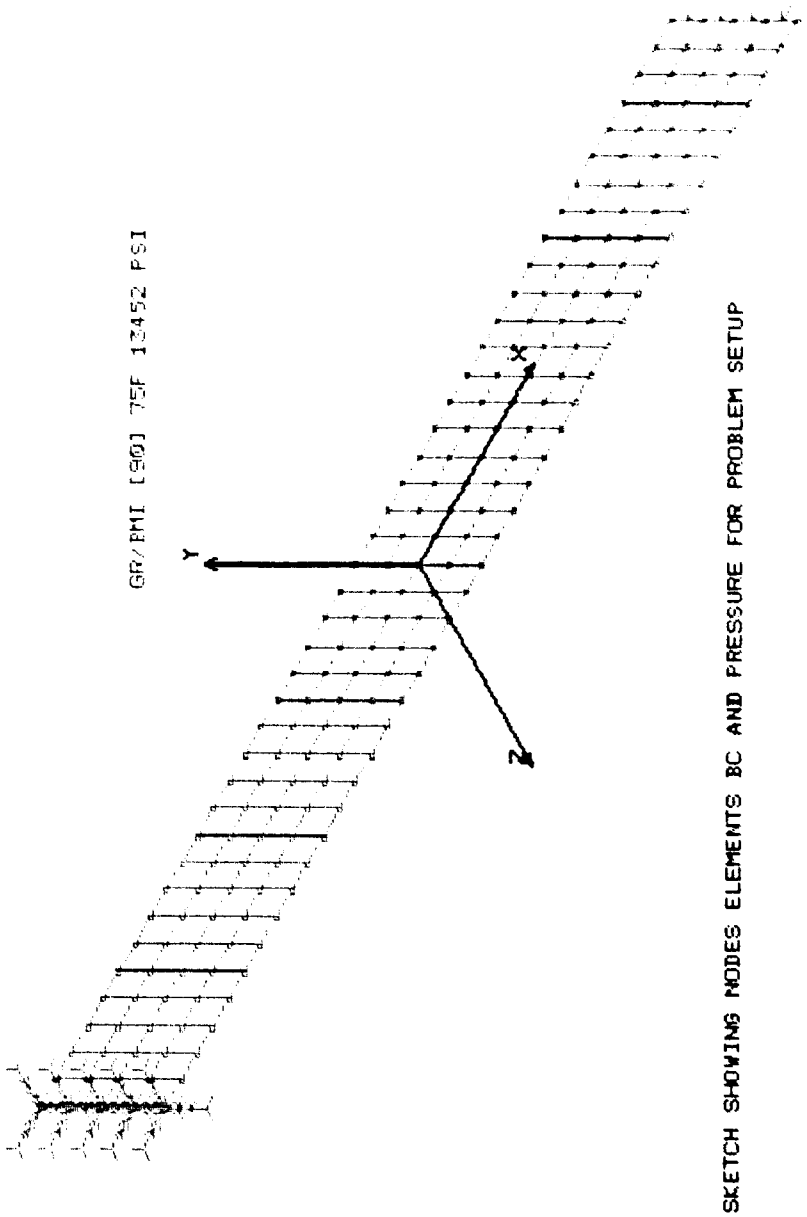

Figure 28. von Mises stress distribution plot for a $[90]_{16}$, L5 exposure Gr/BMI laminate.

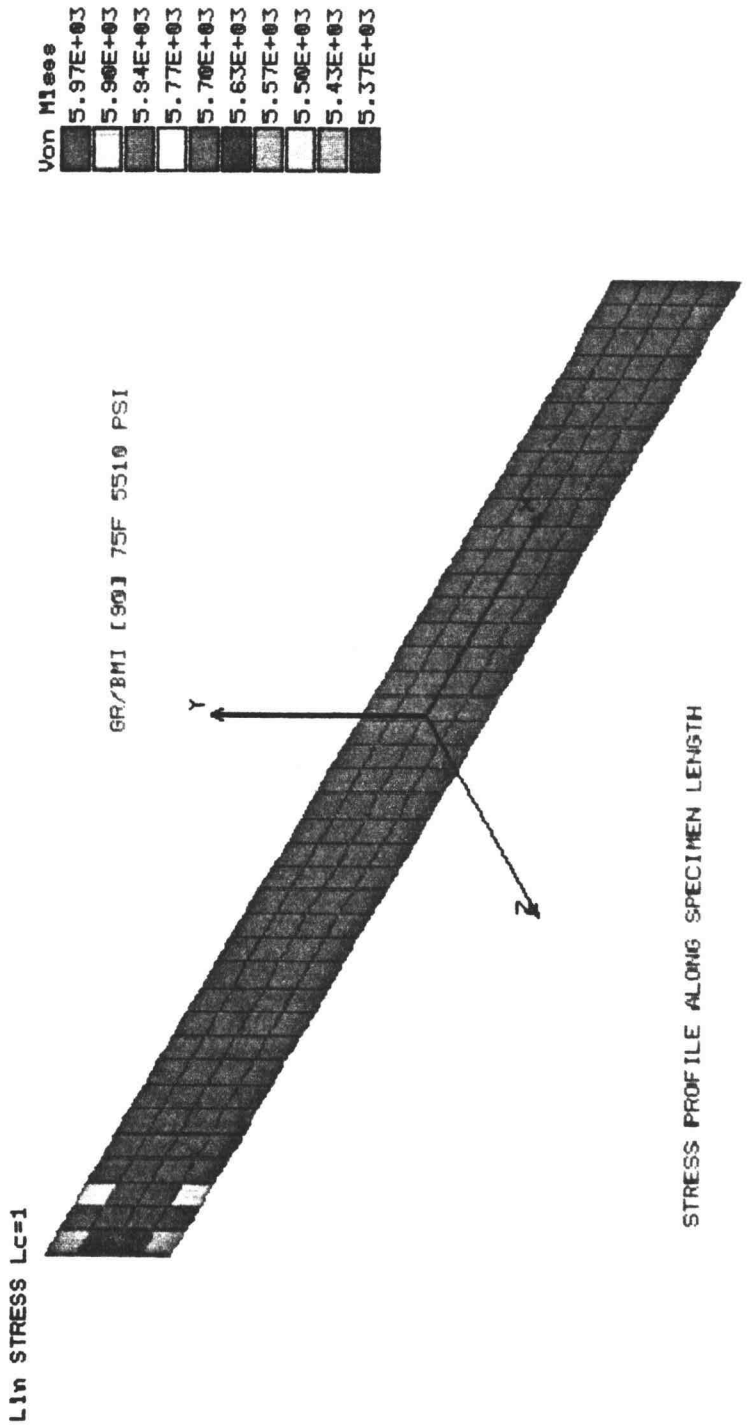

Figure 29. von Mises stress distribution plot for a $[90]_{16}$, L5 exposure Gr/BMI laminate (with rotation in Y-direction only)

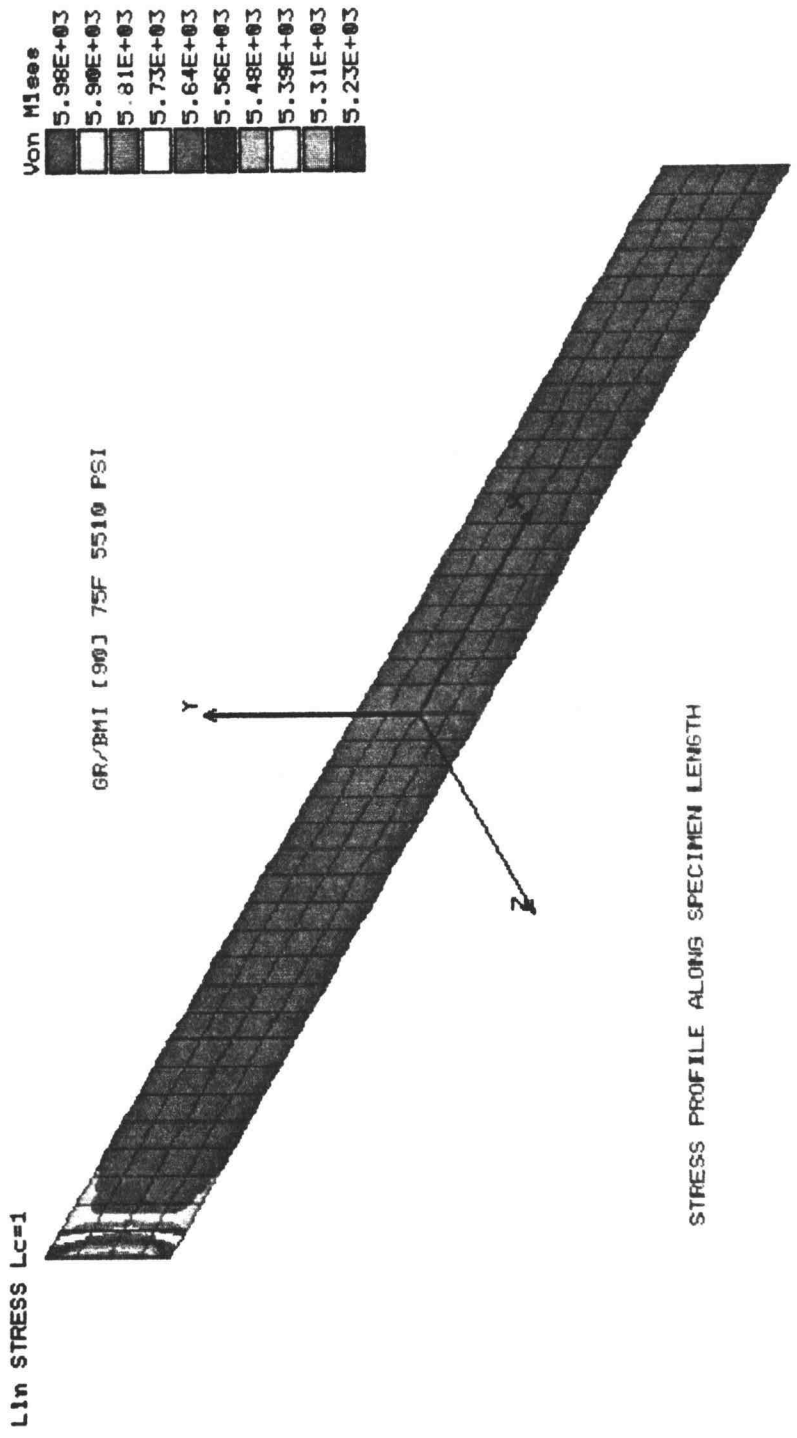

Figure 30. Sigma x - stress distribution plot for a $[90]_{16}$, L5 exposure Gr/BMI laminate.

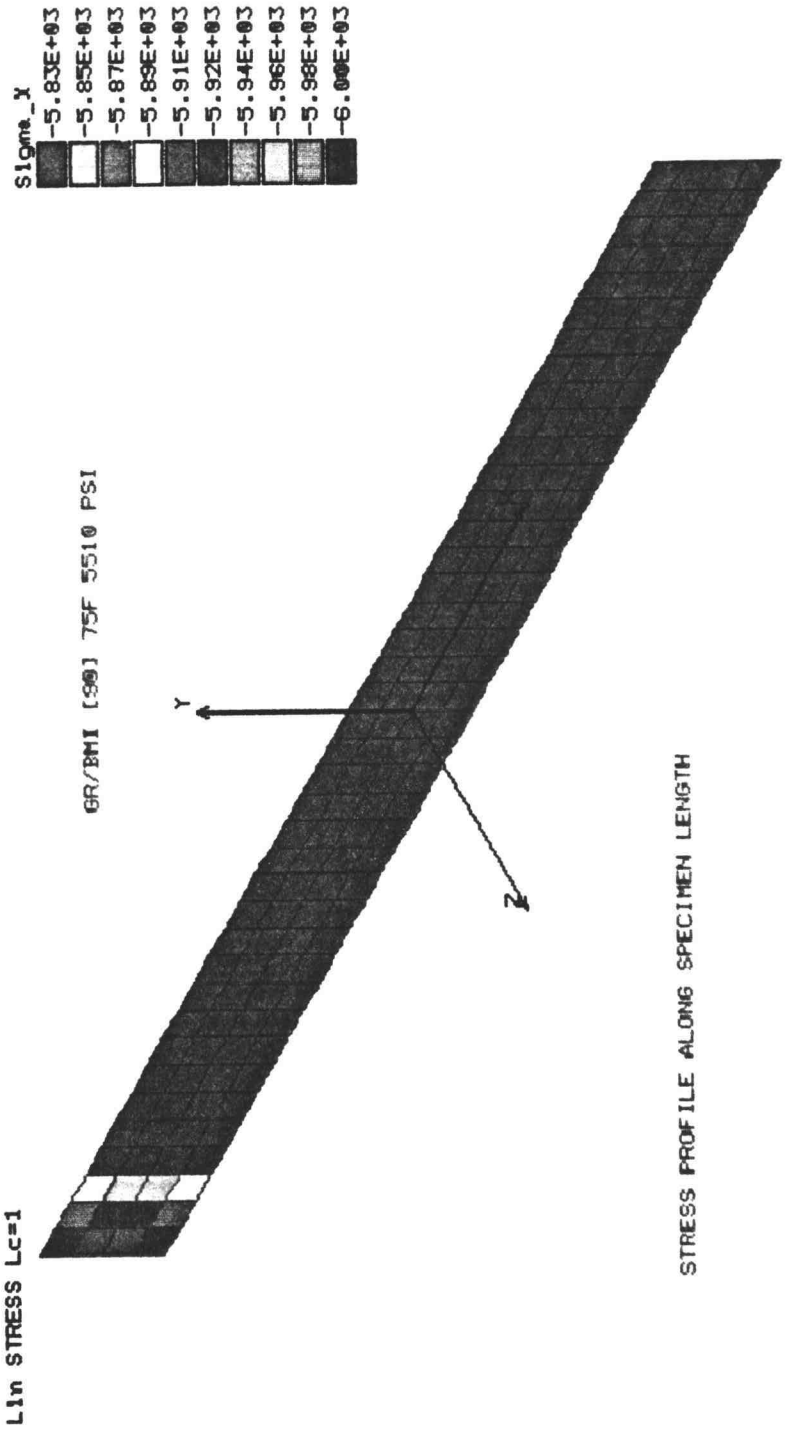

Figure 31. Sigma x - stress distribution plot for a $[90]_{16}$, L5 exposure Gr/BMI laminate (With rotation in Y- direction only).

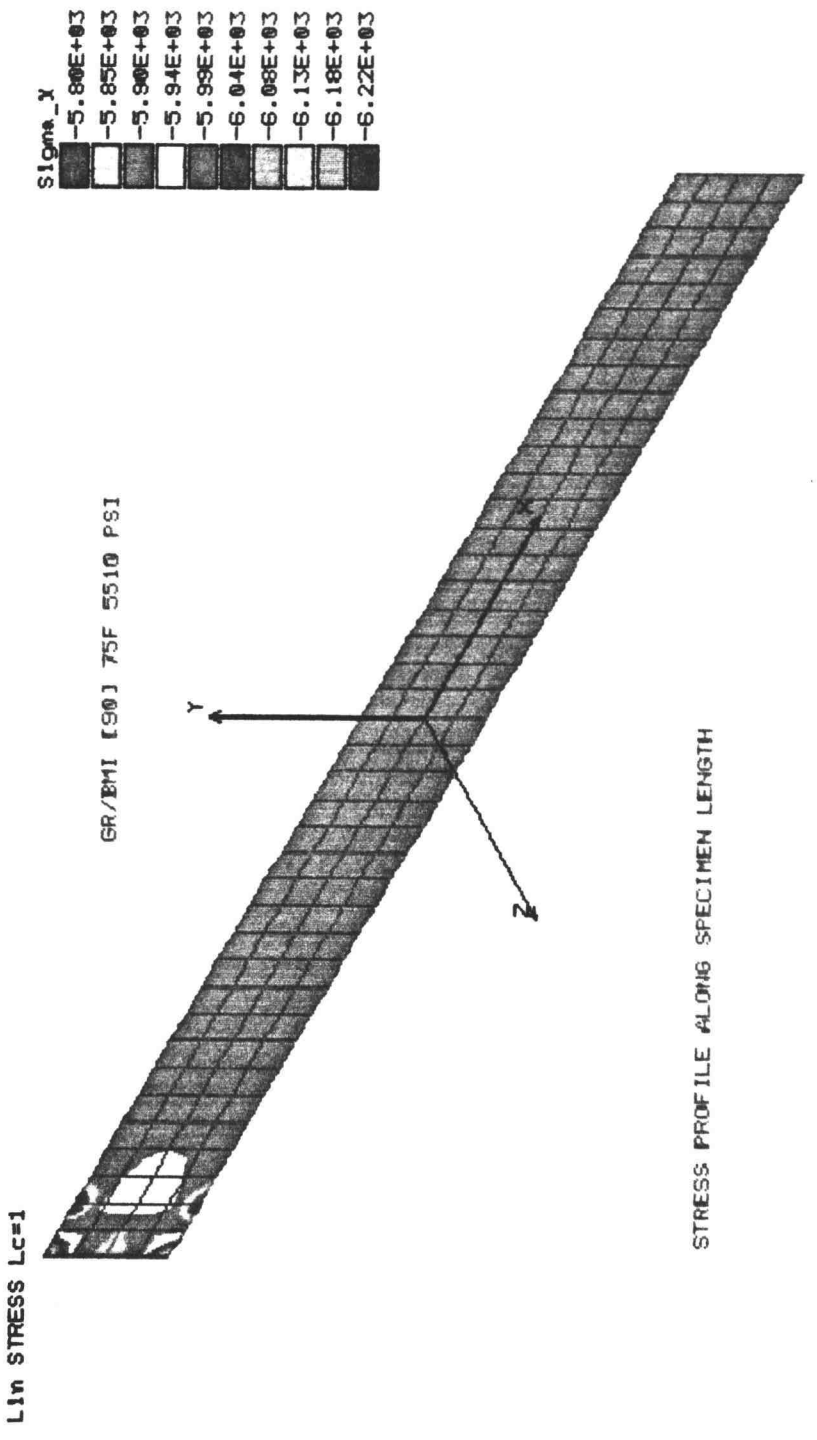

The model also considers all the nodes to be at a uniform temperature of 75° F. Static runs were made for $[0]_8$ and $[90]_{16}$ layups and the output in the form of stress, strain and displacement plots obtained.

Figure 28 shows the von Mises stress distribution for a $[90]_{16}$ layup. von Mises stress, $\sigma^2 = \sigma_x^2 - \sigma_x\sigma_y + \sigma_y^2$ is equal in magnitude to sigma x as stresses in y being minimal are neglected. Then the maximum stress for the model case is equal to sigma x (compressive) and is evident from the plots. It is seen that the stress varies from a maximum of 5.97e3 psi at the loading end to a minimum of 5.37e3 psi at the clamped end. The range is about 10% and is within that allowable for experimental constraints. The stresses developed are close approximations and are within the failure stress limit of 8.3e3 psi. A closer picture of the true stresses developed can be obtained if stress distribution through the specimen thickness can be represented. The rest of the specimen was found to have uniform stress distribution, this being for the first case where rotations both in X and Y directions were suppressed. Figure 29 shows the same plot for the case of rotation only in Y. The stress distribution is similar in terms of magnitude, but varies much more at the clamped end due to the extra degree of freedom. The remaining specimen length, however, experiences uniform stress distribution. Plots of sigma x for the two cases appear in Figures 30 and 31 respectively. It is equal in magnitude to the von Mises but compressive, implying that most of the stress occurs in the loading direction. This goes well with the experimental requirement. A code listing of the program along with similar plots for higher load levels and different layups appear in Appendix 4 of this report.

4.4 Photomicrographs of Tested Specimens

Metallographic techniques involved in the specimen preparation, polishing and microstructural examination procedures as outlined in [15] were applied to four different layups, namely $[0]_8$, $[90]_{16}$, $[+/-45]_{16}$, and $[45/0/-45/90]_{16}$ respectively. This was undertaken to study possible failure modes with respect to specimen history and orientation. Also size and distribution of flaws such as voids, inclusions, fiber misalignment and ply distortion could be observed. Common failure related damage modes such as microcracks, microbuckling, delamination, debonding and fiber pullout could also be observed. Additionally, it would serve as a basis for failure analysis. A typically mounted specimen appears in the photograph in Figure 30. For each layup, two sets of specimens were prepared. Observations were made using standard optical microscopes and photos were taken using Image Analysis setup in the Advanced Materials Lab at Oregon State University. A table listing the observations along with related micrographs follow:

Figure 32. A typically prepared/polished Gr/BMI specimen.

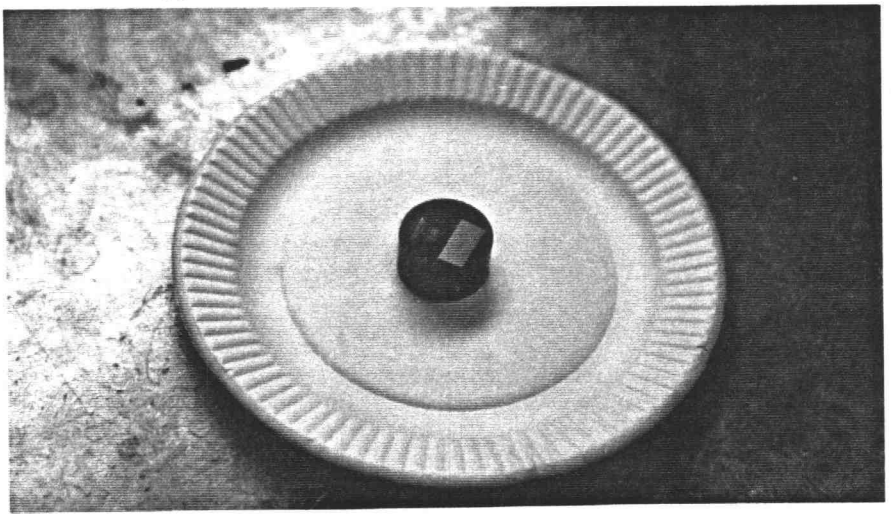

Table 12. Observations and Remarks on Individual Photomicrographs

micrograph #	Observations	Significance
1	Visible voids, fiber scatter and breakup. Large resin rich areas	Indicative of fiber depletion around in and around the area. Shows extent of fiber pullout and damaged area.
2	One section reveals region devoid of fibers, the other shows fiber/matrix interface breakup in the area	Indicative of extent of fiber pullout in the region and crack propagation through the laminate
3	Microstructure shows extensive crack propagation through the matrix and distortion in individual plies, with band-like formation	Fracture surface indicative of matrix cracking leading to probable inter- laminar failure, eventually leading to failure by microbuckling
4	Microstructure at one section reveals crack propagation across a individual ply and other shows extent of distortion of the layers	Fracture surface indicative of crack propagation through fibers across layer width, leading to eventual compression failure of the laminate

Figures 33 and 34. Photomicrograph 1.
Gr/BMI composite laminate of unidirectional $[0]_8$ layup.
Conditioning history - 1251 lbs cyclic load, uniform temperature of 75° F for 2000 hours. Standard specimen preparation and polishing. Un-etched specimen at a magnification of 630X. Microstructure shows fractured fiber ends across laminate fracture surface with voids. Indicative of fiber pullout.

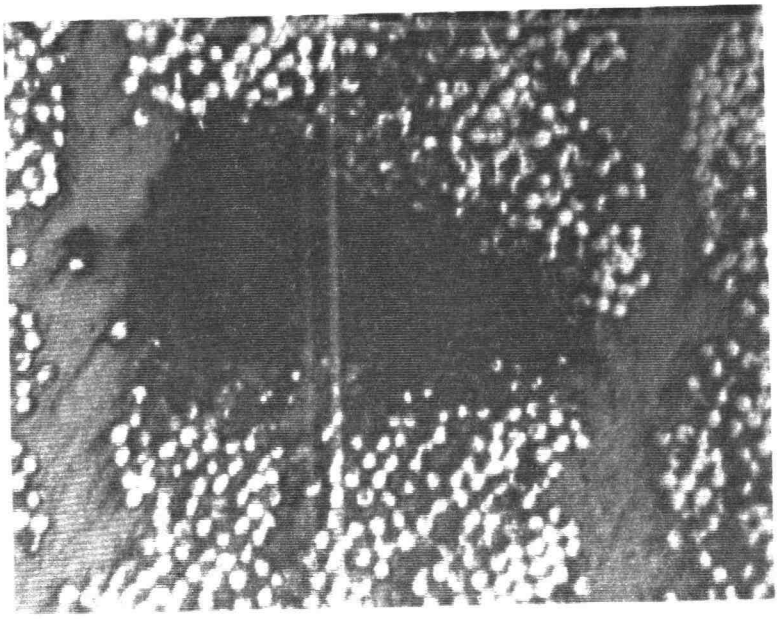

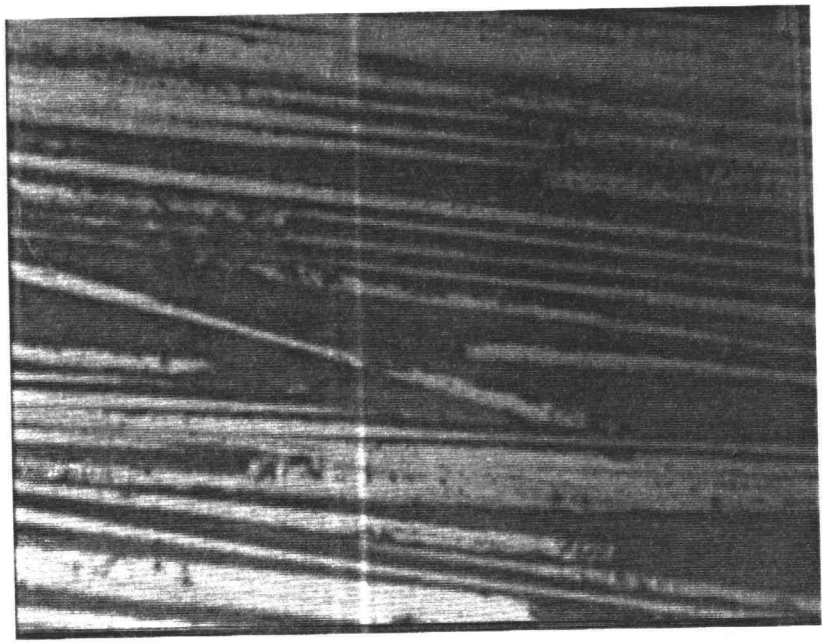

Figures 35 and 36. Photomicrograph 2.
Gr/BMI composite laminate of transverse $[90]_{16}$ layup.
Conditioning history - 1251 lbs cyclic load, uniform temperature of 75° F for 2000 hours. Standard specimen preparation and polishing. Unetched specimen at a magnification of 630X. Microstructure shows fracture markings at fiber/matrix interface, with fracture surface having large voids indicative of fiber pullout.

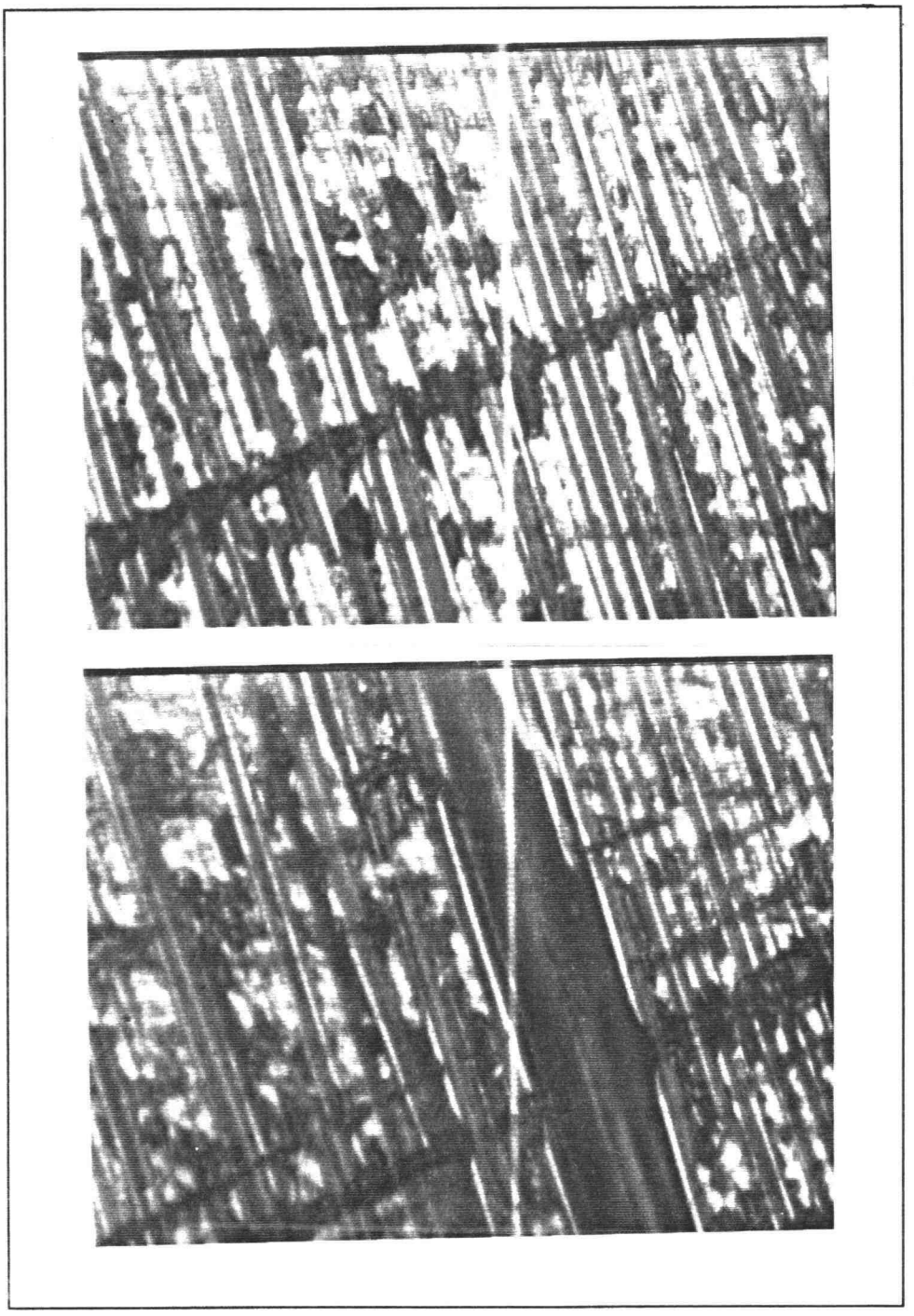

Figures 37 and 38. Photomicrograph 3.
Gr/BMI composite laminate of $[+/-45]_{16}$ layup.
Conditioning history - 2501 lbs cyclic load, uniform temperature of 75^{o} F for 2000 hours. Standard specimen preparation and polishing. Unetched specimen at a magnification of 100X. Microstructure features matrix cracks running across the laminate and distortion of plies indicating of interlaminar damage.

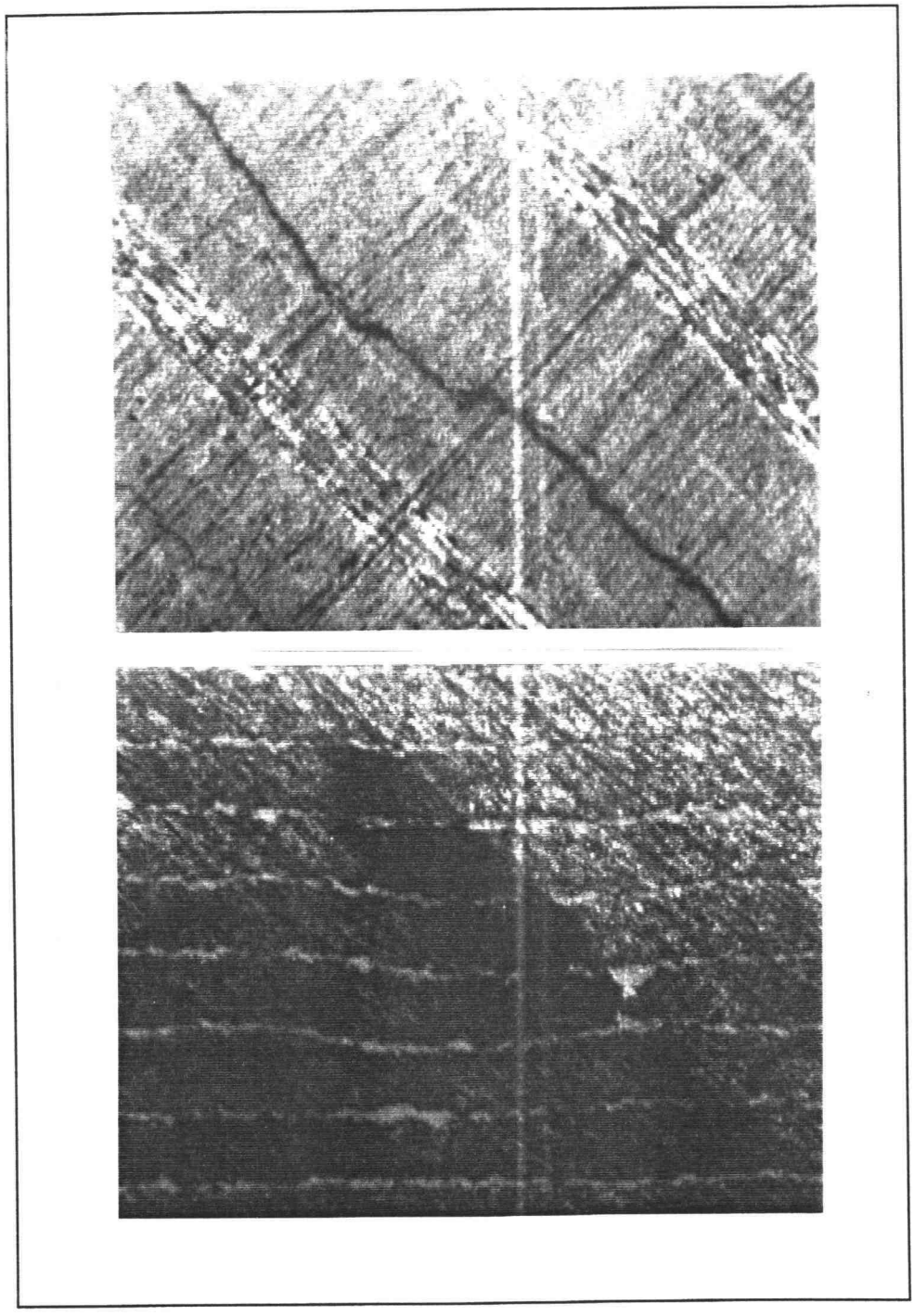

Figures 39 and 40. Photomicrograph 4.
Gr/BMI composite laminate of $[45/0/-45/90]_{16}$ layup.
Conditioning history - 2501 lbs cyclic load, uniform temperature of 75^{o} F for 2000 hours. Standard specimen preparation and polishing. Unetched specimen at a magnification of 250X. Microstructure features a delamination crack running through an individual ply across its width, the extent of ply distortion is also seen - indicates interlaminar damage.

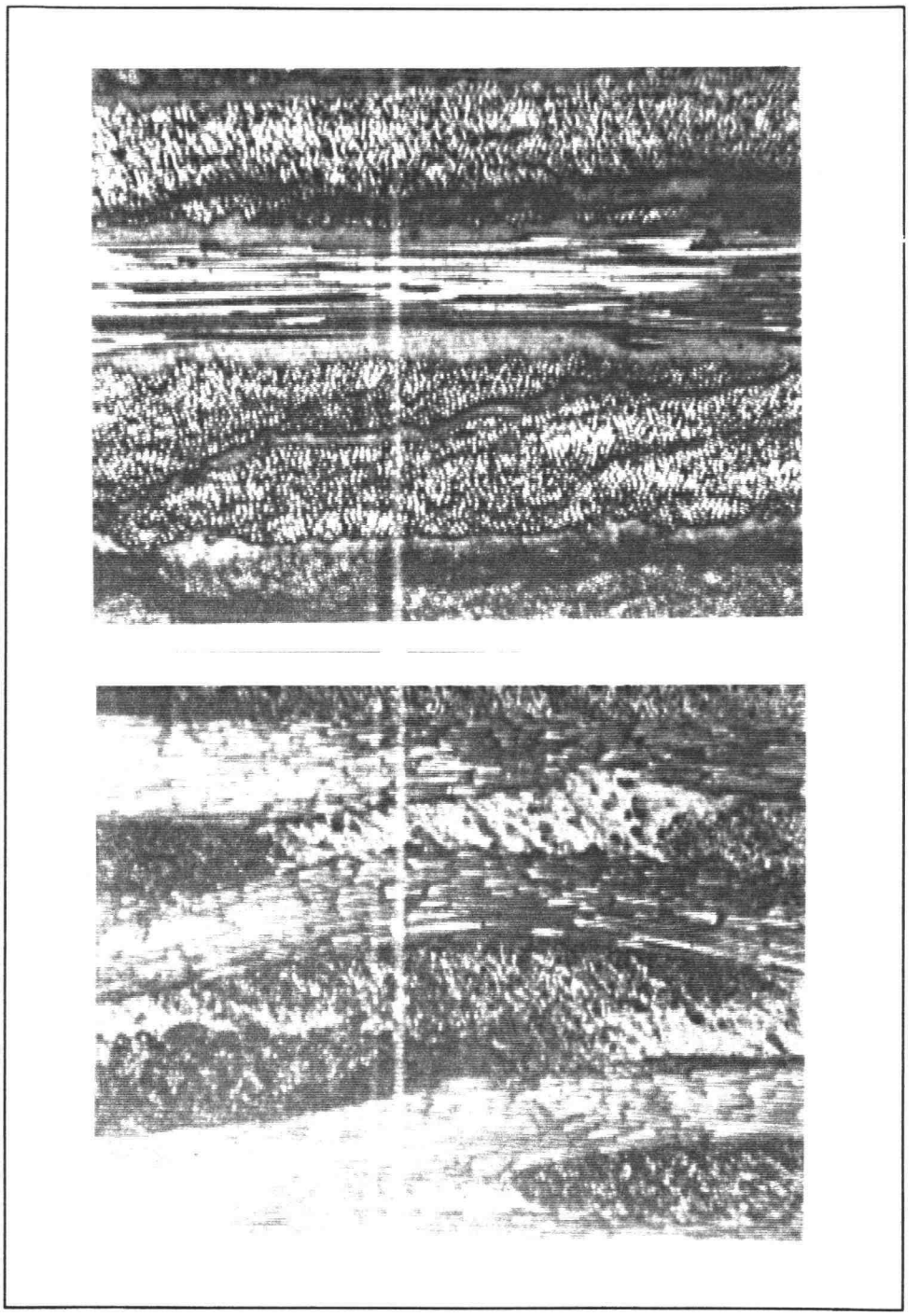

Observation of fracture surfaces of different layups gave interesting results supporting some of the common failure modes of unidirectional and crossply laminates. In the 0-degree and the 90-degree layups, both unidirectional in nature, two prominent features were evident. One was voids and two, the extent of fiber pullout with surfaces markings on the fiber ends. This was more extensive in the latter layup. This could be because fibers in the $[90]_{16}$ layup are transversely oriented and are weak in the loading direction. For the $[0]_8$ layup, however, the extent is minimal because its fibers are oriented in the loading direction.

Microstructure of polished surfaces of cross-ply laminates showed distinctive columnar-type feature as seen in the micrographs of Figures 35 and 36. In the $[+/-45]_{16}$ layup these are observable as cracks propagating throughout the matrix, which has the effect of distorting individual plies in a kink band-like formation. This subjects the fibers to microbuckling, eventually leading to interlaminar failure. In this case the fiber orientation is in the direction of shear. This makes the laminate strong in shear but comparatively weaker in the axial direction. With continued loading these fibers tend to reorient themselves in the loading direction eventually leading to interlaminar failure. The $[45/0/-45/90]_{16}$ layup, on the other hand consists of both uni and cross directional plies. Similar failure mode is observed, only now it is restricted within individual plies constituting the laminate. Due to this the distortion is limited. Depending on the least dominant of the ply, axial loading would lead to its failure for similar reasons. Another observable feature is that the cracks, as they propagate through the laminate, increase in size. This is seen in Figures 37 and 38. This indicates, after initial failure of a ply, with continued loading

the laminate strength is reduced. This is damage- related information and helpful in laminate failure-analysis. In actual practice, however, laminate failure occurs due to a combination of failure modes depending on several conditions such as conditioning history, residual stresses during fabrication etc.

5. Conclusions and Suggestions for Future Work

The following conclusions can be drawn from this research:

5.1 Experimental Method of Conditioning Large Number of Specimens

Advantages:

a) The compression loading method provides for the conditioning of 20 or more specimens at a time individually in self-contained channels, allowing for simultaneous variation of load and temperature. This has been currently modified to include another variable - namely, high moisture - and has been found to be successful.

b) The method is particularly applicable when large number of specimens, exceeding upwards of 300, have to be conditioned in a given period of time. The number of specimens required is high because a variety of properties are obtained from similar sets of specimens. For example, in addition to giving the usual mechanical properties after the exposure, during the conditioning strains are also recorded to study creep properties.

c) Additionally, a metal trough was designed and constructed to improve heating and cooling times, especially for the cyclic exposure. This did take longer during earlier cycles, but was overcome by allowing the trough to heat from cold prior to actual conditioning cycles. It also allowed for use of extra number of specimens; those that needed oven exposure at 300^{o} F could now, instead, be fixed in the trough under similar conditions.

d) The loading method is unique and simple, employing leverage principle to bring specimens to desired the load level. It uses commercially available materials and the mechanism is straight forward as discussed in the experimental section.

e) It is cost effective, in that the channel housing, fixtures, heating and cooling units and the containment areas can be easily modified to include other environmental variables. A jet fuel atmosphere is currently under development.

f) The experimental method of conditioning is proven to be safe and reliable with the inclusion of various safety mechanisms discussed earlier, and the fact that 300 specimens have been successfully conditioned over a five month period.

Limitations:

a) Sometimes test interruptions were necessitated due to problems of premature failing of some specimens by brooming, where only the specimens ends failed.

b) Another limitation initially was not knowing the stress limits of the Gr/BMI at 300^{o} F which necessiatated for more baseline testing and extra specimens.

Future work could include increasing the capabilities of the specimen conditioning system in terms of load and temperature and optimizing the system in terms of reducing interruptions due to premature failure of specimens. This would mean additional modifications to the fixture specially those that see high temperature. The metal trough could be modified to include moisture variable using vacuum bagging. The system reliability can be compared under different environmental conditions such as dry air, salt water, high humidity, jet fuel etc.

5.2 Correlation Between Theory and Experimental Strength/Modulus Properties

The experimental data agreed well with those predicted using Genlam for compressive strength. For tensile modulus and strength, however, there were some discrepancies for certain L - runs as discussed earlier. This could be made better by having closer tolerances on mechanical testing and using more specimens wherever possible. Also the software input could be modified to represent more closely the actual values of the Gr/BMI system. For example, the expansion coefficients used were those of Gr/epoxy. This could be done by measuring strains under temperature and then comparing them with the unstrained specimen. A change in expansion will effect the flow properties of the matrix and so the predicted strength. The strength curves provided another way of interpretation of strength data. Although simplified strength parameters were used in plotting them, they do give the range of safe stresses for a Gr/BMI laminate with respect to orientation. Closer experimental values and interaction parameters could be included to get more accurate stress ranges. Further work here could be in the direction of investigating possibilities for obtaining better correlation between theory and experiment. This would mean finding additional strength parameters and narrowing experimental errors.

5.3 FEA Modeling

The 4-node quadrilateral shell element was used to model individual plies of the laminate. Experimental-like conditions were simulated in the form of suppressing certain degrees of freedom, such as translation in Z and rotations in

X and Y directions respectively. Experimentally-measured strength values were input into the program. Upon running a static analysis, the model gave various stress distribution plots. The plots gave the von Mises stress distribution, the stress in loading direction, sigma x, the displacement and strain distribution both in axial and transverse directions. Stress distribution was found to be uniform other than at the ends, which is expected. The transverse stress was very low compared to axial stress. The shear and transverse strains were also much lower in comparison with the equivalent strain. The displacements were within allowable limits of experimentation. These results went well with the experimental requirements in providing very good basis for the loading method. Although the model was simplified to 2D, it did provide an insight into the material behavior during the conditioning period. Further work here could include developing a 3D model with an increased number of nodes and running a linear dynamic analysis to give closer results.

5.4 Microstructural Observations

The microstructural examination techniques used in determining fracture trends in individual specimens of various layups gave good results. The $[45/0/-45/90]_{16}$ suffered least amount of damage due to its characteristic layup. The $[0]_8$ layup had little fiber pullout, whereas the $[90]_{16}$ layup saw extensive pullout due to their fiber orientation. The $[+/-45]_{16}$, on the other hand, had microcracks running across the matrix, probably due to fiber reorientation. The technique discussed can be used as a quick way to inspect and describe composite trends/properties in general and particularly those relating to failure, as discussed earlier. Additional work here could include going into

nondestructive methods for property determination. Scanning Electron Microscopy techniques could be used for better results. These investigations also help in quality assurance and materials selection.

In conclusion, the objective of providing a solid base for experimental conditioning of large a number of specimens, along with mechanical property determination, was fulfilled. This, in turn, provided the database for predictions on the long-term response of the Gr/BMI composite material system.

References

1) W. C. Hansen, K. Shenoy and E. G. Wolff, "Residual Strength of Graphite/BMI Composites after Long Term Cyclical Compression," *Proceedings IX International Conference on Composite Materials,* Vol. 5 pp. 524 -531 (1993)

2) Wolff, E.,G., Hansen, W.C., and Shenoy, K, "Prediction of Creep Strains during Cyclical Compression of Composites, " *Proceedings VII International Congress on Experimental Mechanics,* Vol. I, pp. 178-182, The Society for Experimental Mechanics, Inc. (1992)

3) E. G. Wolff and T. C. Kennedy, "*Modeling of Structural Composites for the High Speed Civil Transport,*" Quarterly Progress Reports I - X submitted to Boeing Commercial Aircraft Company (1992 - 1993)

4) Tsai, S. W., "Composites Design" 4th Edition, *Think Composites*, Dayton, Ohio, (1988)

5) Tsai, S.W., Hahn, H.T., Introduction to Composite Materials, *Technomic Publishing Co. Inc.,* Lancaster, PA (1980)

6) Tsai, S.W., Wu, E.M., "A General Theory of Strength for Anisotropic Materials," AFML-TR-71-12 (1971)

7) Jones, R.M., "Mechanics of Composite Materials," *Hemisphere Publishing Corporation,* New York. (1975)

8) Chou P.C., McNamee B.M., and Chow D.K., " The Yield Criterion of Laminated Media "*Composite Materials in Engineering Design*, ASM 6th St. Louis Conference. p. 528 (1972)

9) Raghava, R.S., " Prediction of Failure Strength of Anisotropic Materials," *Reference Book for Composites Technology*, Vol. 2, p. 37 (1989)

10) Hansen, W.C., "The Significance and Measurement of Tsai-Wu Normal Interaction Parameter F12," M.S. Thesis, *Oregon State University*, October (1992)

11) Galasso, S. Francis., "Advanced Fibers and Composites," *Gordon and Breach Science Publishers,* New York . (1989)

12) Margolis, M. James., "Advanced Thermoset Composites," *Van Norstrand Reinhold Company,* New York (1986)

13) Grande, L. Donald., "High Speed Commercial Transport (HSCT) Structures and Materials," *Boeing Commercial Airplane Group* (1992)

14) Hashin, Z., "Failure Criteria of Unidirectional Fiber Composites," Journal of Applied Mechanics, Vol. 47, p. 329 (1980)

15) Johnson, A. Cornelius., "Metallography Princples and Procedures," LECO Corporation, Michigan (1989)

16) Anne, C. Roulin-Moloney., "Fractography and Failure Mechanisms of Polymers and Composites," Elsevier Applied Science, New York (1989)

17) Carlsson, A. Leif and Pipes, R. Byron., "Experimental Characterization of Advanced Composite Materials," Prentice-Hall, Inc., New Jersey (1987)

18) Bruins, F. Paul., "Polyblends and Composites," Interscience Publishers, New York (1970)

19) Biggers, S. B. and Chou, T. W., "Composite Materials in Transpotation Systems," ASME Winter Annual Meeting, Georgia (1991)

APPENDICES

Appendix 1.

Labview Program for Testing Tensile Specimens on the Instron 4505

Load Grapher 1.0

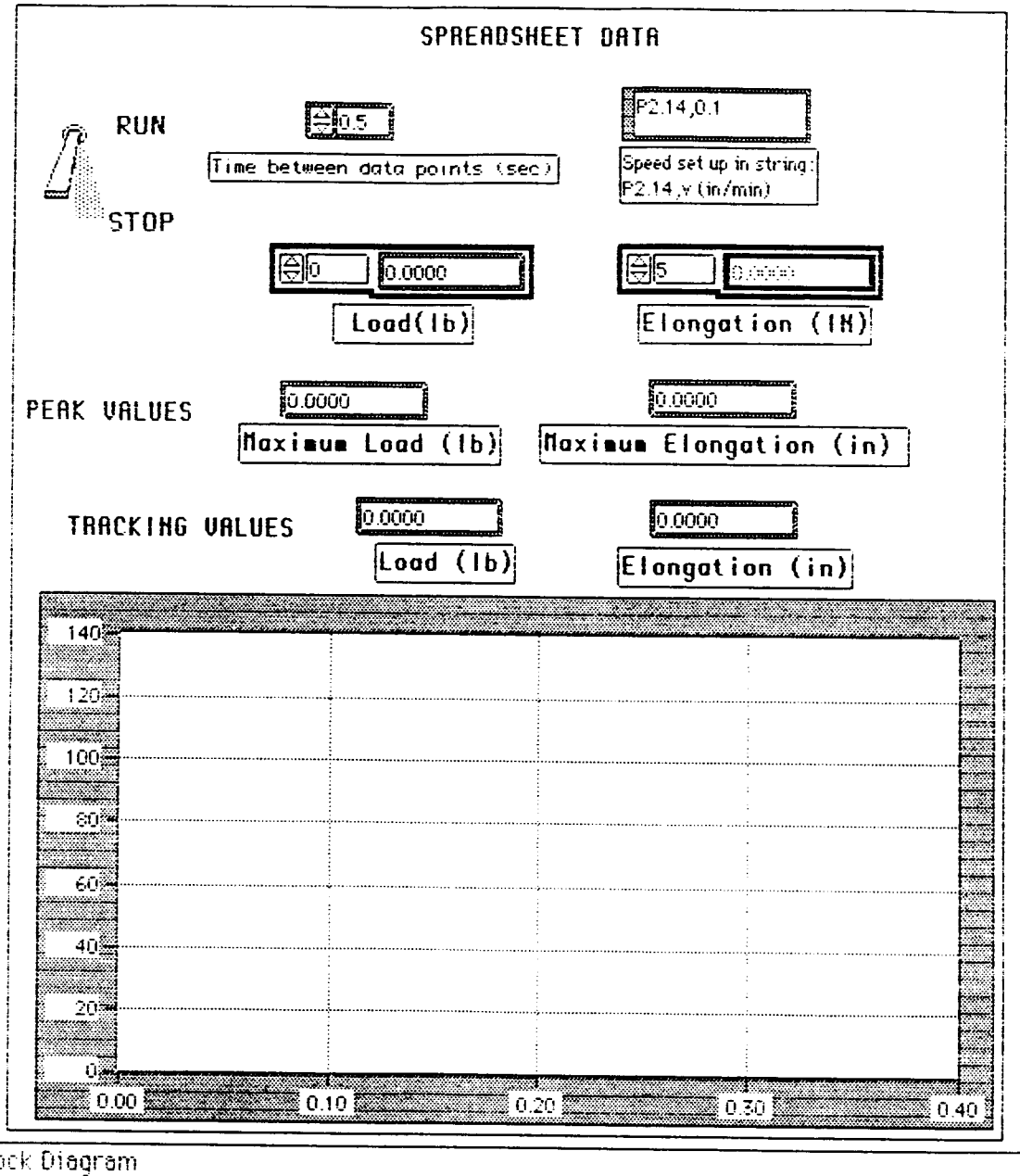

Block Diagram

Stress Grapher 4.0

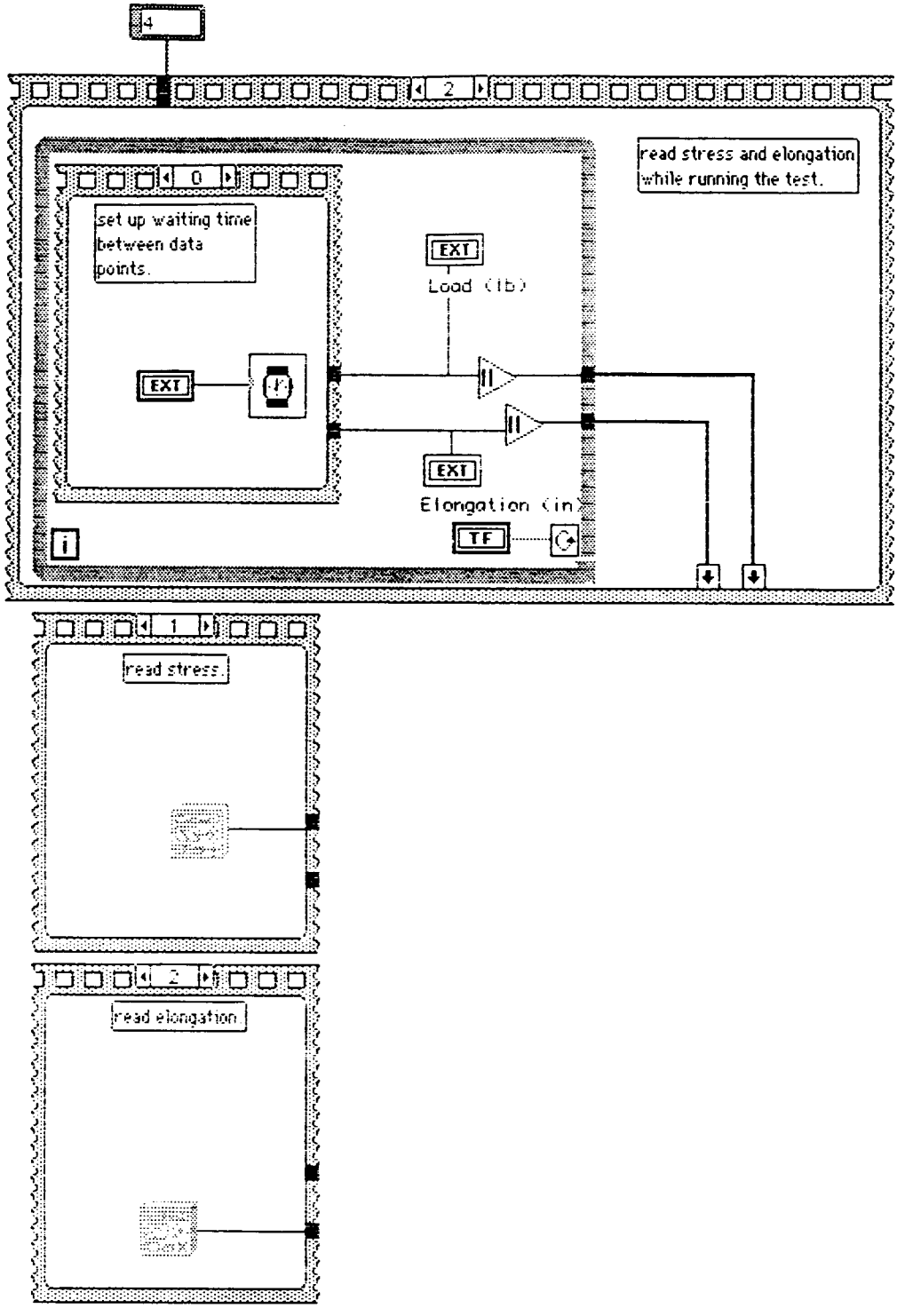

Stress
Grapher
4.0

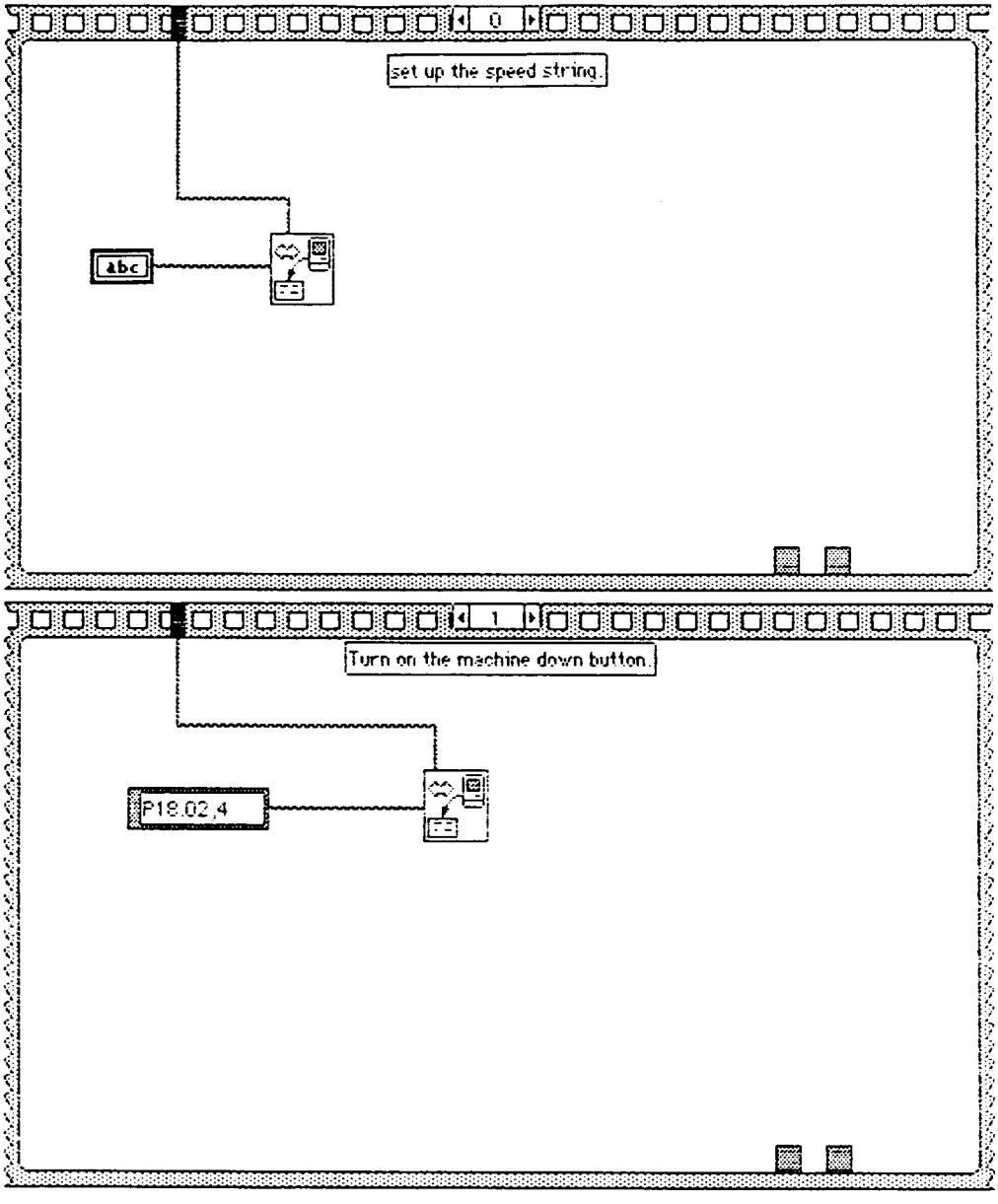

Load Grapher 1.0

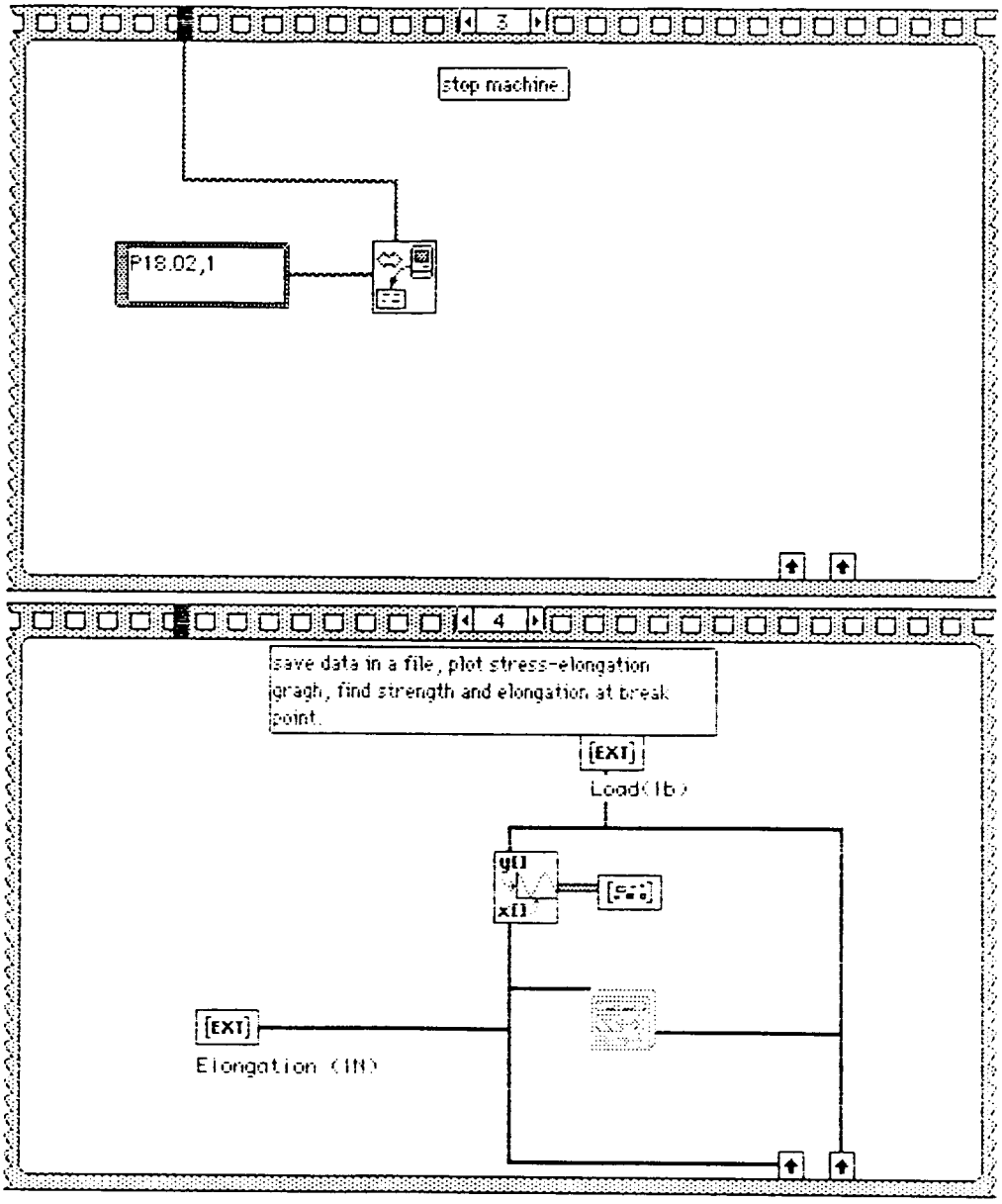

Load Grapher 1.0

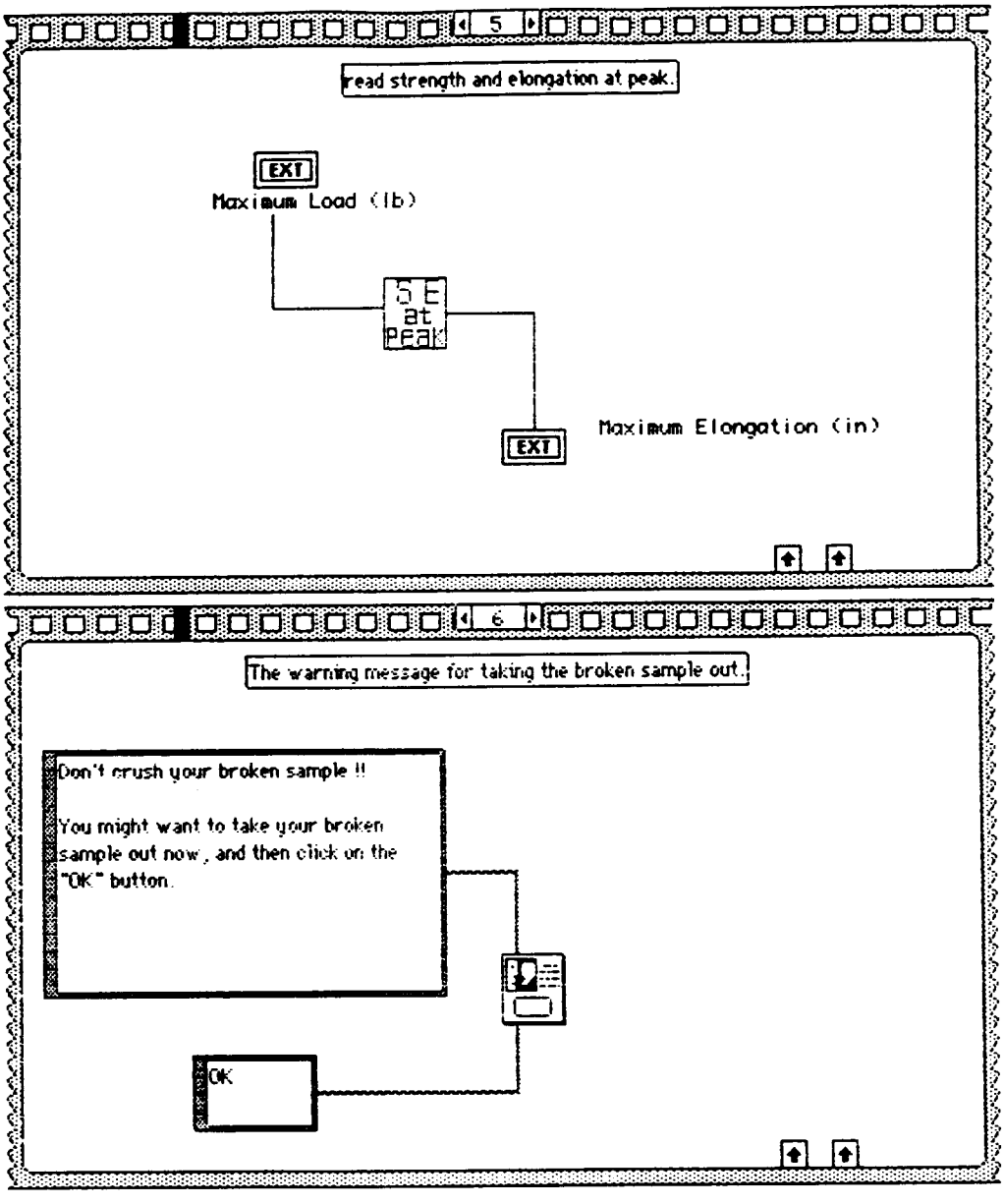

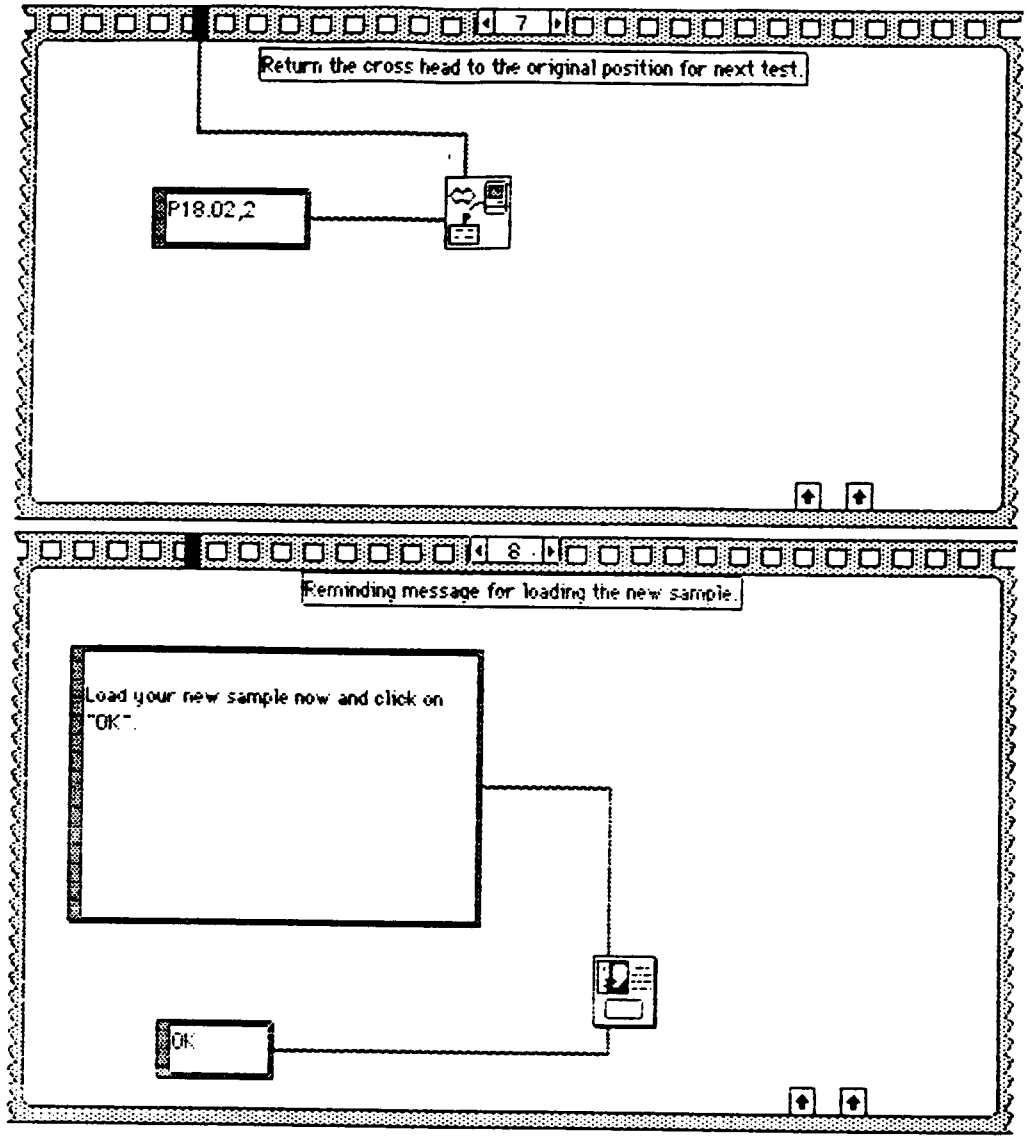
7
Return the cross head to the original position for next test.
P18.02,2
8
Reminding message for loading the new sample.
Load your new sample now and click on "OK".
OK

Stress
Grapher
4.0

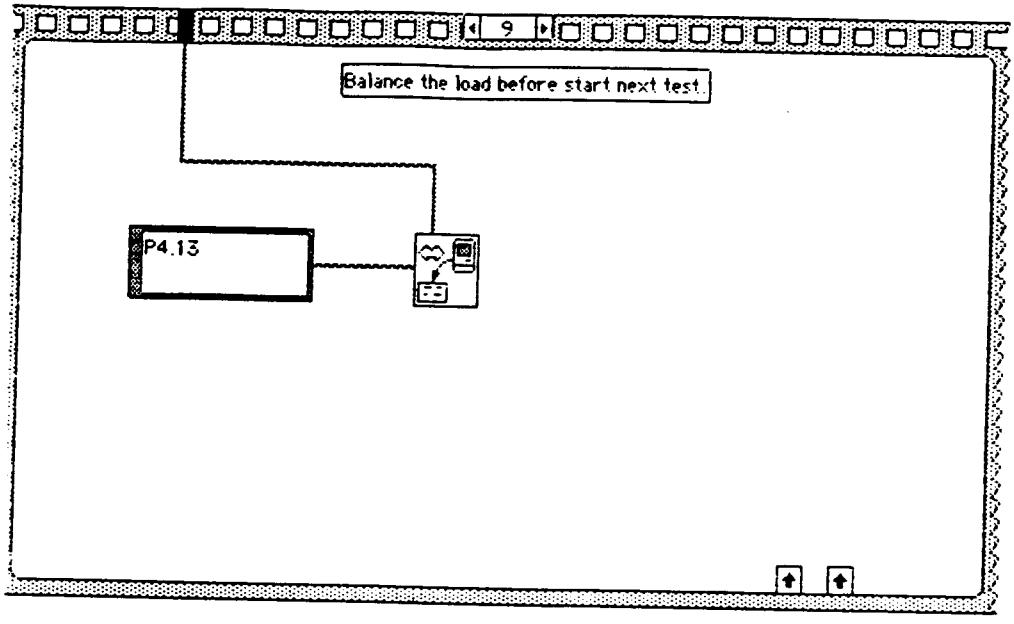

Appendix 2.

Stress Strain Curves

Figure 1. Longitudinal stress strain curve for IM7/5260-H.

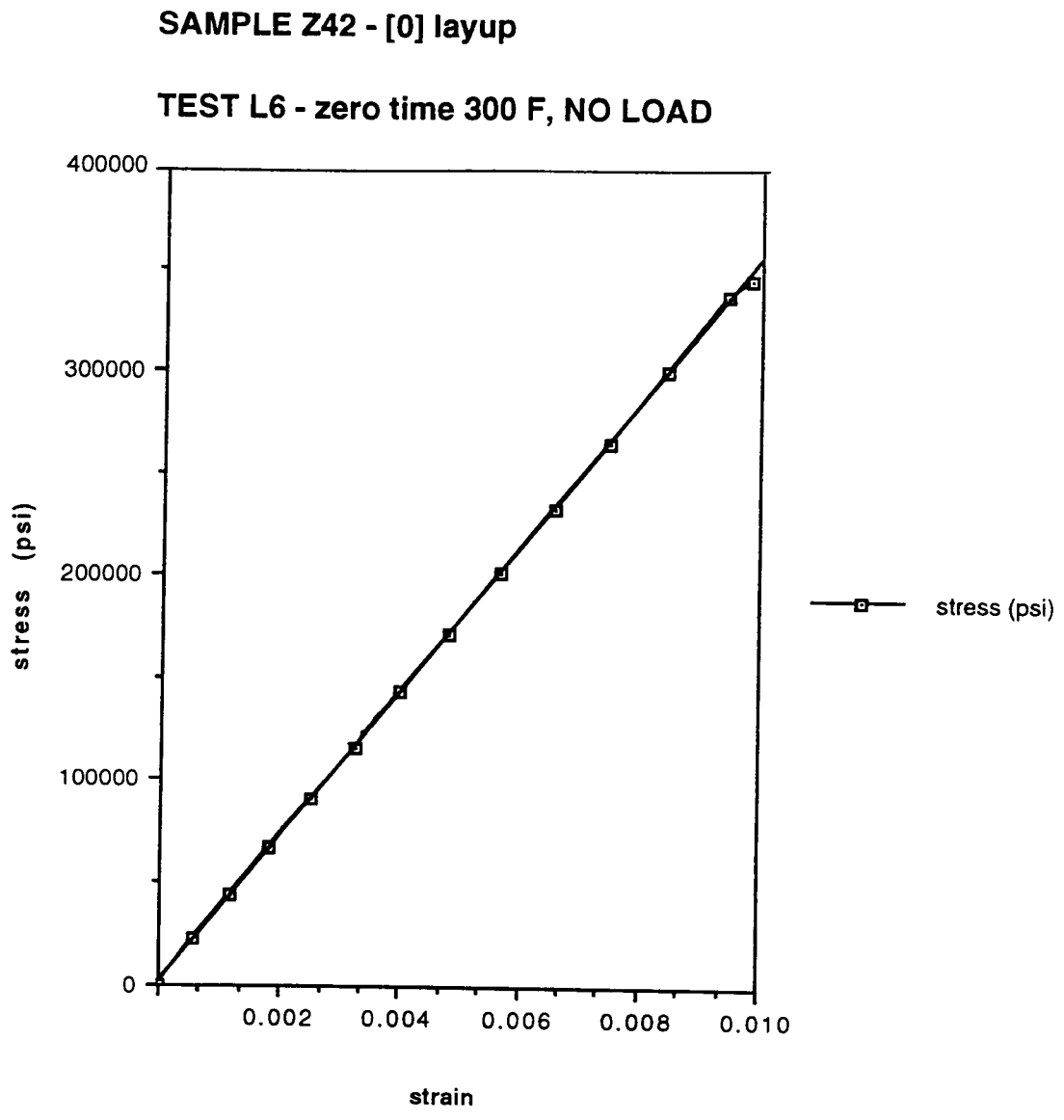

Figure 2. Longitudinal stress strain curve for IM7/5260-H.

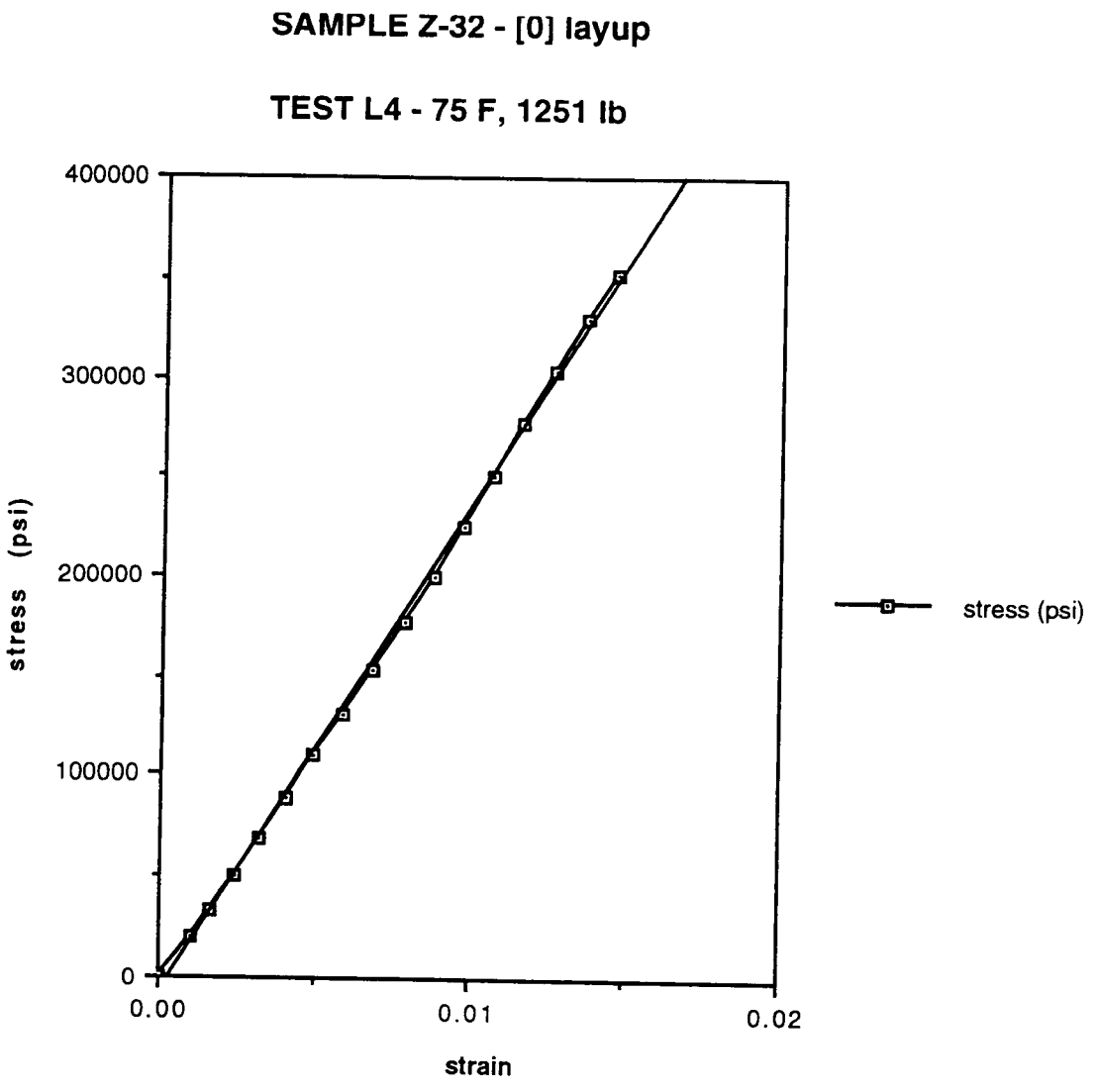

Figure 3. Longitudinal stress strain curve for IM7/5260-H.

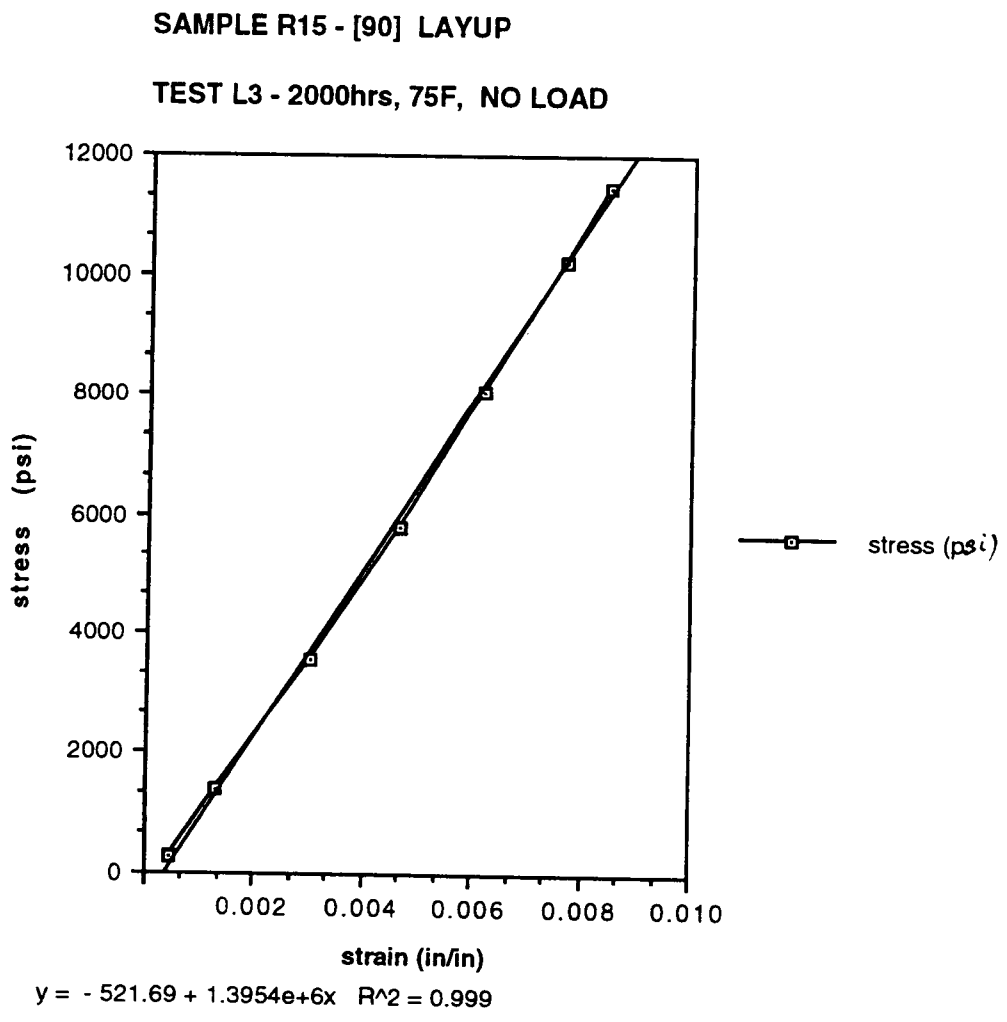

Figure 4. Longitudinal stress strain curve for IM7/5260-H.

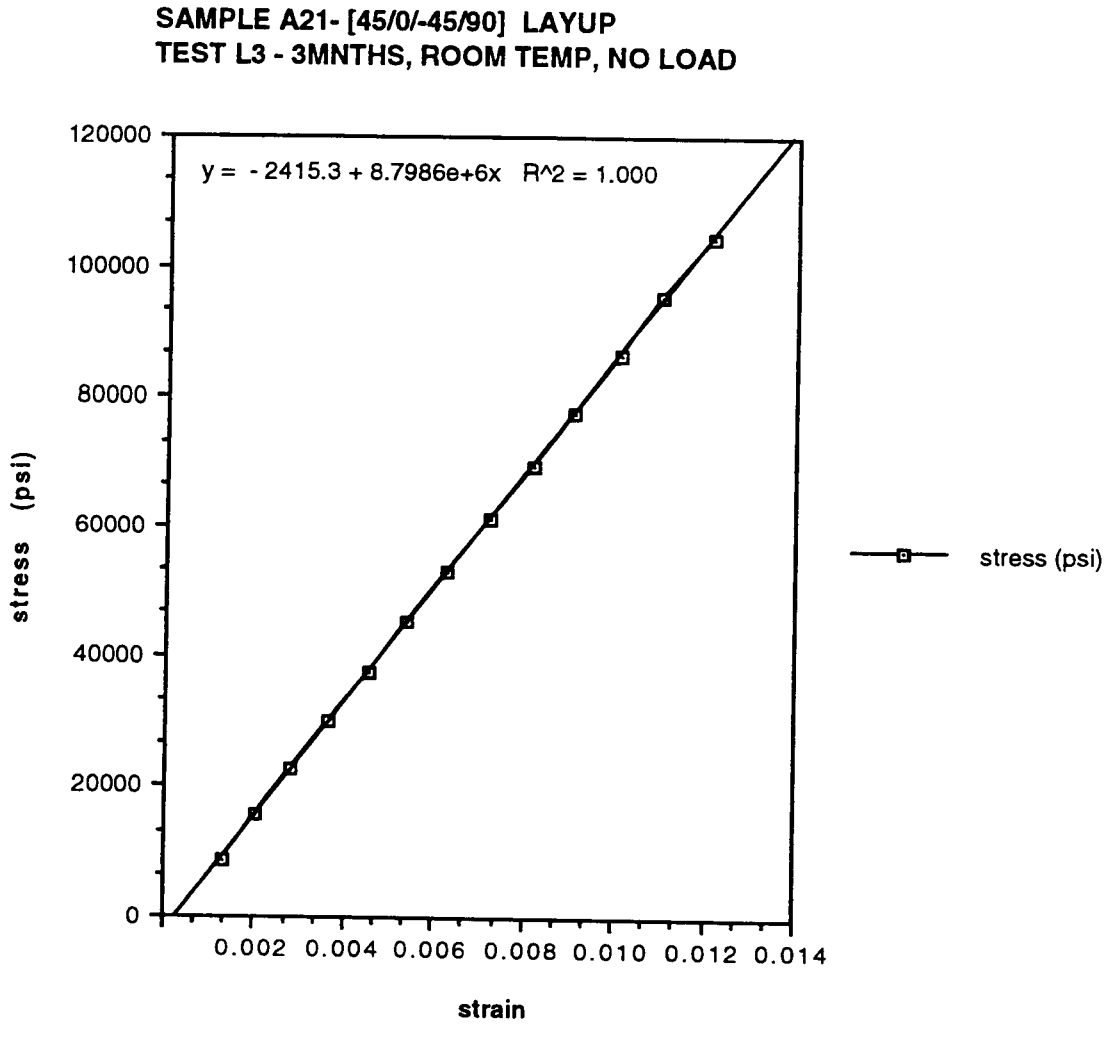

Figure 5. Longitudinal stress strain curve for IM7/5260-H.

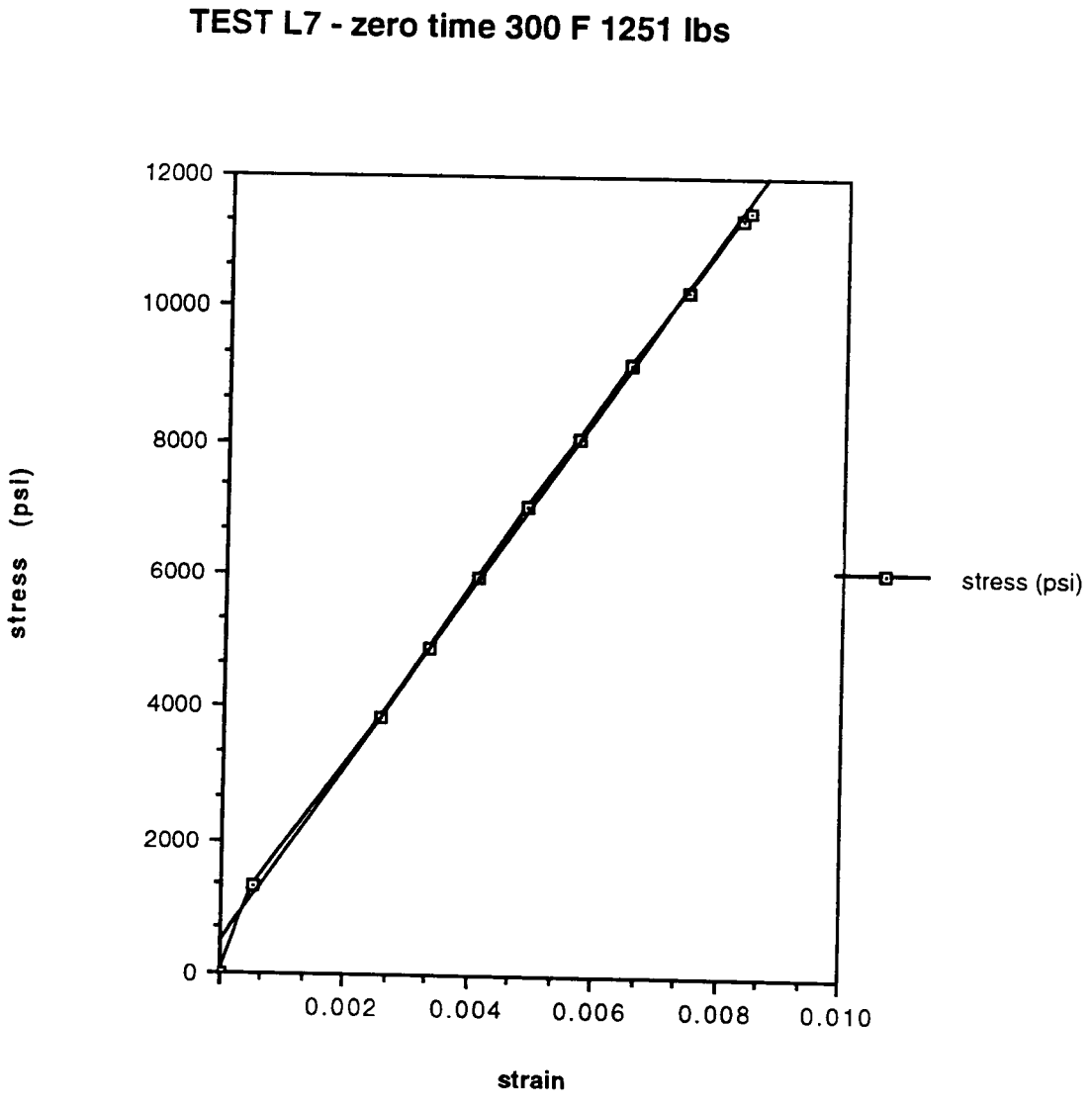

Appendix 3.

Strength Curves

```
/* PROGRAM TO FIND THE CO-ORDINATES OF THE POINTS LYING ON AN */
 /* ELLIPSE DEFINED BY AN EQUATION OF THE FORM */
           /* AX^2+BY^2+CXY=D /*


#include<stdio.h>
#include<math.h>
#define pi 3.14159265359

main()
{
int i;
double sx,sy,a,b,c,d,j,r;

FILE *fopen(),*fpout;
fpout = fopen("ellipse.out","w");

printf("Please input a,b,c, and d");
Printf("for the ellipse in this format 'a,b,c,d'\n");

scanf("%lf,%lf,%lf,%lf",&a,&b,&c,&d);

/* fprintf(fpout,"          sx          sy\n\n"); */

for(i=0;i<=360;i++){
      j = (float)i*pi/180.0;
   r = sqrt(d/(a*pow(cos(j),2.0)-b*cos(j)*sin(j)+c*pow(sin(j),2.0)));

        sx = r*cos(j);
        sy = r*sin(j);
        fprintf(fpout," %6.3f     %6.3f\n",sx,sy);

        }
}

        /*  program ends  */
```

Figure 6. Strength curve in resultant stress space for IM7/5260-H.

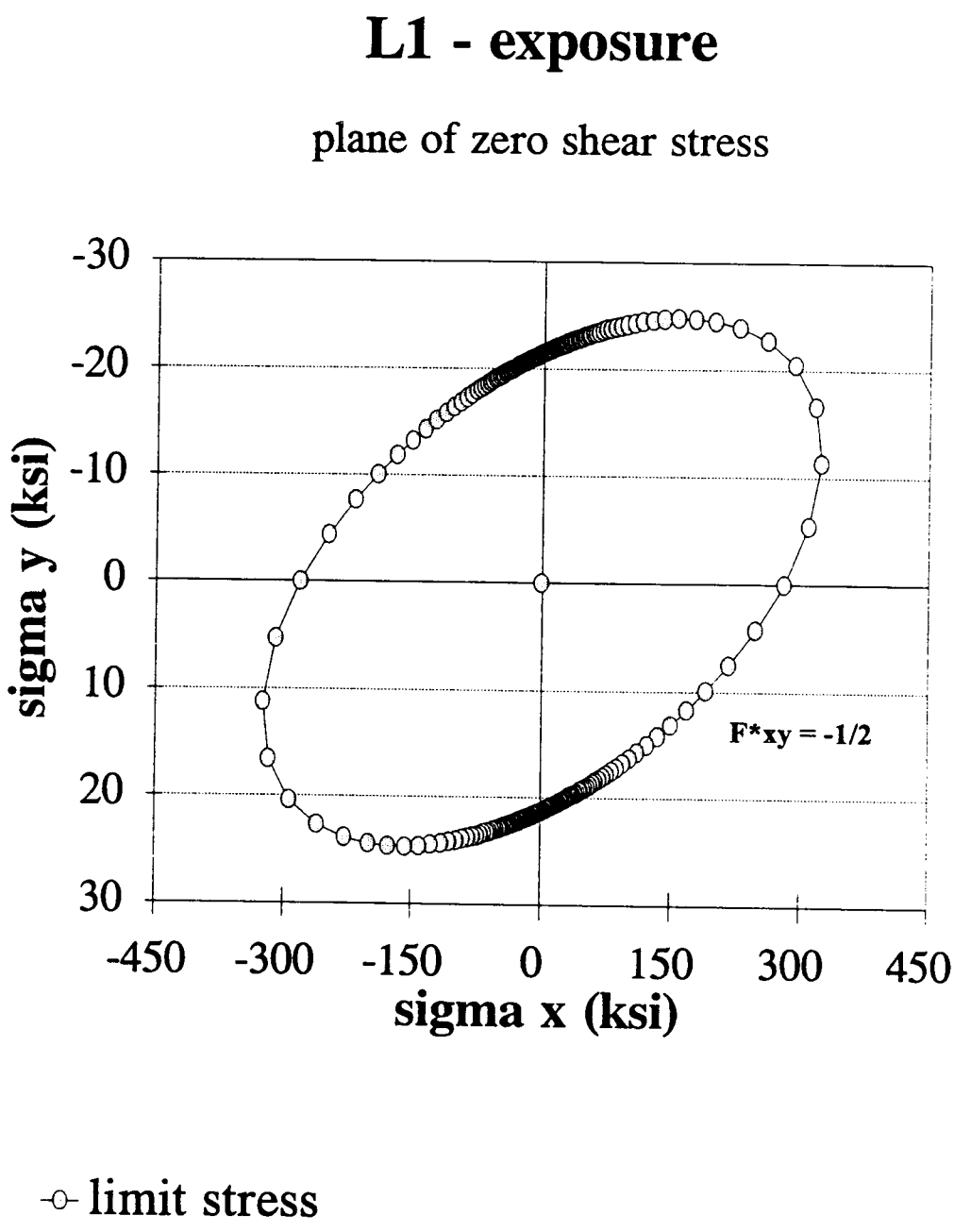

Figure 7. Strength curve in resultant stress space for IM7/5260-H.

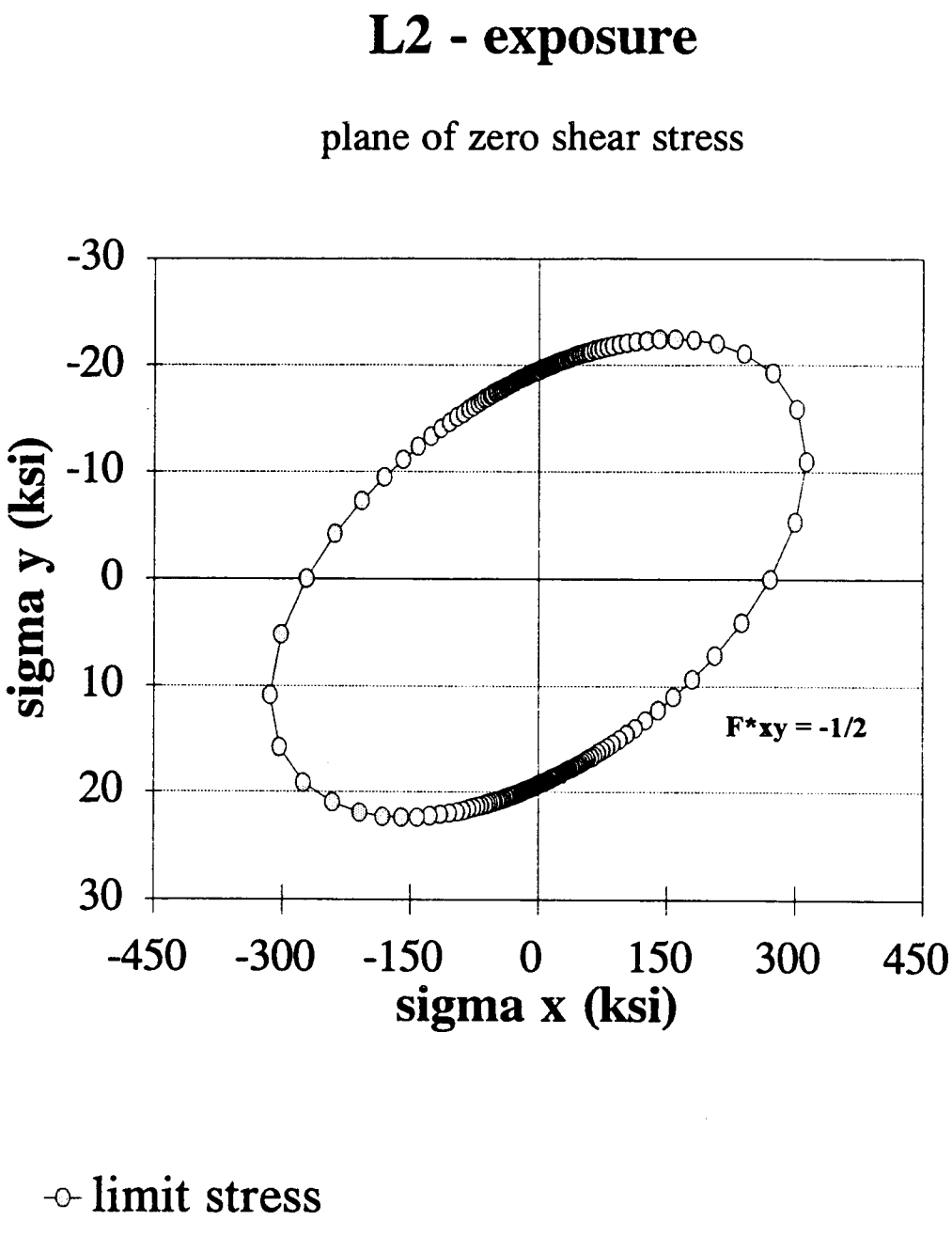

Figure 8. Strength curve in resultant stress space for IM7/5260-H.

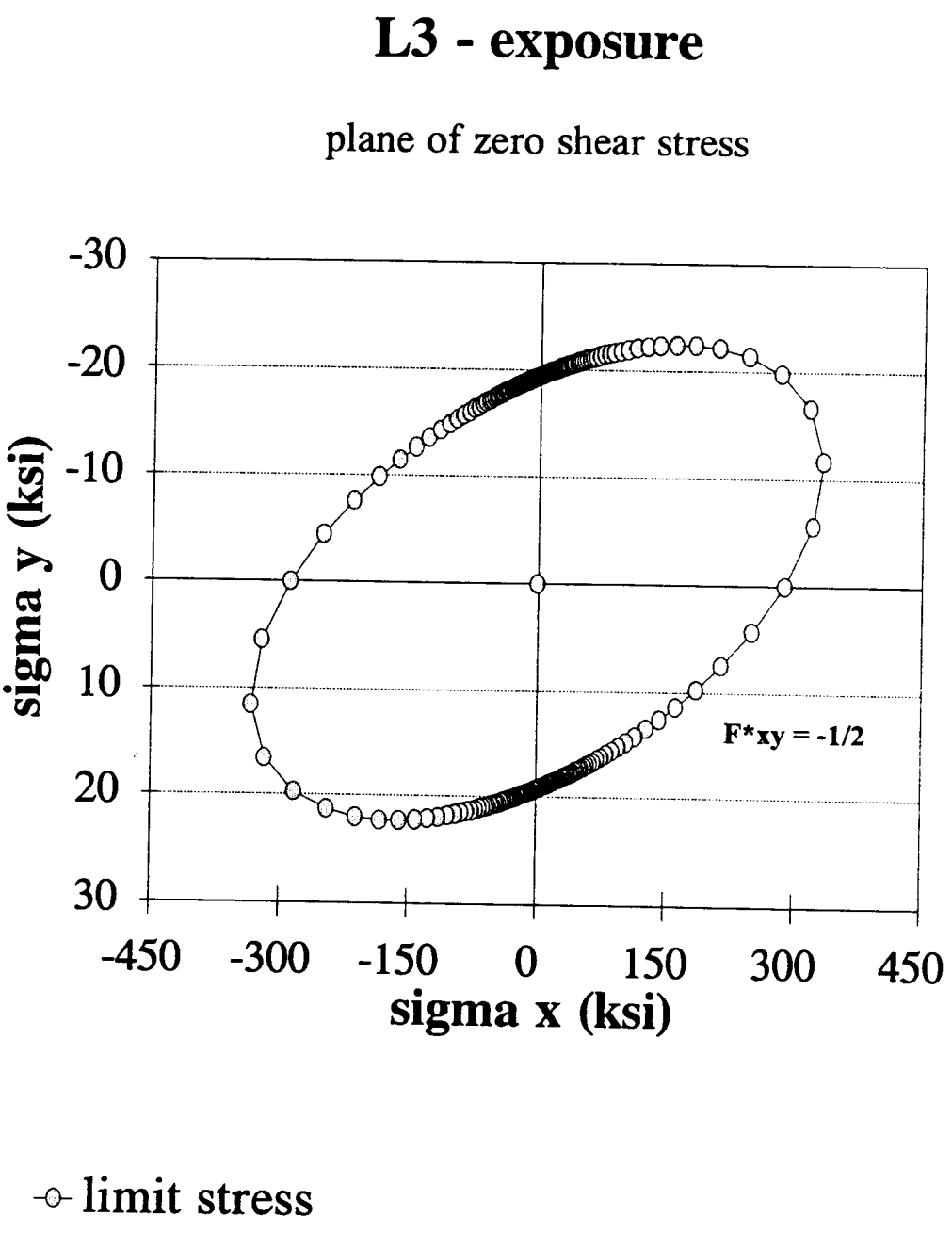

Figure 9. Strength curve in resultant stress space for IM7/5260-H.

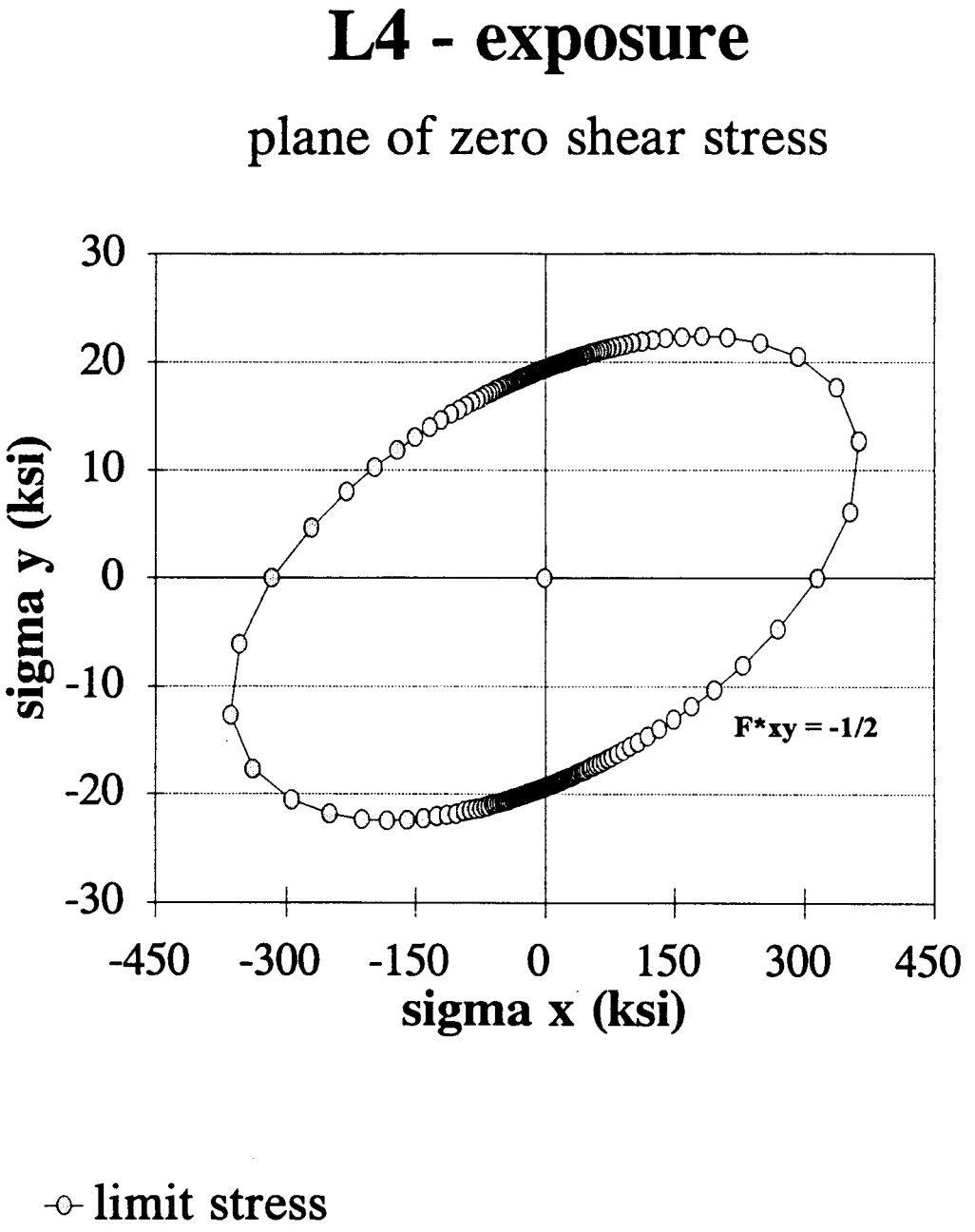

Figure 10. Strength curve in resultant stress space for IM7/5260-H.

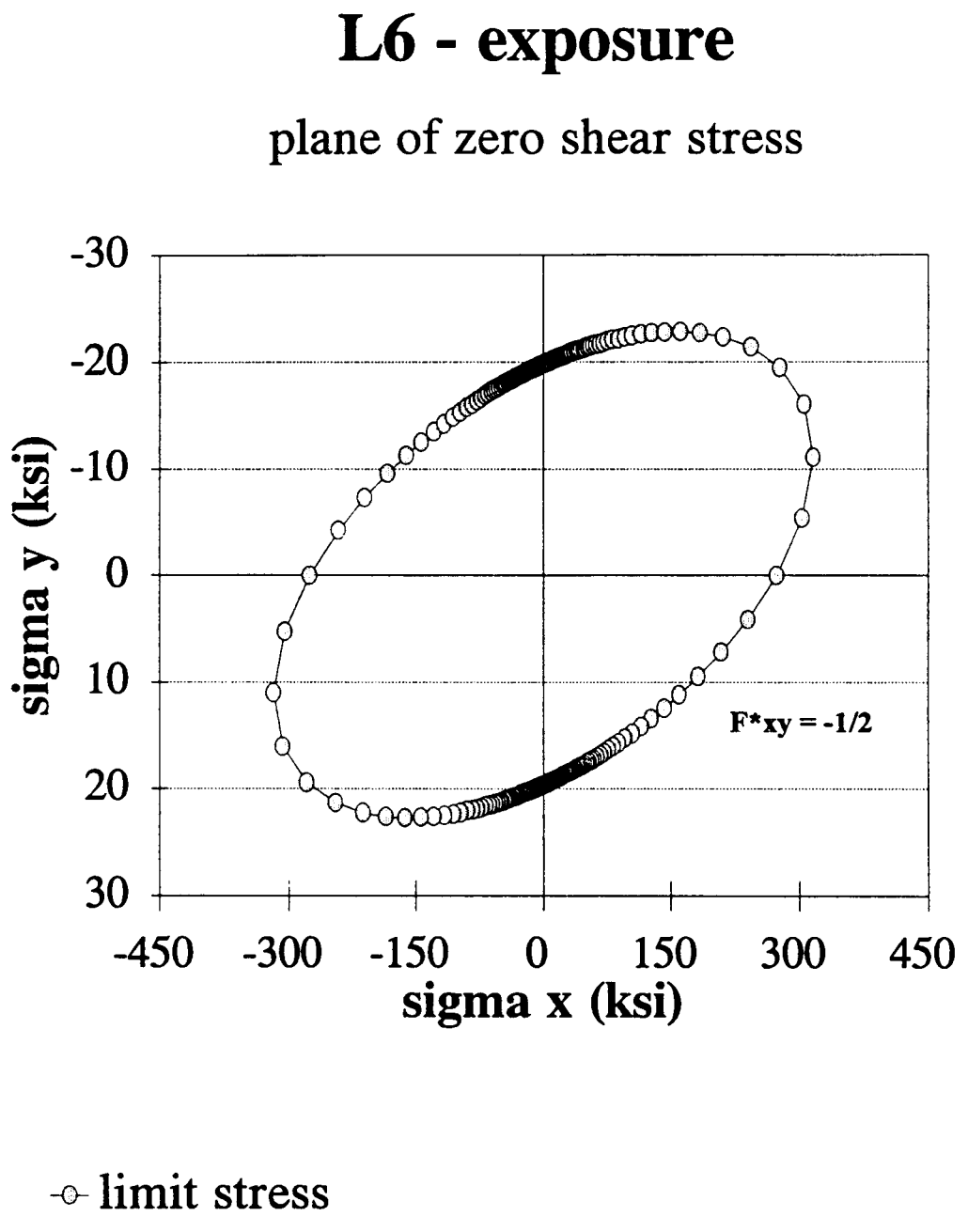

Figure 11. Strength curve in resultant stress space for IM7/5260-H.

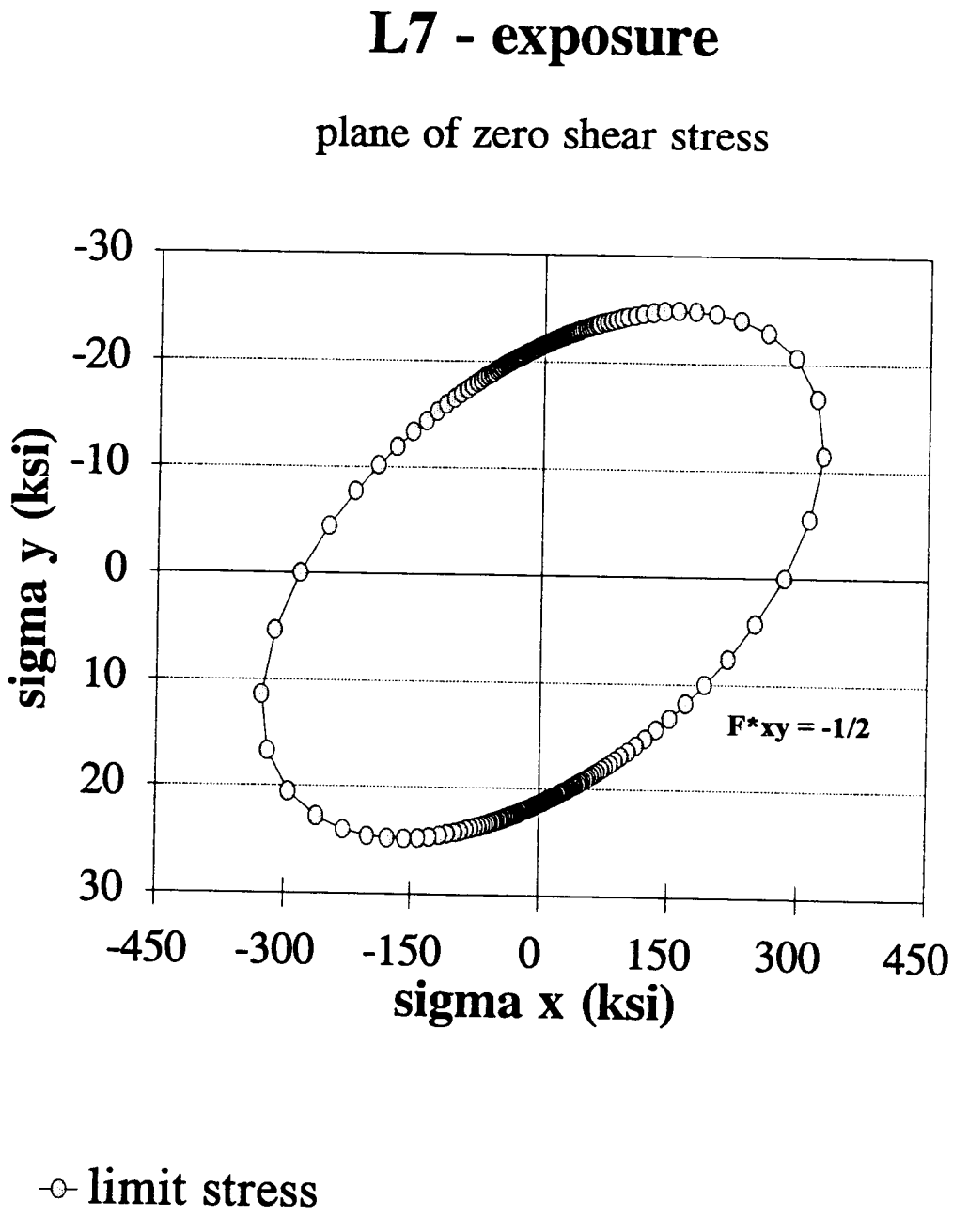

Figure 12. Strength curve in resultant stress space for IM7/5260-H.

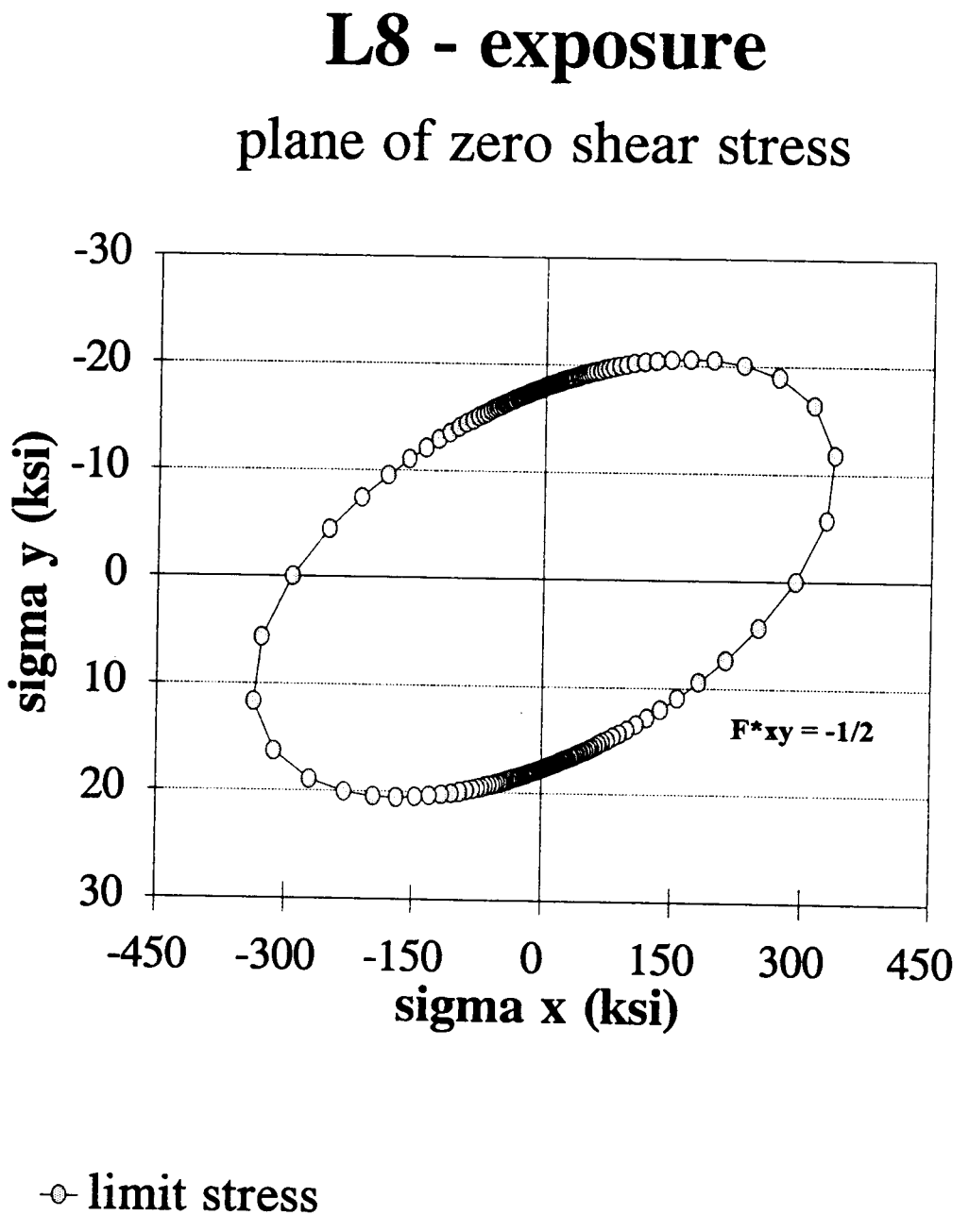

Figure 13. Strength curve in resultant stress space for IM7/5260-H.

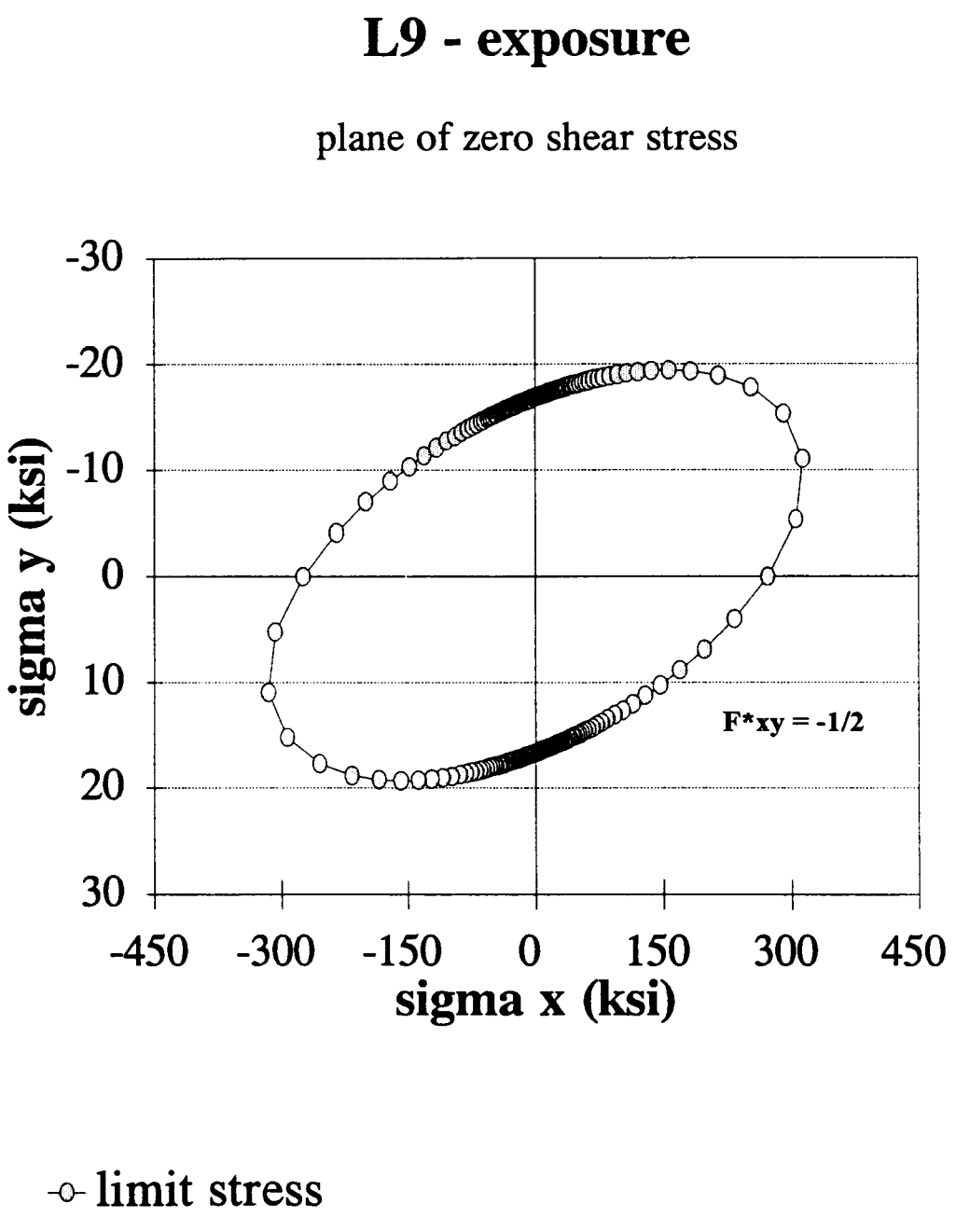

Figure 14. Strength curve in resultant stress space for IM7/5260-H.

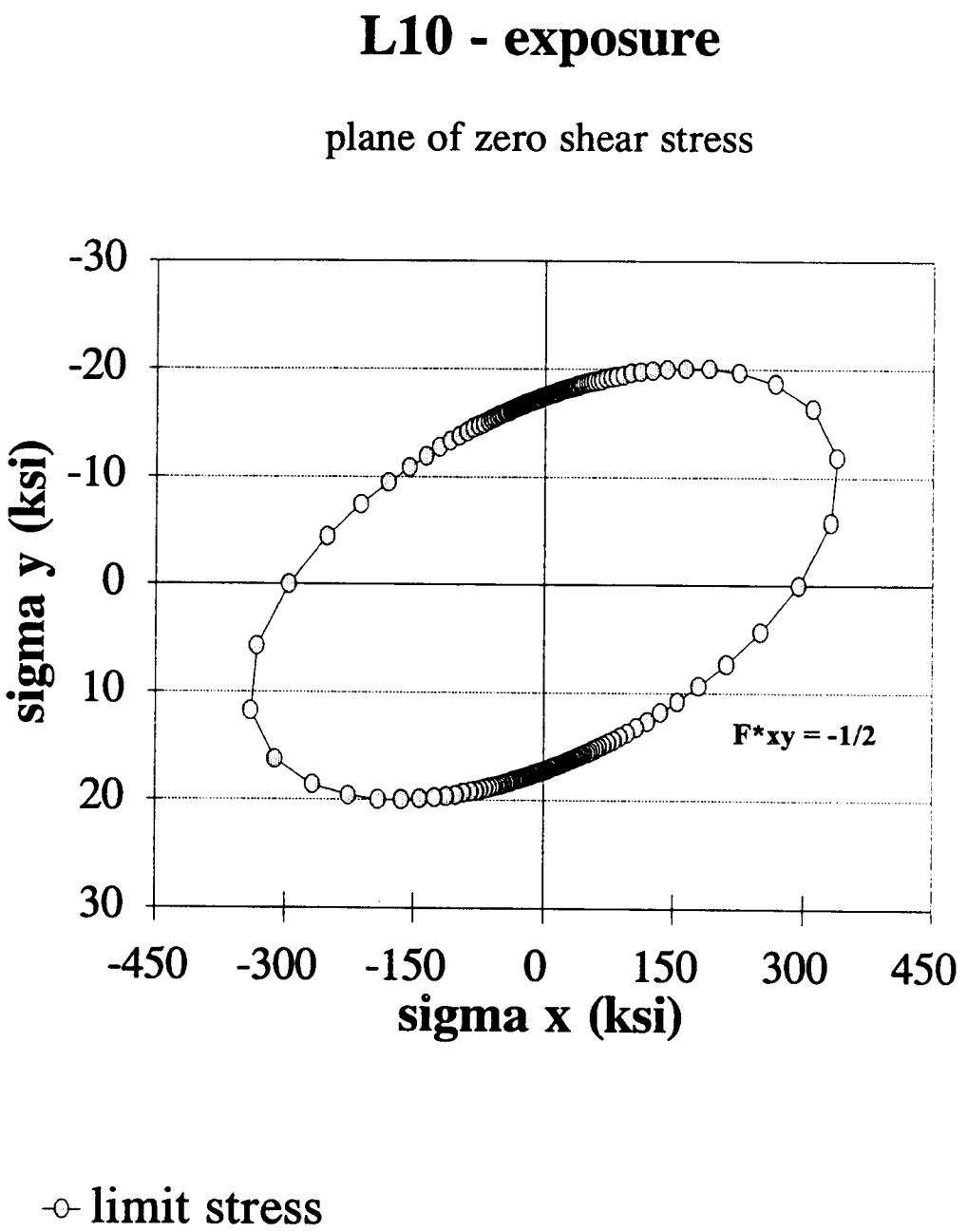

Figure 15. Strength curve in resultant stress space for IM7/5260-H.

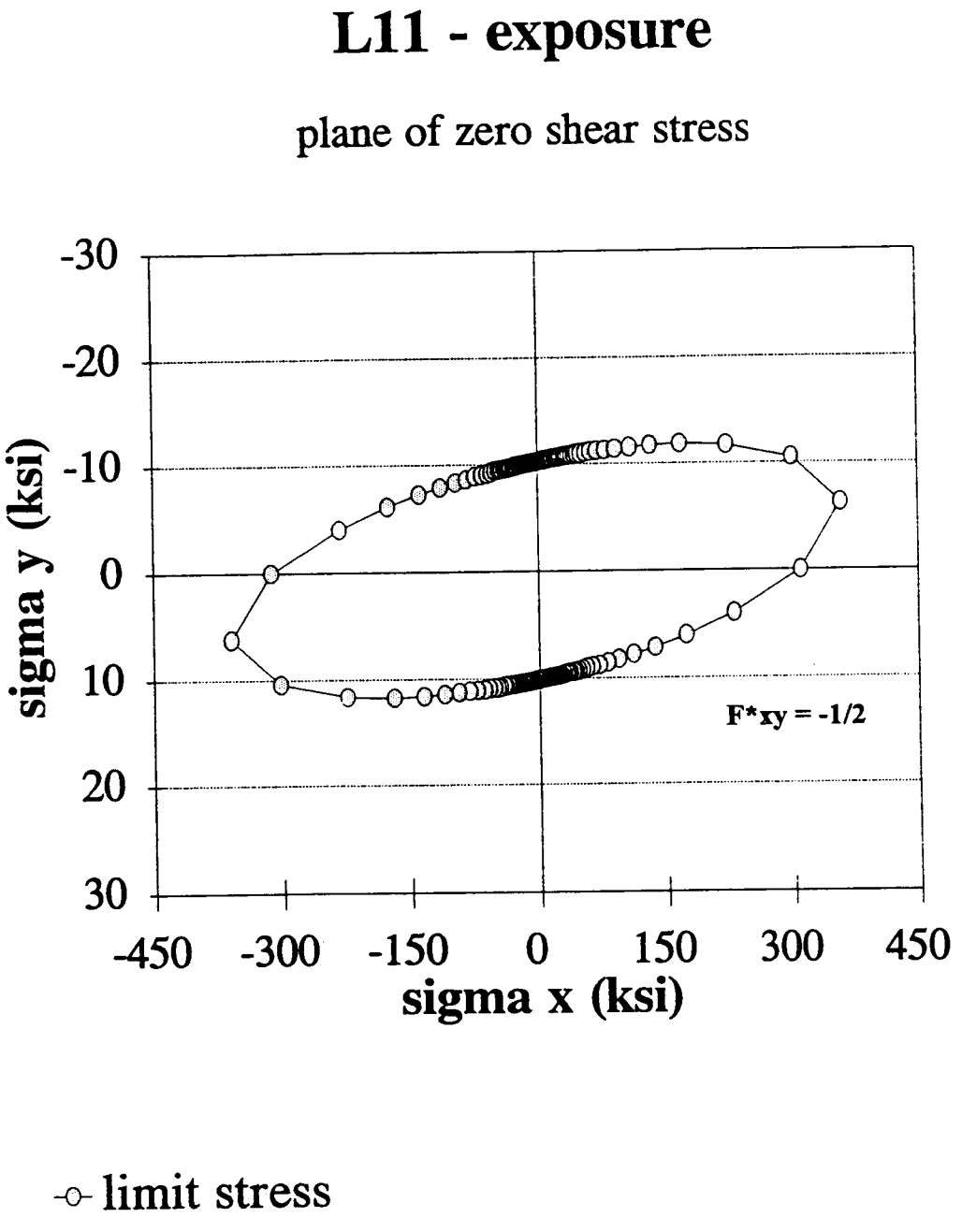

Appendix 4.

Finite Element Program Listing and Plots

```
FEA Problem setup for a [90]16 Gr/BMI
laminate with L5 conditioning history

FILE,90L5RR.GEO,1,1,1,1,
EGROUP,1,SHELL4L,1,16,0,0,0,0,0,
RCONST,1,1,1,10,0.0465,0,0.0058125,1,90,0.0058125,1,90,.0058125,1,
RCONST,1,1,11,10,90,.0058125,1,90,.0058125,1,90,.0058125,1,90,
RCONST,1,1,21,10,.0058125,1,90,.0058125,1,90,.0058125,1,90,.0058125,
RCONST,1,1,31,10,1,90,.0058125,1,90,.0058125,1,90,.0058125,1,
RCONST,1,1,41,10,90,.0058125,1,90,.0058125,1,90,.0058125,1,90,
MPROP,1,EX,1.4E6,
MPROP,1,EY,0.41E6,
MPROP,1,NUXY,0.279,
PT,1,5,0.5,0,
PTGEN,1,1,1,1,0,0,-1.0,0,
PTGEN,1,1,2,1,0,-10.0,0,0,
SCALE,0,
CRPLINE,1,1,2,4,3,1,
SF2CR,1,4,2,0,
M_SF,1,1,1,4,40,4,1,1,
DND,1,ALL,0,165,41,
DSF,1,UZ,0,1,1,RX,RY,,
TUNIF,75,
PCR,1,5510,1,1,5510,
PRINT_ELSET,5,41,41,60,60,80,81,100,100,120,120,
DATA_CHECK
R_CHECK
R_STATIC
```

```
FEA Problem setup for a [0]8 Gr/BMI
laminate with L5 conditioning history

FILE,ZEROL5R.GEO,1,1,1,1,
EGROUP,1,SHELL4L,1,8,0,0,0,0,0,
RCONST,1,1,1,10,0.234,0,2.925E-3,1,0,2.925E-3,1,0,2.925E-3,1,
RCONST,1,1,11,10,0,2.925E-3,1,0,2.925E-3,1,0,2.925E-3,1,0,
RCONST,1,1,21,6,2.925E-3,1,0,2.925E-3,1,0,
MPROP,1,EX,34.8E6,
MPROP,1,EY,3.49E6,
MPROP,1,NUXY,0.279,
PT,1,5,0.25,0,
PTGEN,1,1,1,1,0,0,-0.5,0,
PTGEN,1,1,2,1,0,-10,0,0,
SCALE,0,
CRPLINE,1,1,2,4,3,1,
SF2CR,1,4,2,0,
M_SF,1,1,1,4,40,4,1,1,
DND,1,ALL,0,165,41,
DSF,1,UZ,0,1,1,
TUNIF,75,
PCR,1,53890,1,1,53890,
PRINT_ELSET,5,41,41,60,60,80,81,100,100,120,120,
PRINT_OPS,0,0,0,0,0,0,0,0,0,0,
DATA_CHECK
R_CHECK
R_STATIC
```

Figure 16. Strain distribution plot for IM7/5260-H.

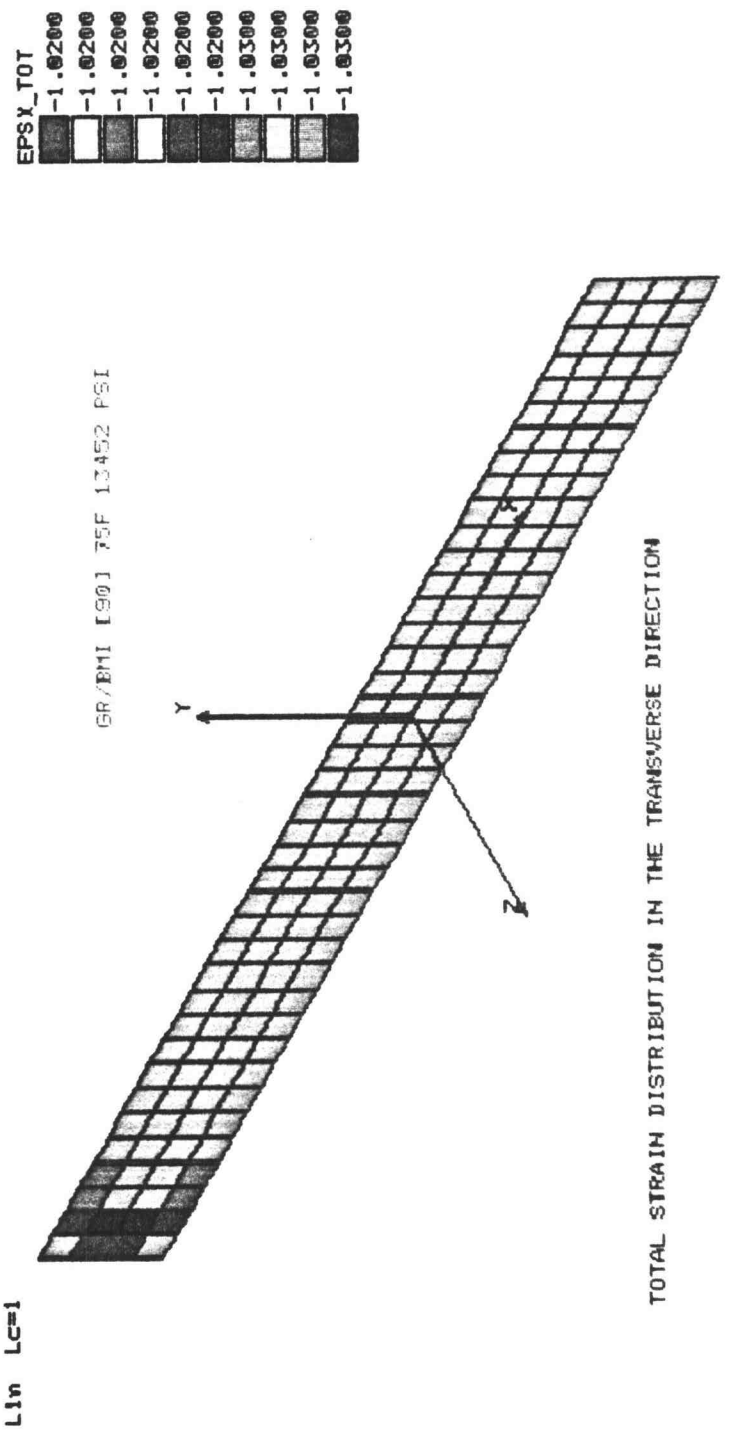

Figure 17. Displacement contour plot for IM7/5260-H.

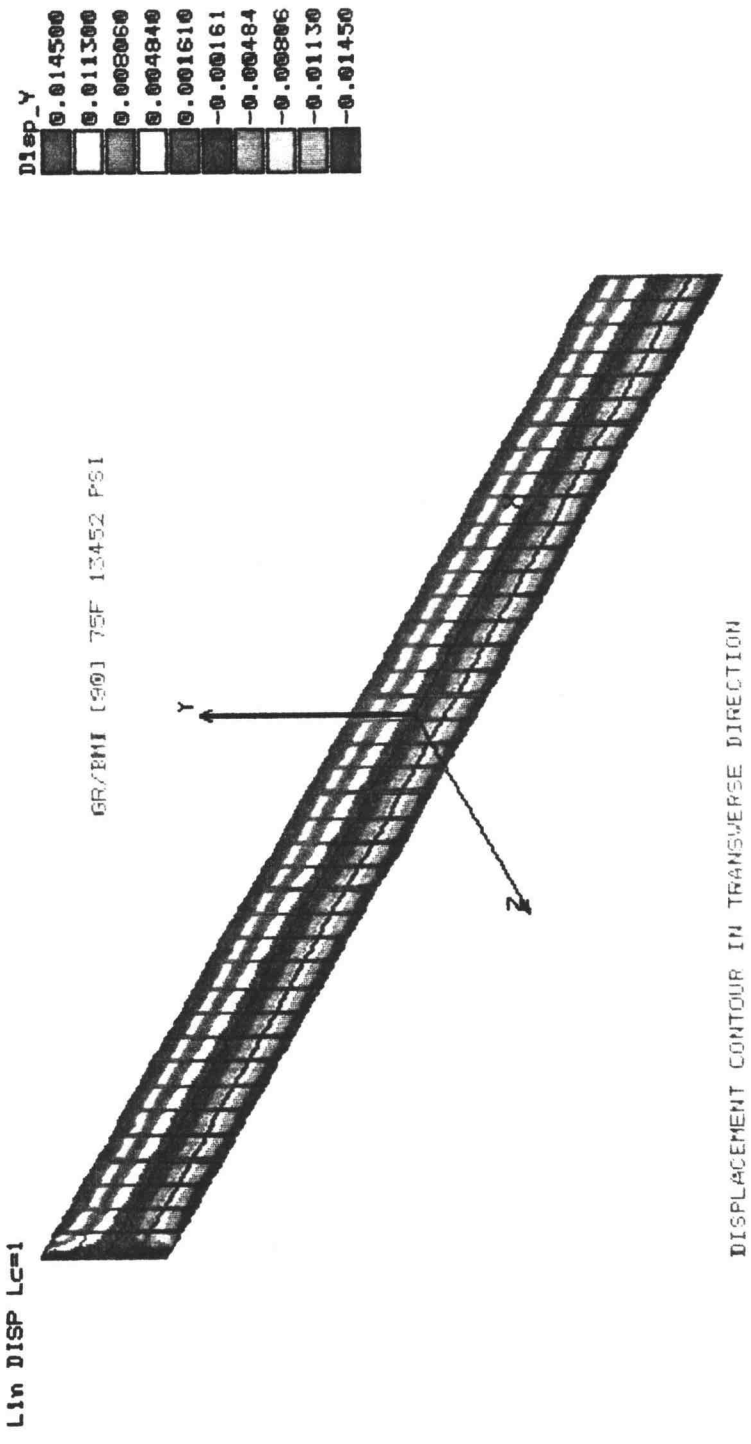

Figure 18. Strain distribution plot for IM7/5260-H.